University of Sheffield

Developing Tools and Techniques to Enhance the Accessibility and Robustness of Expansion Microscopy

Rajpinder Singh Seehra

Submitted in accordance with the requirements for the degree of

Doctor in Philosophy

The University of Sheffield

School of Biosciences

March, 2025

Declaration of Authorship

The candidate affirms that the work presented in this thesis is their own, except where sections of jointly-authored publications have been incorporated. The specific contributions of the candidate and other authors to these works are clearly outlined below, with their consent. The candidate also confirms that appropriate credit has been given to the work of others throughout the thesis.

Acknowledgements

Before diving into this thesis, I would like to thank the amazing people who have supported me throughout this journey.

Izzy Jayasinghe, my amazing supervisor, whose unwavering guidance has made this PhD a core part of my development.

Dan Bose, who supported me through my PhD, with keen insight and sound advice.

Ash Cadby, for inspiring me to pursue this line of research.

Tayla Shakespeare, my erstwhile compatriot on this rocky path of a PhD that we started at the same time.

Tom Sheard, for being a steady guiding hand, and always making time to hear me out, even with the heavy coding work.

Michael Spencer, for persisting with our countless leaky plates and supporting our groups efforts.

Mum, Dad, Eeshar and Avi, my loving family who always spare an ear to hear my many thoughts and ideas, no matter how nonsensical they sound.

Author Publications

Work presented in this thesis has been featured in the publication listed below. The contributions of co-authors to the presented work have been listed in the sections where relevant.

Establishing the fundamentals of plate ExM from Chapter 3, and Validation of Microplate ExM and Distortion Analysis from Chapter 4 contain data from Seehra et al. (2023). The author performed all expansion microscopy experiments and data analysis. The co-author contributions involved: *Drosophila* fly wing sample preparation, material provision and writing of the manuscript.

Seehra, R.S., Warrington, S.J., Allouis, B.H.K., Sheard, T.M.D, Spencer, M.E., Shakespeare, T., Cadby, A., Bose, D., Strutt, D. & Jayasinghe, I. (2023). **Geometry-preserving expansion microscopy microplates enable high-fidelity nanoscale distortion mapping.** *Cell Reports Physical Science*, 4(12), p.101719.

Abstract

Expansion microscopy (ExM) allows users to visualise biomolecules, cellular ultrastructure, and tissue architecture with the use of the osmotic expansion of hydrogels to attain molecular-scale resolution of structures below the diffraction limit. However, multiscale distortions that can impact the quantitative potential of the image data are intrinsic to this method.

The current gold standard of error estimation in ExM is achieved through two-dimensional (2D) registration of pre- and post-expansion images, an inherently labour and skill-intensive process. An analysis and pipeline that examines the three-dimensional (3D) nature of distortions is also lacking.

Here, we present a 3D-printable plate approach which provides one of the first high-throughput approaches to ExM, particularly for imaging nanoscale features of sub-cellular and tissue structure. By further employing these techniques we explore the nature of 3D ExM and provide a methodology by which to analyse the image data.

Table of Contents

List of Tables

List of Figures

List of Abbreviations

ABS – Acrylonitrile butadiene styrene

APS – Ammonium persulfate

DMAA – N,N-dimethylacrylamide

DMEM -Dulbecco's modified eagle medium

DNA-PAINT – DNA points accumulation for imaging in nanoscale topography

DyMin – Dynamic minimum intensity

EF – Expansion factor

ExM – Expansion microscopy

FDM – Fused deposition modelling

FLARE – Fluorescent labelling of abundant reactive entities

FRET – Förster resonance energy transfer

GaAsP – Gallium arsenide phosphide cathodes

HEPES – 4-(2-Hydroxyethyl)piperazine-1-ethanesulfonic

IExM – Iterative expansion microscopy

KPS – Potassium persulfate

MAP – Magnified analysis of the proteome

MINFLUX – Minimum fluorescence photon flux

NA – Numerical aperture

NHS – *N*-hydroxysuccinimide

NUP – Nucleoporin

PALM – Photoactivated localisation microscopy

PBS – Phosphate-buffered saline

PFA – Paraformaldehyde

PLA – Polylactic acid

Pro-ExM – Protein-retention expansion microscopy

PSF – Point spread function

RESI – Resolution enhancement by sequential imaging

RMSE – Root-mean-square error

RPE-1 – Retinal pigment epithelial cells

SIFT – Scale-invariant feature transform

SIM – Structured illumination microscopy

SNR – Signal-to-noise ratio

SRRF – Super-resolution radial fluctuations

STED – Stimulated emission depletion

STORM – Stochastic optical reconstruction

TEMED – Tetramethylethylenediamine

TREx – Ten-fold robust expansion microscopy

U-ExM – Ultrastructure expansion microscopy

Chapter 1. Introduction

1.1. Light Microscopy

Light microscopy is fundamental to modern research. In its simplest form, light microscopy consists of a light source, a sample holder and objective lens, allowing for basic visualisation of structures not visible to the naked eye. This core concept has been widely adapted and developed to create imaging modalities such as brightfield, phase-contrast and epifluorescence microscopy.

However, these modalities are inherently limited by the diffraction limit, a bound wherein objects closer to one another than this limit are indistinguishable from one another (Figure 1-1.B). This boundary originates from the wave-like nature of light being diffracted by optical elements, diffusing the wavefront and producing a diffraction pattern. This sets a limit for the resolution of the imaging technique. In classical light microscopes this is expressed using the Abbe diffraction limit (Abbe, E, 1873):

$$d = \frac{\lambda}{2nsin\theta} = \frac{\lambda}{2NA}$$

Wherein, the wavelength of light λ, travels through a medium with refractive index of n, converging to a point with a half-angle θ (Figure 1-1.A). The numerical aperture (NA) is the same as $nsin\theta$ and can simplify the equation based upon this commonly used nomenclature (Figure 1-1). For a modern microscope with a NA of 1-1.5 the diffraction limit under 500 nm green light would range from 250 nm to 167nm as the NA increases.

Whilst cells are generally above this scale, the many components comprising their ultrastructure remain below the diffraction limit and are unable to be resolved. These components include a vast array of nanoscale structures (i.e. organelle membrane and fine structure, endoplasmic reticulum, endosomes, antibodies, viruses) which are important for scientific investigation. Many dynamic events also occur at this scale (<250 nm), from protein folding to molecular signalling, the diffraction limit blurs these events, preventing observation and limiting investigation (Betzig et al., 2006). Being able to visualise information at this scale allows the quantitative assessment of the structures and molecules of interest.

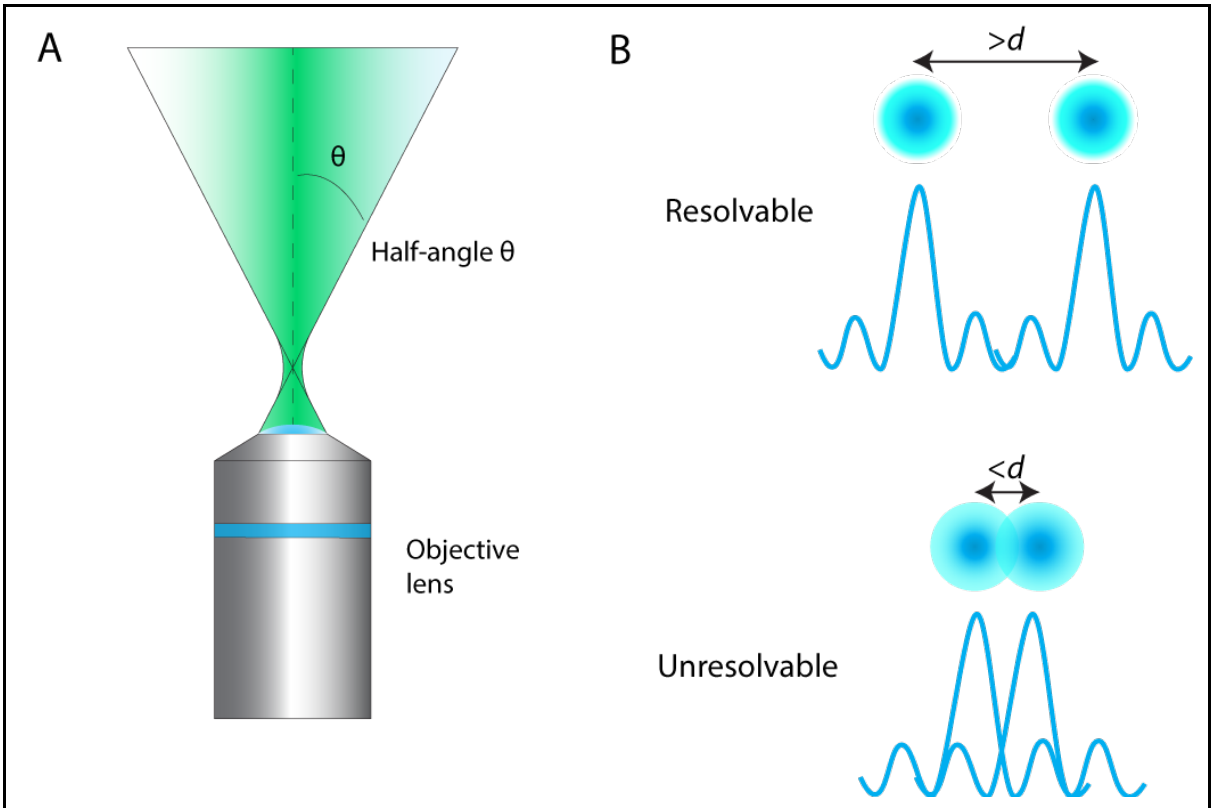

Figure 1-1: Resolution Limit of Structures

Illustration breakdown the factors influencing the resolution limit A) Illustration of the half-angle of the objective lens. B) Example illustration of illumination pattern of structures resolvable at a distance greater than the diffraction limit d, and unresolvable at a distance less than d.

1.2. Overcoming the Diffraction Limit

The point-spread function (PSF) is defined by an object below the diffraction limit which appears as a diffraction-limited spot. The PSF contains information describing the diffraction effects inherent to the light pathway in the microscope and propagates from a central intensity. This results in an Airy disk being produced as a product of interference in the diffracted wavefront in 3D space. The main avenues of overcoming this bound involve light collection, PSF engineering and computational localisation. An example of PSF engineering includes suppressing of the fluorescence using an additional laser altering the PSF, as in Stimulated Emission Depletion microscopy (STED). Whilst computational localisation can be performed by the suppression of fluorescence and identifying the centroids of the individual molecules, as in Stochastic Optical Reconstruction microscopy (STORM).

1.2.1. Early Super-Resolution Imaging

Early approaches to overcoming the diffraction limit and acquiring super-resolution images, images below the diffraction limit, were primarily focused on light collection and PSF engineering.

Confocal microscopy uses a pinhole to limit out-of-focus light, removing structures from the PSF, increasing the resolution of the data collected (Figure 1-2.A). The pinhole is placed prior to the detector, and the size is adjusted based on the emission wavelength to be the size of an Airy unit. This reflects the size of the Airy disk, the size of the central disk of the PSF of the system (Aguet, 2009). To allow this to work, confocal systems scan across the imaging plane to construct the image, with data at each point being collated and processed. With advances in the technique from

spinning disk to Airyscan, the speed of this method has increased from its point-scanning origin. The Airyscan system, developed by Zeiss, uses a detector array instead of a standard unitary detector. This allows for measurement of the PSF over the detector and therefore allowing for an increase in the light collection of the system and the signal-to-noise ratio through pixel reassignment of the collected data. These in turn increase resolution of the system, stepping towards overcoming the diffraction limit. These advancements have allowed confocal microscopy to become more ubiquitous and can be easily used to extend the functions of a standard fluorescence microscope.

4Pi microscopy uses a second objective lens on the opposing side of the sample to the primary objective, increasing light collection (Figure 1-2.B). The lenses are aligned to the same location, allowing for the collection of the forward and backward light cone simultaneously. By controlling for the length of the light path the information can be superimposed to acquire image data with an axial resolution improvement up to 100-150 nm (Nagorni and Hell, 1998).

This resolution improvement is limited to the axial plane and can be effective in resolving 3D structures at the diffraction limit by allowing for isotropic voxel sizes.

STED microscopy uses two overlapping lasers to stimulate a central region of fluorophores and deplete a surrounding donut of fluorophores, engineering the PSF (Figure 1-2.C). The quenching of the outer fluorophores pushes them into a higher vibrational state wherein they cannot be excited by the quenching laser. This effectively stops the fluorescence and reduces the size of the focal spot, improving

resolution (Klar et al., 2000). Depending on the optical elements used, the shape of this region can be altered to improve both axial and lateral resolutions (Reuss et al., 2010; Török and Munro, 2004), up to 100 nm and 30 nm, respectively (Carravilla et al., 2019; Bergstrand et al., 2019; Klar et al., 2000; Hell and Wichmann, 1994), depending on noise and aberrations.

This degree of resolution allows for structural analysis of complex organelles such as mitochondria (cardiac mitochondria imaging with protein clusters at 20-30 nm size) (Singh et al., 2012), endosomes (synaptic membrane protein clustering forming microdomains with endosomes >200 nm) (Geumann et al., 2010), and endoplasmic reticulum (live-cell STED imaging of ER with ~60nm resolution) (Hein et al., 2008). Adaptations for live-cell imaging maintain the sub-diffraction limit resolution whilst allowing for further exploration of cell dynamics inclusive of: gap junctions (Hein et al., 2010), synaptic vesicles (Westphal et al., 2008) and epidermal growth factor receptors (Pellett et al., 2011).

However, photobleaching, caused by the increased laser power, remains an issue with the technique, limiting the viability of high-resolution live cell imaging. Systems such as dynamic minimum intensity (DyMIN), determine if a signal is present and switch off the laser exposure is no signal is detected (Heine et al., 2017). Thereby reducing the exposure time of the sample and henceforth photobleaching.

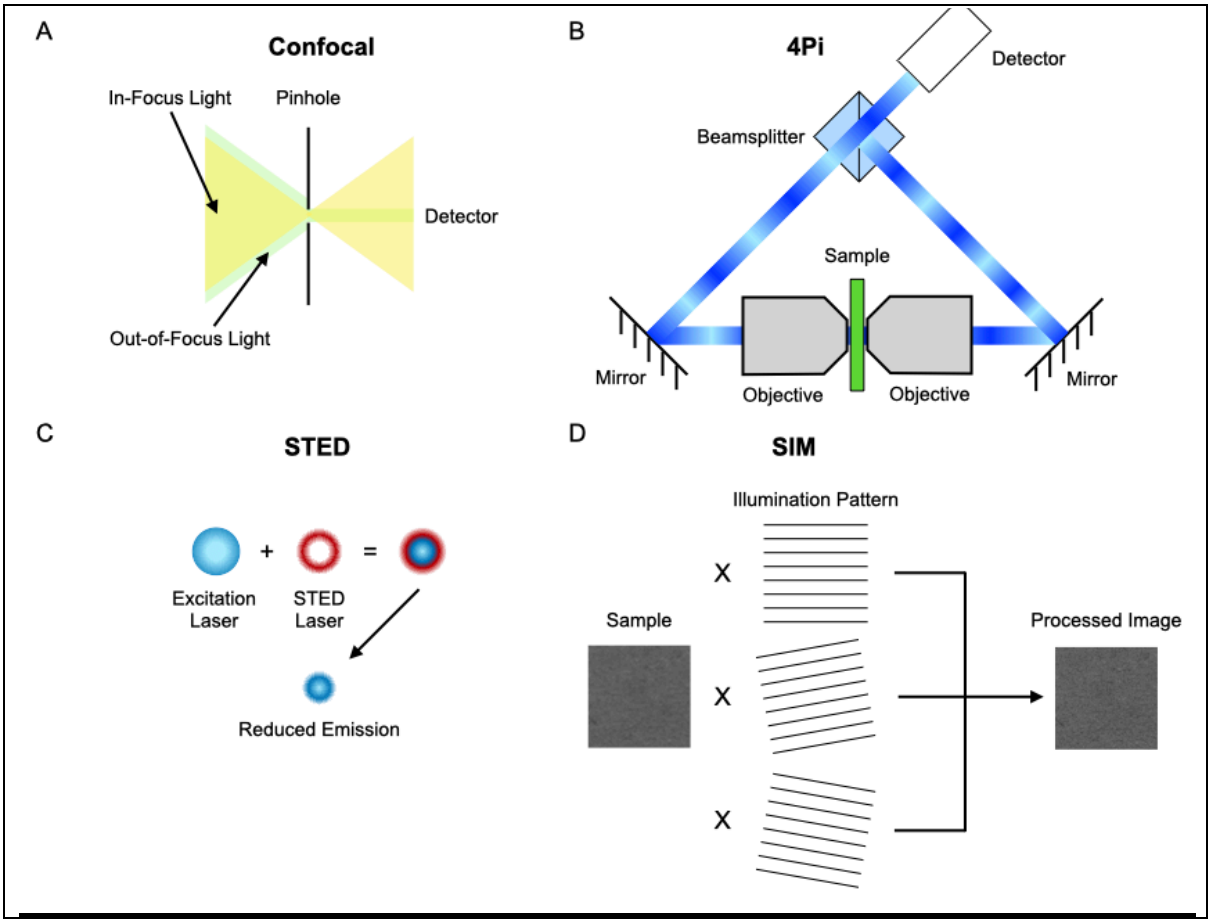

Figure 1-2: Mechanisms of Confocal, 4Pi, STED and SIM Techniques

Diagrams illustrating the following techniques: **A)** Confocal microscopy: a pinhole is used to remove out-of-focus light, **B)** 4Pi: two objectives are used to maximise light collection, **C)** STED: a ring laser is used to suppress signal creating a reduced emission signal from the sample, **D)** SIM: sample is imaged with an illumination pattern moving high frequency information to lower frequency space, data is processed to acquire a higher resolution image.

1.2.2. Localisation Microscopy

The advent of STORM (Rust et al., 2006) and photoactivated localisation microscopy (PALM) (Betzig et al., 2006) allowed for computational approaches to overcoming the diffraction limit.

STORM suppresses the fluorescence of ‘blinking’ photoswitchable fluorophores (Figure 1-3.A). This works by using a laser to excite the fluorophore and promote transition into the triplet state from the excited energy state. From here the fluorophore can be reduced into a stable dark state. The fluorophore can then be actively driven to the ground state by another laser line to allow for a briefly fluorescence and blinking to occur (Bates et al., 2005).

The acquisition of multiple frames to localise these separate diffraction-limited points allows for the collection of super-resolution data. This works by reducing the number of fluorescence events visualised per frame allowing the capture of individual fluorophores. Using the structure of a predicted PSF, the PSF data in the images can be estimated and localised to a central position, thereby acquiring high resolution images. Through the use of astigmatic lenses, to encode axial information in the PSF, this technique can collect 3D data. This has led to reported resolutions of 20 nm laterally and 50 nm axially.

Comparative resolution has been acquired In 3D live-cell STORM imaging (Jones et al., 2011). However, the balance between spatial resolution, temporal resolution and localisation density has an impact on the accessibility of the technique.

PALM functions using the same principle as STORM, in that individual stochastic events are recorded over many frames (Betzig et al., 2006) (Figure 1-3.B). The key difference between them being the use of photoactivatable fluorescent proteins in PALM. These work by bleaching the fluorophores till a sparse image field was obtained and then applying a secondary laser pulse to active the fluorescent proteins. By

controlling the secondary pulse signal, the response can be tuned to allow for resolvable point structures for measurement. By repeating over thousands of frames a full image can be acquired. This combined with genetic modification to the sample in question allow for simpler live-cell imaging with PALM relative to STORM (Shroff et al., 2008).

DNA points accumulation for imaging in nanoscale topography (DNA-PAINT), also utilises a blinking approach (Schnitzbauer et al., 2017) (Figure 1-3.C). This approach requires the use of imager and docking DNA strands. The imager strand, bound to a dye, transiently binds to the docking strand affixed to the sample. This binding causes the blinking which is captured via imaging over multiple frames to reconstruct the full image. This approach allows for large-scale multiplexing through sequential imaging whilst using the same dye and laser (Jungmann et al., 2014). As the imager strand can be replaced, this also leads to a reduction in bleaching. The transient nature of the binding does, however, limit the acquisition rate of this technique, and requires a fixed specimen.

Resolution enhancement by sequential imaging (RESI), utilises similar concepts to DNA-PAINT. By binding multiple docking strands to a single target, the same target can be imaged at each docking strand and thereby each image sets data can be localised and compared through sequential imaging. Thus in turn increasing resolution as data is computed between each image set (Reinhardt et al., 2023). This resolution increase is isotropic in 3D and has been reported to reach sub-nanometre precision. Akin to DNA-PAINT this technique is primarily applicable to fixed specimens.

Additionally, the size of the DNA strands affects the linkage error and limit the resolution of the technique.

Minimum fluorescence photon flux (MINFLUX) uses a ring-shaped excitation laser with a central minimum for excitation (Figure 1-3.D). A fluorophore directly beneath this centra minima will not fluoresce. As the ring of the laser moves around the active target, the fluorescence intensity will vary, this variance can be used to more accurately localise the molecule. This process minimises the photons emitted by the fluorophore and we can follow single molecules by continuing to minimise the fluorescence of the targeted molecule by following the molecule position (Balzarotti et al., 2017). Localisation events can therefore be tracked, allowing application in live-cell imaging (Gerasimaitė et al., 2021). However, labelling density is important to prevent overcrowding.

Overall, all the super-resolution methods described require complex optical systems or treatment of the sample to function, often needing dedicated facilities to manage the microscope systems (Table 1-1). There is a large time-component requisite for high-resolution images which is increased in the stochastic-based techniques. However, the ability to acquire images nearing the resolution of electron microscopy allows for the increased versatility of these techniques.

Whilst these techniques target the PSF to gather more information and improve resolution, expansion microscopy (ExM) takes a different approach.

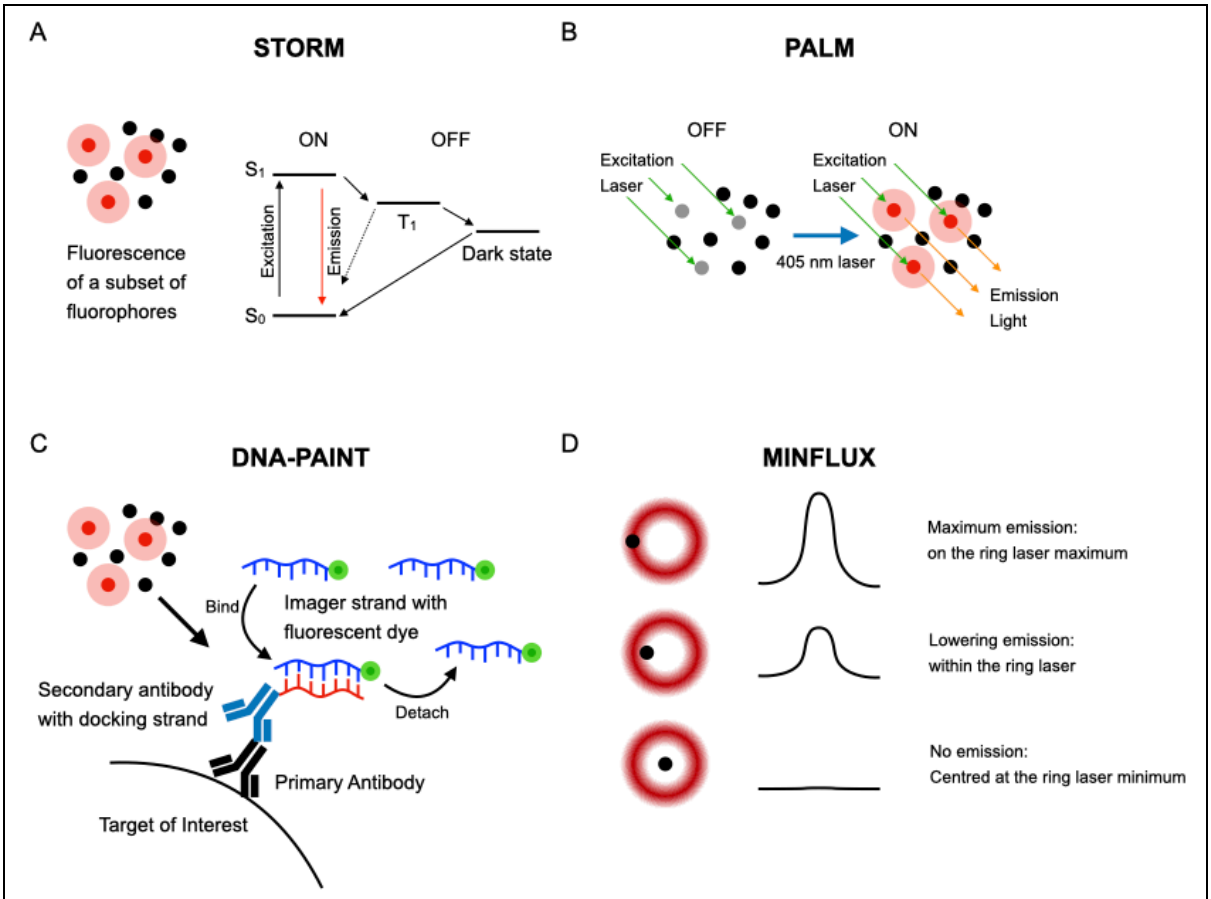

Figure 1-3: Mechanisms of STORM, PALM, DNA-PAINT and MINFLUX Techniques

Diagrams illustrating the following techniques: **A)** STORM: photoswitchable fluorophores are transitioned into the dark state, fluorophores 'blink' periodically creating an illuminating spatially separated subset. The acquisition of multiple frames can be used to localise and reconstruct the image. **B)** PALM: 405nm light-activated dye is used to control fluorescence under the excitation laser allowing separation of fluorophores and reconstruction of image after multiple frames.

C) DNA-PAINT: sample is bound with a docking DNA strand, imager strand with and associated dye can freely bind to the docking strand and release, in the process fluorescing. This creates a 'blinking' effect for imaging of spatially separated fluorophores. **D)** MINFLUX: ring-laser with central minimum is used to scan for signal. Where signal is found is indicative of a fluorescent marker, by reducing the emission to zero the marker can be localised to the centre of the laser and the position more accurately identified.

	Lateral (XY)	Axial (Z)	Advantages	Limitations
Confocal - Airyscan	120-150 nm	200-350 nm	• Fast • Works with classic staining approaches	• Limited super-resolution
4Pi	20-150 nm	10-150 nm	• Compatible with other SMLM techniques	• Complex system • Fixed sample
STED	30-100 nm	50-100 nm	• Moderate Speed • Primarily optical	• Complex system • Phototoxicity
SIM	90-140 mm	250-350 nm	• Works with classic staining approaches	• Limited super-resolution • Sample bleaching
STORM	20-50 nm	30-50 nm	• Great lateral resolution	• Slow • Amount of data • Specialised fluorophore
PALM	20-50 nm	30-50 nm	• Live and fixed samples • Great lateral resolution	• Slow • Amount of data • Specialised fluorophore
DNA-PAINT	20-50 nm	80-150 nm (TIRF)	• Large-scale multiplexing	• Slow • Imaging limited to near coverslip • Specialised fluorophore
MINFLUX	1-3 nm	1-3 nm	• Nanometer level resolution • Low phototoxicity • Live and fixed samples	• Slow, as needs low fluorophore density • Complex structures increase acquisition • Specialised fluorophore

Table 1-1: Comparison of Super-resolution Microscopy Techniques

1.3. Introduction to Expansion Microscopy

ExM, developed by Chen et al. (Chen et al., 2015), uses a swellable hydrogel matrix to physically expand the sample allowing for increased spatial separation and resolution of cellular ultrastructure (Figure 1-4). The technique used custom-made DNA-acrylamide handles and was compatible with most microscope systems including the ubiquitous confocal microscope. This allows for a large-scale democratization of imaging, bordering and stepping into the super-resolution field.

Initial inceptions of ExM relied on adaptation of fluorescent labels to contain a methacryloyl group to allow for polymerisation into the hydrogel matrix (Chen et al., 2015). However, with the creation of protein-retention ExM (pro-ExM), standard fluorescent proteins and labels could be used with the technique (Tillberg et al., 2016).

Modern ExM relies on traditional antibody labelling with primary and secondary antibodies. By binding these to Acryloyl-X, to create a functional acrylamide group, fluorophores are capable of being incorporated into the hydrogel matrix composed of sodium acrylate (swellable monomer), acrylamide (monomer, mechanical stability of gels) and N-N'-methylenebisacrylamide (crosslinker). This simplified the matrix composition as the DNA handles could be replaced with this anchoring process. The polymerisation process is initiated by ammonium persulfate (APS) and accelerated by tetramethylethylenediamine (TEMED) whilst incubated to produce the gel matrix. As the sample must be bound into the gel matrix it is important to note that ExM can only be performed on fixed samples, especially due to the next step, digestion.

A key component of ExM requires digesting away the sample once the gel has been formed. This allows the remaining fluorophores (~50% but vary by fluorophore (Tillberg et al., 2016)) bound to the matrix to freely expand with the hydrogel. This digestion step is often performed with proteinase mixtures specific to the type of sample with Proteinase K being the most common, capable of broad-scale cleaving of protein peptide bonds. This provides the added advantage of producing optically clear samples, as the biological material is digested away. However, it is important to manage digestion time as too much can degrade the fluorescence, whilst too little leads to incomplete digestion, in turn leading to distortions in the hydrogel.

With the addition of deuterated water, after the digestion step, the sodium ions in the hydrogel are displaced and the remaining abundance of negative charges repel, expanding the matrix. This process has resulted in the most common ExM recipes with expansion factors of four- (Tillberg et al., 2016) and ten-fold (Truckenbrodt et al., 2018).

The expansion factor here denotes the expected expansion of the hydrogel and the incorporated cellular structures. This allows for structures below the diffraction limit to be at a now resolvable distance and thus capable of being imaged without the need for super-resolution techniques. At the classical four-fold expansion this results in an Airyscan lateral spatial resolution of ~70 nm.

Due to heterogeneity in the gel formation the risk of anisotropy is possible as the gel expands. Additionally, handling of the gel can provide shear forces affecting the hydrogel mesh and introducing further avenues for anisotropy and distortion. Analysis

of the anisotropic nature of the ExM hydrogels has revealed a 1-4% error across their length scales (Chang et al., 2017; Chen et al., 2016, 2015; Chozinski et al., 2016; Damstra et al., 2022; Tillberg et al., 2016). Hence it is important to investigate and be aware of the distortions created by these anisotropies.

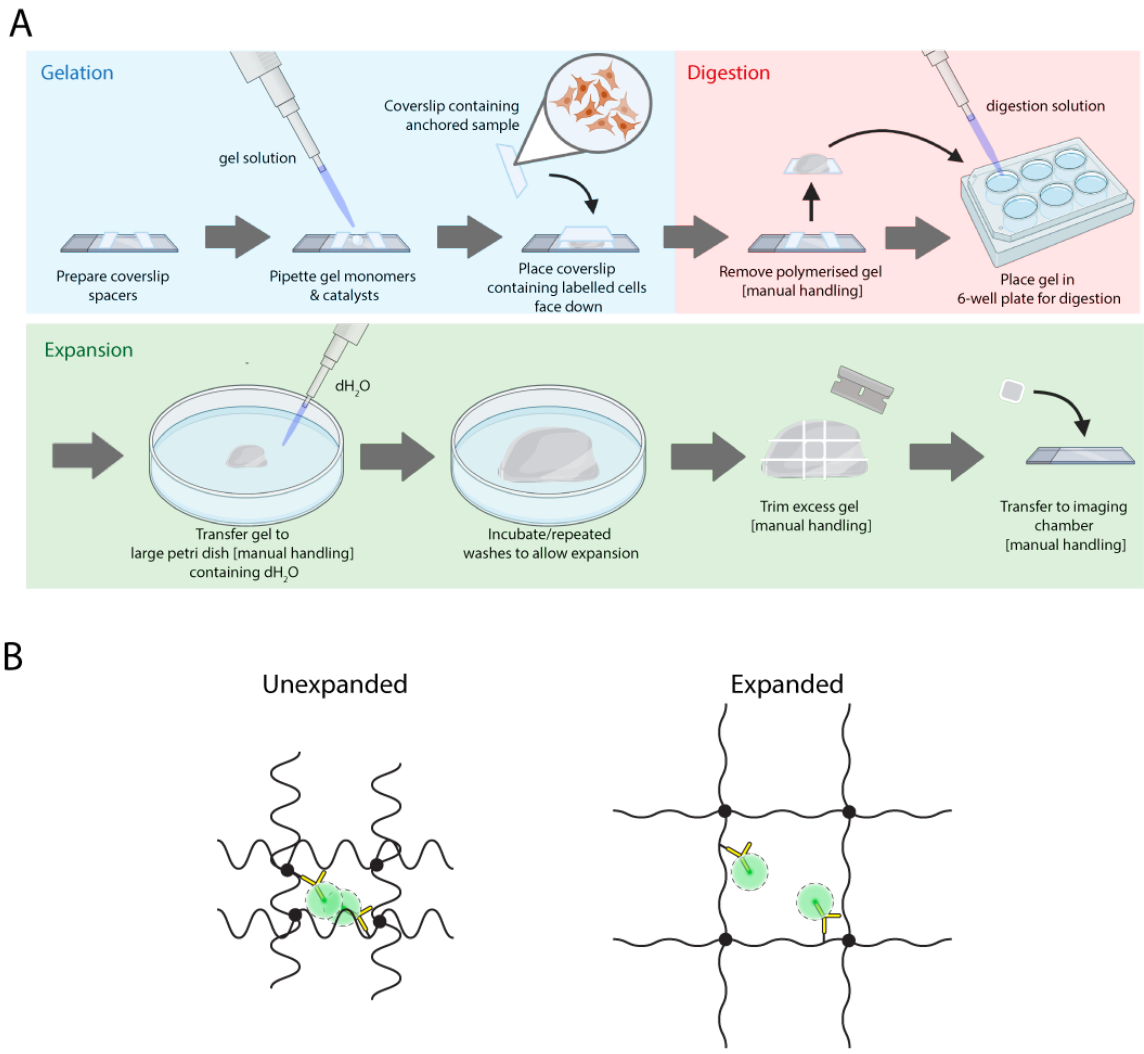

Figure 1-4: Schematic illustration of the Classical ExM method.

The panels illustrate the approach to ExM and how the hydrogel is cast, handled, the expansion process, and prepared for imaging. **A)** Expansion protocol from gelation stage, illustrating stages where manual handling of the gel is required. Adapted from (Seehra et al., 2023). **B)** Illustration of the spatial separation of fluorophores as part of gel expansion in ExM.

1.3.1. Principle and the Main Variations of ExM Recipes

Pro-ExM has provided a reliable four-fold expansion methodology with wide application. The simplicity of implementation combined with the ease of use has made this a widely accepted ExM recipe, with applications in both cultured cells and tissue samples (Chozinski et al., 2016; Sun et al., 2020; Tillberg et al., 2016; Wen et al., 2020).

At the ten-fold scale, the use of N,N-dimethylacrylamide (DMAA) as a crosslinker, created a gel recipe further expanding upon the capabilities of ExM and becoming a standard for recipes at that expansion range. The gel process is adjusted to be initiated with potassium persulfate (KPS) and requires strict polymerisation conditions. Specifically, elimination of oxygen prior to polymerisation through nitrogen purging, this allows the DMAA polymerisation. This process generates sulfate and hydroxyl radicals, which propagate polymerising the monomer components together. DMAA as the crosslinker also polymerises at the methylene group to create the 3D hydrogel matrix. In spite of these limitations, reports of up to 25 nm resolution demonstrate the efficacy of the technique, whose only other imaging limit requires thin samples of less than 50 microns (Klimas et al., 2023; Truckenbrodt et al., 2018).

1.3.2. Ultrastructure Expansion Microscopy

Using these principles and methods, we can further adjust the components to produce variations of expansion microscopy. Each form of expansion microscopy aims to target a specific task.

Digestion causes a loss in target proteins in post-expansion, this results in a reduction in the signal-to-noise ratio as less antibodies remain. A method to alleviate the loss was found in magnified analysis of the proteome (MAP) (Ku et al., 2016) wherein when fixing the sample, acrylamide was used to prevent crosslinking of endogenous proteins with formaldehyde. Samples could be softly denatured, retaining epitopes for post-expansion labelling.

This strategy was used in ultrastructure ExM (U-ExM) to preserve organelles and cellular ultrastructure with a focus on centrioles (Gambarotto et al., 2019). This revealed a difference in expansion factor between Pro-ExM and MAP based methodologies, because of the different denaturing methods, in particular, soft-denaturing methods are often more restricted in their expansion factor as structures remain to limit the expansion.

1.3.3. TissU-Expansion Microscopy

TissU-ExM (Steib et al., 2022a) was developed to address suboptimal staining efficiency in dense structures and samples (Freifeld et al., 2017; Sim et al., 2022). By adapting: the MAP-based acrylamide concentration when fixing, the denaturation temperature, and the incubation time, it was possible to achieve a four-fold expansion of zebrafish samples. This expansion appeared isotropic and free from large-scale distortions, an inherent and prominent problem with the expansion technique in tissues.

1.3.4. Ten-Fold Robust Expansion Microscopy and Magnify

Ten-fold robust expansion microscopy (TREx) (Damstra et al., 2022), was subsequently developed to address prominent distortions, and provide a more robust methodology functional in a variety of sample types. Through systematic investigation of the crosslinker concentration and gelation conditions the recipe could be tuned to the required expansion factor, whilst producing robust gels.

The TREx recipe uses the same chemicals as the Pro-ExM method, and the reduction in crosslinker concentration allows for less restriction in expansion due to reduced binding locations of the crosslinker.

TREx demonstrated capabilities in both cultured human cell samples and thick mouse brain tissue sections, taking advantage of important lessons from the previous techniques (Damstra et al., 2022).

The recently developed Magnify recipe uses a similar approach of crosslinker adjustment and monomer changes to include DMAA to allow for robust eleven-fold expansion. Klimas et al. demonstrated the efficacy of the technique using tissue samples including mouse brain tissue and human kidney cell samples (Klimas et al., 2023).

1.3.5. Iterative Expansion Microscopy

In further attempts to increase the scale of expansion, iterative approaches were explored. Iterative ExM (IExM) expands a sample up to twenty-fold through successive

four-fold expansions. By using cleavable crosslinkers, samples could be initially expanded before being embedded in a polyacrylamide gel for the subsequent iteration. The crosslinker for the original gel is cleaved allowing the second iteration of expansion. With application in both culture cell and mouse lung and liver tissue samples, structures with a 20 nm resolution were resolvable (Chang et al., 2017).

The authors also theorised a third iteration bringing the resolution even closer to the angstrom level.

1.4. Combining ExM with Other Super-Resolution Modalities

The spatial separation of fluorophores, provided by the volumetric expansion of ExM, allows for an improved resolution. However, with the intention of being used on classical diffraction limited microscopes, there is a barrier to further insight. Combining the biological approach ExM uses to confront the diffraction limit with the biological resolution provided by super-resolution techniques, it is possible to gain further insight into cellular ultrastructure at scales rivalling electron microscopy.

1.4.1. Enhanced Expansion Microscopy (EExM)

Confocal microscopy uses a pinhole to reduce the out-of-focus light allowing for image reconstruction wherein the PSF is notably smaller and in turn increasing resolution up to two-fold. Using Airyscan, in which a multi-element detector array allows for algorithmic pixel reassignment, combined with ten-times expansion methods, it is possible to acquire resolution nearing 15 nm in the lateral plane and 35 nm axially (Sheard et al., 2019; Sheard and Jayasinghe, 2020). This increase in axial resolution

was not limited to regions closer to the coverslip, demonstrating a marked improvement over other super-resolution techniques.

The use of confocal microscopy with ExM recipes is a standard efficacious approach to acquiring ExM data at reasonable speed and resolution.

1.4.2. ExSIM and Investigating Human Pathogen *Giardia lamblia*

By combining ExM with structured illumination microscopy (SIM), a spatial resolution of 30 nm has been achieved (Halpern et al., 2017). SIM uses a diffraction grating to create illuminated strips across the image plane (the Moiré effect), this creates an interference wherein higher frequency information in the sample becomes lower frequency and thus better gathered by the objective lens. By rotating and translating the diffraction pattern we can reconstruct the image by adjusting the data in Fourier space.

Using the pro-ExM four-fold recipe with the two-fold resolution improvement from SIM, the resolution is able to reach comparable levels to other super-resolution modalities. This technique was tested in *Giardia lamblia*, a protozoan known to cause giardiasis (Ankarklev et al., 2010), whose disc-associated proteins are below the resolution of classical confocal ExM.

SIM requires the acquisition of multiple exposures per image plane to reconstruct the higher resolution image. This introduces a greater risk of photobleaching the sample during the acquisition process as a higher light dose is delivered relative to a single

image. There is also a requirement for minimising sample drift, a common issue in ExM experiments.

Drift was addressed by using a lysine coating on the coverslip producing a positively charged layer attracting the negatively charged hydrogel. Whilst the photobleaching was reduced by minimising the number of images per plane.

Altogether this resulted in comparative resolution between ExSIM and 3D single-molecule approaches, with ExSIM having an overall advantage particularly in the axial direction. This highlights the importance of the spatial separation of ExM as denser regions may become difficult to resolve by super-resolution approaches alone. However, in combination with ExM these high-density structures can be isotropically expanded, separated and therefore, better resolved.

Further applications of this approach include imaging of *Drosophila* synaptonemal complexes (Cahoon et al., 2017; Wang et al., 2018).

1.4.3. ExSTED

Expansion microscopy has also been combined with STED microscopy, creating ExSTED, wherein, microtubules, nuclear pore complexes (Li et al., 2018), cilia and centrioles have been imaged (Gao et al., 2018).

Similarly, these combined a four-fold expansion approach with the resolution improvements inherent to the STED imaging modality. Thereby, allowing for up to 10 nm resolution in the 2D data and 50 nm resolution in 3D.

Due to the similarities between confocal and STED, in that of point scanning, this approach does not require an extensive rework of the protocol and imaging methods to function. However, the decrease in spatial density of the fluorophores inherent to ExM and signal loss from pre-expansion imaging, resulted in a requirement of post-expansion labelling to bolster the signal to acquire images with STED (Gao et al., 2018).

1.4.4. ExSMLM

STORM requires a photoswitching buffer to permeate the sample to create the signature effect required for the technique. However, the ExM hydrogels are classically negatively-charged due to the displacement of sodium ions during the expansion process. Hence, Zwettler et al. successfully implemented a charge-neutral polyacrylamide gel that the expanded sample was re-embedded into (Zwettler et al., 2020).

The authors illustrated that linkage error is an important factor affecting the quality of post-expansion imaging. By using post-expansion labelling methods they obtained a lateral resolution of 10 nm, observing the 9-fold symmetry of the procentriole.

This method is limited by the size of the fluorescent molecules used to stain the samples, as well as the impact of distortions at smaller length scales. Whilst post-ExM

labelling reduces the linkage error, the accuracy of labels is directly impacted by their size. Therefore, moving from a primary and secondary antibody approach to smaller nanobody approaches could provide a way to reduce this issue, specifically in pre-expansion labelling as this could reduce the risk of antibodies being bound into the hydrogel matrix in multiple places and thereby being displaced by the expanding matrix (Shaib et al., 2024).

Distortions exist at all scales of ExM (Chen et al., 2015) and when localising features at the smallest of scales of the matrix, this will impact the accuracy of inferred structures. The existence of distortions less obvious to observation have a substantial impact on the reliability of the post-expanded structures, hence being aware of these small-scale distortions allow an accurate representation of the limits of the data presented and the structures imaged. The impact of distortions is sample specific and will therefore, reduce the repeatability of experiments at this scale, impacting the reliability of the ExSMLM technique.

1.4.5. Other Innovative Applications of ExM

To increase the image acquisition speed, light sheet microscopy has been combined with ExM. This allowed for simpler 3D reconstruction of the large tissue samples used whilst retaining high resolution and cellular ultrastructure (Düring et al., 2019; Bürgers et al., 2019; Chakraborty et al., 2019; Lu et al., 2023). In clinical tissue specimens, ExPath was developed to allow expansion of paraffin-embedded samples (Zhao et al., 2017). An ExM method for breaking down the bacterial cell wall, μExM, was developed by using specific digestion components that target this structure (Lim et al., 2019).

Lipid imaging is notoriously difficult in ExM as they are non-polar structures, hence mExM was created to address this (Karagiannis et al., 2019).

The optical clearing and de-crowding offered by ExM allows for, super-resolution radial fluctuations (SRRF), wherein the fluorescence intensities are analysed both radially and temporally. This technique's resolution is classically limited by overlapping fluorophores, hence combining this method with 10X ExM and STED imaging, resolution approaching 1 nm has been reported (Shaib et al., 2022).

1.5. Introduction to NHS Ester Staining and Applications

ExM combined with super-resolution techniques offers valuable nanoscale insight into structures bordering the molecular level, however the broader cellular layout and arrangement in context to this information remains less explored.

The use of amine reactive *N*-hydroxysuccinimide (NHS) esters have been developed allowing visualisation of cellular compartments. NHS esters (when affixed with a fluorophore) provide a method of widespread, nondescript staining, as the NHS esters react with primary amines to create stable amide bonds releasing the NHS molecule. Therein, allowing for identification and interpretation of compartment structures, cells and tissues, all of which contain amine groups available for binding. This additional context provides a method by which to assess the molecular structures of interest against the local ultrastructure (M'Saad and Bewersdorf, 2020).

Using NHS esters with ExM, has allowed for imaging at various scales to assess: cellular compartments (Damstra et al., 2022; Lee et al., 2022; Louvel et al., 2022; Sim et al., 2022), molecular organisation (Bertiaux et al., 2021; Chacko et al., 2023; Hinterndorfer et al., 2022; Yu et al., 2020), and the conformation of individual proteins (Shaib et al., 2022). This has allowed for structural analysis both with and independent of direct antibody labelling.

For example, fluorescent labelling of abundant reactive entities (FLARE), marked a novel method to stain samples, by changing the target of classical fluorophores from a specific biomolecule to the abundant functional groups in the sample. This was performed by adjusting the fluorescent labels with a functionalized NHS group to allow for amine labelling throughout the sample. Thereby, a wide range of structures and organelles can be stained in a nonspecific manner. This method showed wide scale application in both cultured and tissue samples with hydrogel compatibility, allowing for ExM (Lee et al., 2022).

Recent work has shown that the labelling pattern of NHS ester dyes varies between pre-expansion, inter-digestion and post-expansion applications. In pre-expansion labelling, the NHS ATTO647N dye showed mitochondrial and nucleoplasm labelling, however, the nucleoplasm labelling was absent from inter-digestion labelling time point (Sheard et al., 2023).

Interestingly, applying multiple NHS esters simultaneously also resulted in an interaction and change in labelling pattern. This has been attributed to Förster Resonance Energy Transfer (FRET) based interactions between the dyes and

influenced by the order of application. This results in signal retention of the dye post bleaching due to energy interactions with the other NHS ester being closely bound allowing for FRET between the two fluorophores. For example, NHS ATTO647N was bleached, however, this led to a corresponding ~85% reported increase in the fluorescence of the NHS Alexa488 dye channel, with no change in labelling pattern.

In summary, NHS ester labelling provides a broad-scale staining method with a nondescript pattern of labelling. The variability in the labelling pattern does not seem to be compartment bound, and therefore, characterisation of NHS esters is important to understand the context they can be applied in. Conversely, they are fluorescently bright and robust allowing for retention post-expansion, an advantage over regular pre-expansion immunolabeling methods.

1.6. Validating Expansion Microscopy Data for Isotropy

ExM is built on the core concept of the physical expansion of the sample to achieve super-resolution data. However, the potential anisotropy of this expansion, resulting from heterogenous hydrogel formation and incomplete digestion, can result from and cause several forms of distortion. Large-scale distortions are more commonly caused by incomplete digestion and are more apparent. Generally allowing for samples sufficiently affected to be discarded early in the experiment. However, small-scale but global distortions are more difficult to perceive and can influence the accuracy of the expanded structures. Therefore, the degree to which we can comment on the structures present in the post-expanded image is limited by these distortions. To

assess both qualitatively and quantitatively the degree of anisotropy, it is necessary to interrogate the data.

There are several methods to investigate the anisotropy including: pre-/post-expansion comparison of the same regions, landmark-based calculations, and averaging of structures of interest in both pre-and post-expansion samples.

In their landmark paper, Chen et al. use the pre-/post-expansion comparison between the same regions to assess distortions and noted a 1-3% anisotropy in the hydrogels (Chen et al., 2015). This was performed by imaging the same cells in pre-expanded and post-expansion states, aligning the data and using a non-rigid registration method to extract the nanoscale distortion information. This distortion data was then displayed in a vector map, qualitatively illustrating the differences in the same cell between the unexpanded and expanded states.

This distortion data was further used to create a qualitative assessment, wherein, the distance between points in each image were compared and the root-mean-square error (RMSE) of the difference was plotted against the original distance between the points. This was performed for every point in the image pair to acquire the RMSE as a function of length measurement. This allowed for an understanding of the scale at which distortions were prevalent and thus the percentage error in measurement across the image. This remains the golden standard and benchmark for ExM validation.

A derivative of this method by Truckenbrodt et al. uses rigid registration methods and optical flow calculations to obtain distortion information before generating distortion

maps and RMSE data (Truckenbrodt et al., 2019). The use of rigid registration methods implies a base assumption of isotropy; hence the alignment uses the similarity-based transformations of translation, rotation and uniform scaling. The optical flow algorithm then assesses the difference between the two images to generate the distortion data at subpixel levels. Briefly, this is performed by comparing gaussian blurred sub-regions in both images and best matching the regions within the context of the whole image. In turn the transformation data from both rigid and non-rigid methods can be used to acquire the expansion factor.

Both methods discussed thus far require the acquisition of pre-expansion and post-expansion images from the same region. However, due to the inherent difficulty in finding and acquiring images from the same region, alternative methods have been devised. The use of landmark-based calculations and averaging methods, forgo this requirement, instead opting for increased numerical data (Amodeo et al., 2021; Büttner et al., 2020; Kunz et al., 2019; Mascheroni et al., 2020; Wen et al., 2021a). This results in a greater focus on the expansion factor and less on small-scale distortions. Thereby, reducing the reliability of ExM data at small-scale and therefore, limiting the resolution gain and the accuracy of small-scale structures of interest in the post-expansion data. As ExM has the capacity to bring structures below the diffraction limit to above the diffraction limit, it becomes increasingly important to identify distortions at these scales to understand the resolution and accuracy of the data.

Image registration methods were originally developed to aid in the medical field. Data from MRI and CT scans required alignment to interpret the information from each in context (Wells III et al., n.d.). Hence, normalised mutual information, data shared by

both images after the pixel intensities have been normalised, was used to develop the initial rigid and affine transformations (Maes et al., 1997).

As the techniques became more advanced it became apparent that local deformation was occurring in soft tissue. These deformations were non-rigid and hence the b-spline algorithm was developed to account for and correct these deformed regions (Rueckert et al., 1999; Ashburner and Friston, 2005). This has resulted in modern advancements such as Elastix (Klein et al., 2010).

1.7. Limitations of ExM

As a technique, ExM remains a fixed sample imaging method due to the necessity of digesting and physically expanding the sample. Fixing is classically done through paraformaldehyde (PFA) fixation, wherein PFA acts to crosslink macromolecules in the structure by reacting with amine groups on proteins and nitrogen containing structures. In situtions where PFA is insufficient glutaraldehyde can be used in conjunction with PFA to assist in crosslinking structures. , The option of cryo-fixation exists for cryo-ExM imaging (Laporte et al., 2022), this consists of plunge-freezing the sample in liquid ethane (as cooled by liquid nitrogen) and storing in chilled acetone for storage at -80 degrees celsius. Subsequently, when the sample is required, they are allowed to warm at room temperature and then rehydrated in successive ethanol baths into PBS.

Beyond this there are several other areas that limit the applicability and usability of the technique. These primarily include: variability and inconsistency, dye compatibility, and distortions.

1.7.1. Variability & Manual Handling

Expansion sample variability arises from three sources: anisotropic gel expansion, experimental differences, and manual handling of the hydrogel.

Gel anisotropy can vary sample-to-sample with gels prepared at similar times showing different expansion factors. As most gels start to polymerise swiftly once the initiator and accelerator are added, this can lead to a difference between the first and last gel created. Specifically, the viscosity of the gel mixture changes rapidly within the first minutes of combination. If not applied rapidly to the sample, the gel mixture will have polymerised sufficiently enough to raise concerns over the components ability to penetrate into the sample to form the hydrogel effectively.

In particular, aspects such as digestion length can affect the quality of the remaining fluorescence (Chozinski et al., 2016), presence of distortions from incomplete digestion, and therefore the expansion factor (Park et al., 2019). Anecdotally the handling of and age of components such as sodium acrylate can impact the quality of a gel.

Manual handling at each stage contributes to this variability, introducing avenues for additional physical influence on the gel that could result in distorting the contained sample. From moving the initial gel to a chamber for digestion and expansion, to cutting up and transferring gel pieces for imaging, each stage risks damage to the gel. In the traditional method, manual handling is required to move the gel for each stage of the experiment, especially as the gel expands (Figure 2A).

Combined with a 1 - 4 sample throughput per experimental run, the number of factors influencing the variability remain high and are primarily mitigated by a skilled researcher.

1.7.2. Dye Compatibility

Whilst initially a larger problem, since the inception of pro-ExM many antibody dyes are now accessible. However, the harsh radical-rich polymerization and digestion steps can cause fluorescence loss as fluorophores are variably vulnerable to being broken down through overdigestion (Chozinski et al., 2016). Signal retention can vary widely with standard fluorophores, such as Alexa 488 retaining 57.2% of its signal (Chen et al., 2015) between pre-/post-ExM stages. The development of photostable dyes for ExM remains an area of exploration.

1.7.3. Distortions and Artefacts

Structure density and biological heterogeneity can result in challenges for ExM. The compact nature of DNA in the nucleus or the layered cell wall pose as barriers to thorough digestion. This can give rise to distortions and artefacts, through the incomplete or insufficient digestion and the permeability of the gel matrix into these denser regions (Norman et al., 2024).

Broadly, distortions can range from: tearing, where expansion is resisted; shearing, where the area between resisted regions is stretched; and local area expansion heterogeneity, where the structure expands but to a different degree than the rest of the sample (Figure 1-5).

Tearing is primarily a problem in tissue and whole organism ExM protocols, with specific digestion protocols being used to address this. For example, in *Drosophila* larvae, slowing polymerisation allows for increased monomer permeation into the gel and subsequent chitinase digestion works to better break down the biology (Jiang et al., 2018).

Shearing would indicate non-uniform expansion of the sample and the expansion factor would deviate in each axis. For example, measurements of microtubule diameters should scale with the expansion factor in all directions as these structures lie at various orientations in a sample space. Variation in the diameter would indicate non-uniformity and the direction of distortion and shearing could be isolated. Specifically for microtubules, this error tends to remain at 1-4% with greater deviation for tissue samples over cells (Chang et al., 2017).

Local area heterogeneity remains a large issue for expansion. From incomplete digestion to sample heterogeneity, the number of factors causing this issue are being gradually reduced. Expansion protocols are continuously being optimised for cell (Truckenbrodt et al., 2019; Damstra et al., 2022; Gambarotto et al., 2019) and tissue (Chakraborty et al., 2019; Damstra et al., 2022; Steib et al., 2022a) samples alike. In turn, methods to optimise monomer infiltration and digestion protocols have arisen, providing a wealth of options to target distortions.

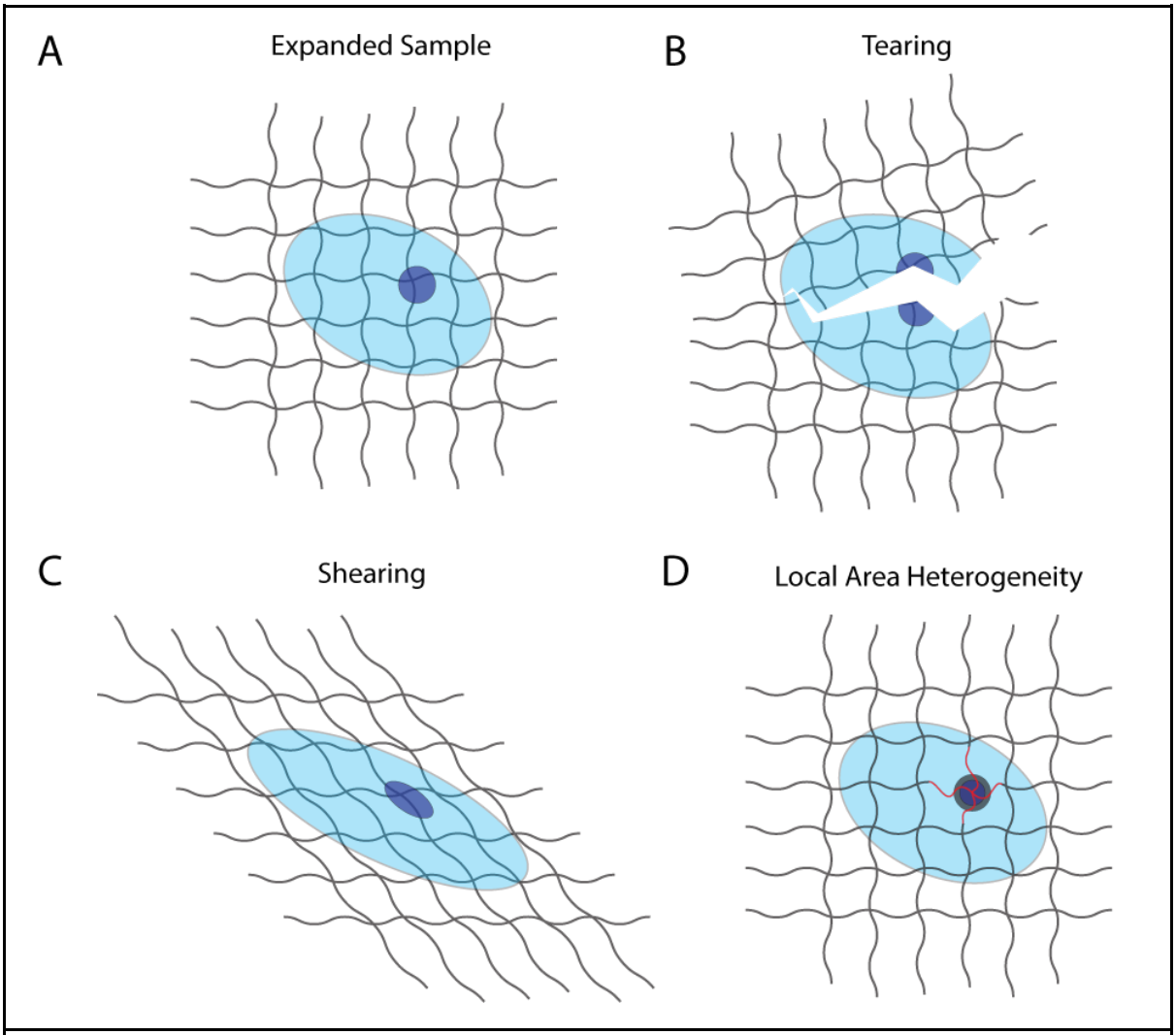

Figure 1-5: Schematic illustrations of common distortions in ExM

The panels depict a cell embedded in the hydrogel mesh showing various deformation under the presence of distortions. **A)** Expanded sample with no distortions present. B) Distortion of gel by tearing of the sample. **C)** Distortion of the sample by shearing forces anisotropically stretching the sample. **D)** Local area heterogeneity resulting in reduced expansion of internal cellular structure.

The understanding and elimination of the causes of these distortions has allowed researchers to investigate factors related directly to the sample. Regions of a cell that reduce the access of polymerisation reagents are associated with greater distortion

producing these local effects. This reduction in access leads to heterogeneity in the gel matrix and less efficient digestion in these regions leading to distortions. Practically, this includes compartment boundaries (Büttner et al., 2021; Pernal et al., 2020; Seehra et al., 2023) and chromatin dense regions (Martínez et al., 2020; Norman et al., 2024) as two key areas. Distortions inhibit the reliability of the expansion data collected with larger distortions invalidating samples, and smaller distortions limiting the quantitative value of the image data.

Overall, the presence of distortions are ubiquitous in ExM and it remains important to characterize and validate ExM data to provide appropriate context to the information presented. In particular, when imaging structures close to the resolution limit of the ExM experiment, understanding the accuracy of the results and the degree of error present is vital in interpreting the results.

1.7.4. Variation in Validation Approaches to ExM

As mentioned prior, the benchmark for expansion microscopy requires pre-/post-expansion imaging of the same region to allow for distortion analysis and RMSE calculations. However, the inherent difficulty in this process has resulted in alternative approaches being introduced. In combination with the increasing trust in ExM due to previous validation, this has resulted in only a small portion of literature conducting the gold standard approach.

From a sample set of 197 of the ~400 journal articles using ExM, distributed from 2015 to the end of 2023, 82 journal articles (41.6%) used pre-/post-expansion imaging with

27 (13.7%) further validating with RMSE as a function of length measurement (Figure 1-6).

The expansion factor was considerably more often calculated at 123 articles (62.4%) publishing this data. The expansion factor was often calculated in novel ways with the structural averaging being the most common. Of the 82 articles that published pre/post-expansion images, 59 calculated the expansion factor. Those not using registration methods to calculate the expansion factor used macroscale pre-/post-expansion measurements of the physical gel and structural averaging (as mentioned above), with several papers reporting an expansion factor but omitting the methods by which it was acquired.

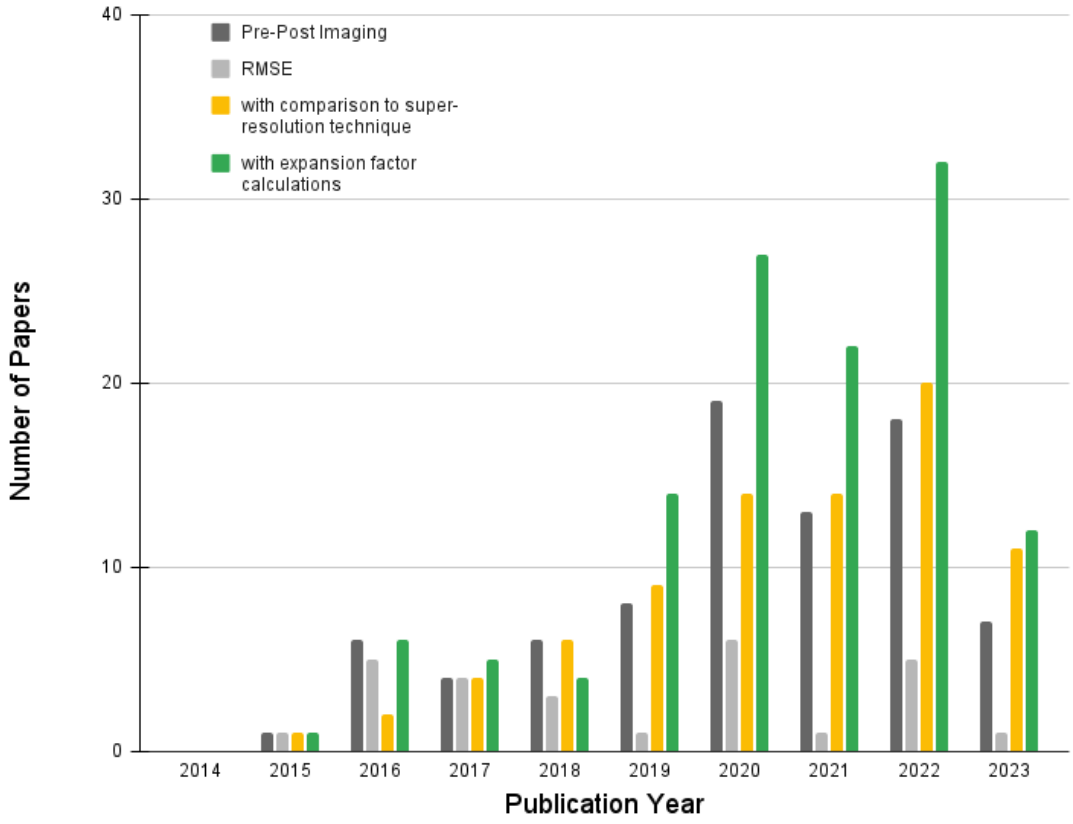

Figure 1-6: Bar chart of ExM validation approaches used in a subset of published ExM journal articles from 2014 to 2023

The chart shows the number of papers that include, pre-/post expansion imaging (black), RMSE calculations (grey), comparison to super-resolution techniques (yellow), and expansion factor calculation (green). The results show an increase in the variability of the validation approaches used.

1.7.5. Areas Not Sufficiently Explored in ExM

The landscape of expansion microscopy has been growing since its inception in 2015, showing an increasing number of published papers every year since (Figure 1-7). The majority of the development has been focused on improving the protocol and increasing the number of applications to the technique which has resulted in a large influx of papers showing biological application in recent years.

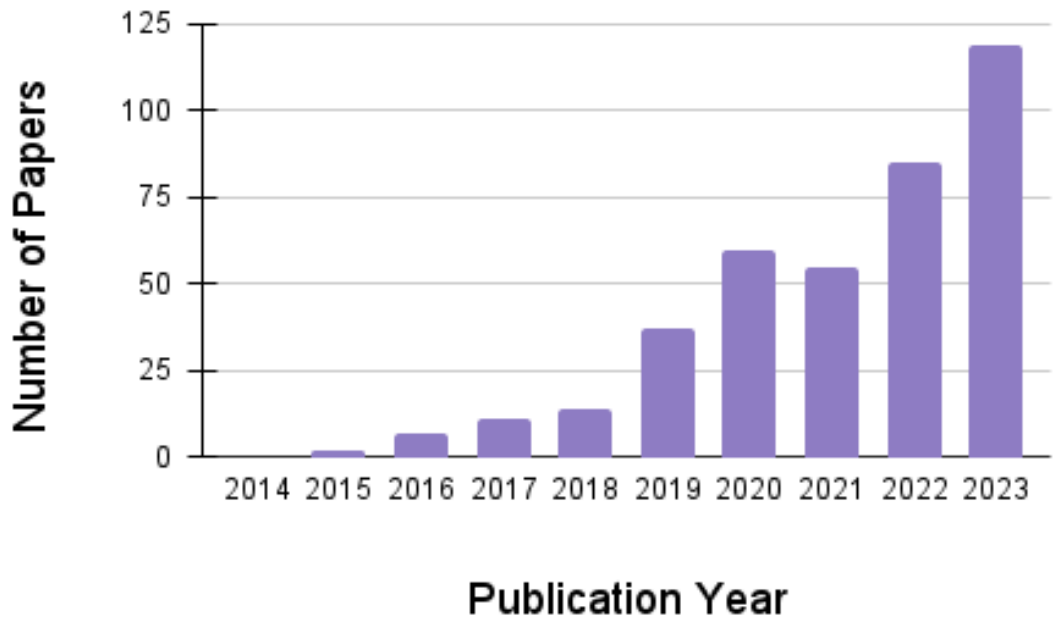

Figure 1-7: Bar chart showing the annual number of published papers using ExM from 2014 to 2023

The increasing trend in papers since the initial inception of the technique in 2015 with a particularly rapid growth rate after 2019, shows the rising research output of ExM.

However, several areas remain uncovered that could improve the accessibility, usability and functionality of the technique. High-throughput of ExM remains widely unexplored, with recent attempts in 96-well plates showing some result whilst being compatible with standard microscopes and automated systems (Day et al., 2024). However, this system is designed for automation and is a large step from the current slide-based approach. This difference in approach from a functional, expertise-limited slide-based approach to an automated plate-based multi sample system, shows the scope of development available to ExM. A plate-based approach that increases the

throughput of ExM and thereby increasing consistency and robustness would allow for more adaptability and greater research scope till the technique is considered competent enough to be fully automated as per Day et al. 2024.

A foray into programmed fluidics and similar robotic systems could provide a system for the relatively simple expansion experiment to be performed automatically. No published attempts have been made towards this yet and could assist in reducing variability between samples.

Finally, as the primary focus of ExM development has been on novel recipes, few papers have attempted to tackle the tools and techniques required to perform ExM. Whilst a broadly simple technique, there is a steep learning curve for new users to obtain usable data. This is primarily due to the manual handling of coverslips, gels, and other components requisite for the process. Additionally, the acquisition of pre-/post-expansion data remains a difficult task even for veterans of the technique.

Photo-ExM provides one attempt to reduce the gel variability by controlling the polymerisation process (Günay et al., 2023). However, the additional tools and materials contradict the concept of democratization that underlies ExM. Therefore, robust tools that are usable without the need for specialised microscopes and that reduce the complexity of sample preparation would assist in moving the technique forward.

1.8. Aims and Objectives

The main scope of this thesis addresses expansion microscopy and its functionality as a technique. Whilst ExM is an alternative approach to obtaining high-resolution and super-resolution image data, especially as a cheaper and less resource intensive variant, it lacks robust reproducibility and consistency. Given the need to optimise the ExM approach per sample type and potential for sample loss due to human error, it is evident that there are opportunities for improvement. Addressing these insensible losses, increasing consistency and reducing the barrier to entry is the first goal of my project.

In tandem with this, the analysis avenues to understanding isotropy in ExM and the reliability of the acquired data, has numerous approaches. Bespoke software is a necessity to standardise this process and provide a baseline for the comprehension of expansion microscopy datasets. By streamlining the concepts envisioned in the original Chen et al. (2015) paper with novel approaches, we aim to develop such a piece of code to be widely usable and easy to run, homogenising the analysis approach.

Thus, in Chapter 3 we introduce the development towards our solution to increasing the reliability of the technique with key aspects limiting the technique being addressed.

Chapter 4 revolves around demonstrating the tools developed and their efficacy with the 4x ExM protocol. By benchmarking this approach against the gold standard method of pre-/post-expansion imagining of the same region, we thus explore the analysis and key assumptions we make as part of understanding our expansion data.

With having established a new approach, Chapter 5 aims to push the applications of ExM further through exploration of the 3D environment. In particular, aiming to understand isotropy of the gel in all 3 dimensions and the hypothetical increase in XYZ spatial resolution inherent to ExM.

Chapter 2. Methods

This work is based on work published in Seehra et al, 2023 (Seehra et al., 2023)

2.1. Cell culture

A solution of Dulbecco's Modified Eagle Medium (DMEM) with high glucose, 4-(2-hydroxyethyl)piperazine-1-ethanesulfonic (HEPES), L-glutamine, 10% fetal bovine serum (v/v; Cat no. 17563595, LabTech International Ltd, UK) and Phenol Red (Fisher Scientific Ltd, UK) was used to culture cells. This solution was complemented with 1% Penicillin-Streptomycin (v/v; containing 10,000 units/mL of penicillin 10,000 µg/mL of streptomycin in a 10 mM citrate buffer; Fisher Scientific Ltd). Incubation was conducted as standard at 37°C and 5% CO_2 and upon confluency of ~ 70-80% cells were seeded. This is usually 2 days post passage.

Microplate chambers were initially sterilised via a 70% ethanol (v/v) spray down followed by placing them into a sealed bag and subsequently UV irradiated for 30 minutes. The glass coverslip (attached prior to the microplate) was coated with 0.01 mg/ml Poly-D-Lysine (code: 3439-100-01, Cultrex) for 2 hrs at 37°C and 5 % CO_2. Following the excess being removed, 0.05% Trypsin-EDTA (Cat no. 25300054, Fisher Scientific Ltd), was used to detach cells. Which were spun down at 400g for 5 minutes and resuspended in fresh medium. This suspension was seeded onto the microplates at a cell density of 75,000 /ml (1 ml of resuspended cell mixture per well). Microplates were cultured at 37°C and 5 % CO_2, with media replacement every 24 hrs till ready for use 2 days later.

Cell Line	Source Number	Source
Human cervix epithelioid carcinoma cells	HeLa-CCL2	European Collection of Authenticated Cell Cultures (ECACC)
hTERT retinal pigment epithelial cells	CRL-4000	American Type Culture Collection (ATCC)

Table 2-1: Table of cell lines, source number and source

2.2. Fly Wing Dissections

This work was performed by Samantha Warrington and has been included with her consent.

2.2.1. Experimental Model and Subject Details

Drosophila melanogaster flies were grown on standard cornmeal/agar/molasses media at 25°C.

2.2.2. *Drosophila* Wing Immunostaining and Antibodies

Dissection of *Drosophila* pupal wings was performed at 28 hrs after puparium formation at 25°C. After sticking down the pupae, the cuticle was removed and the pupae were fixed by placing them in a drop of 4% PFA (Fisher Scientific Ltd) in PBS (tablets dissolved in dH2O; Fisher Scientific) for 30 mins at room temperature. After which the pupal wing was dissected from the pupal carcass and fixed for an additional 10 minutes prior to removing the inner cuticle.

2.3. Immunolabeling

2.3.1. Immunostaining

Cells were fixed 1-2 days post-plating in 2% PFA (1ml 4% PFA. 1ml fresh medium, Fisher Scientific Ltd) for 10 minutes, following which 3 x 10-minute washes in PBS were performed. A storage solution of PBS containing 0.5% bovine serum albumin (w/v, Gibco, Thermo Fisher Scientific) and 0.1% sodium azide (w/v) was used to maintain the fixed cells (stored at 4°C) till immunostaining.

Permeabilisation of cells was conducted in PBS (137 mM NaCl, 2.7 mM KCl, 10 mM Na_2KPO_4, 2 mM KH_2PO_4, pH 7.3) + 0.1% (v/v) Triton X-100, and later blocked in PBS with 10% normal goat serum (NGS; v/v) and 0.05% Triton X-100. Antibody incubation solution (0.05% Triton, 2% NGS in PBS) with the addition of 1:200 primary antibody was used for immunostaining with 200 µl of the solution being added to each well and then incubated overnight at 4°C. Samples were washed with PBS every 5 minutes for a total of 3 times. After which 1:200 secondary antibody was applied with 200 µl per well for 2 hrs at room temperature. Samples were washed again with PBS 3 times with 20-minute intervals.

In the instance of NHS ester application, once cells are permeabilised, 200 µl of 1:1000 NHS ester in ester staining solution (100 mM $NaHCO_3$ + 1 M NaCl, pH 6, made up to 100 ml with dH_2O) was used per well for immunostaining. Samples were incubated for 1 hr 30 mins at room temperature and then washed 3 times with 20-minute intervals, after which the blocking step could be conducted.

2.4. Expansion Microscopy

2.4.1. Anchoring

To prepare linking the fluorophores into the gel, samples were incubated in 250 µl of PBS and 1% Acryloyl-X (w/v; Catalogue number A20770, Fisher Scientific) at 4°C overnight.

2.4.2. 4X Gel Preparation

Samples were washed with PBS 3 times with 20-minute intervals. Following which incubation in 200 µl of monomer solution (sodium acrylate (Sigma-Aldrich), acrylamide (Sigma-Aldrich), MBAA (Sigma-Aldrich), NaCl, PBS, dH20) for 30 minutes at 4°C. Following this the monomer solution was taken off, and the silicone frame insert was firmly placed into the well, maximising the contact between the insert and the coverslip. 100 µl of 4X gel solution (containing 297 µl of monomer solution, 6 µl of 10% TMED, 6 µl of 10% APS, 6µl of PBS) was added to the central well of each insert. To reduce the risk of pre-polymerisation the 10% APS and 10% TEMED were added to the gel solution immediately prior to dispensing into the wells, maximising monomer infiltration inside the cells. The microplate was covered with a 6-well plate lid, covered in foil to reduce access of light to the samples, after which the microplate was incubated at 37°C for 2 hrs.

2.4.3. X4 Gel Digestion and Expansion

Tweezers or similar implements were used to remove the silicone frame inserts for the well, with caution being used in the rare instance wherein gels may adhere to the frames. Digestion was performed by adding 1 ml of digestion buffer (containing 50 mM Tris (Thermo Fisher, 1 mM EDTA (Sigma), 0.5% Triton + 0.8 M guanidine HCl (Sigma),

made up to 100 ml with dH_2O) along with 1% proteinase K (w/v; Sigma-Aldrich) per well incubated at room temperature, on a rocker overnight. Digestion duration was at least 12 hours to minimise gel damage known to occur from shorter digestion periods. Samples were then washed in an excess of dH_2O to allow expansion, ensuring to fully immerse the gel. dH_2O was replaced at minimum 3 times with 1-hour intervals until gels stabilised at ~4-fold expansion. In the case of the microplates, this also included gels expanding and reaching the edges of the well.

2.5. Image Acquisition & Airyscan Processing

2.5.1. Imaging

Images were obtained on both Zeiss LSM880 AiryScan and Zeiss LSM980 Airyscan 2 (Carl Zeiss, Jena), using 10x 0.3 NA air Plan Apochromat objective, 40x 1.3 NA oil-immersion Plan Apochromat objective, 40x 1.2 NA water-immersion Plan Apochromat objective and 63x 1.5 NA oil-immersion Plan Apochromat objective (from Carl Zeiss, Jena). Airyscan mode was used throughout with accommodations to fluorescence reduction, caused by expansion, being adjusted by laser power and gain. Due to the prominence of photobleaching and the increase in spatial separation of fluorophores in post-expansion samples, the laser power and gain were increased to ensure the full data frame could be acquired within the scan window. Fluorophores were excited using Argon 488 nm and DPSS 561 nm laser lines. The inbuilt spectral detector was used to assist in selection of emission bands (BP 495-550 and BP 570-630) and recorded with the in-built GaAsP detector. Scan rates for singular images were taken over 20-60 seconds, whilst each frame in a volume was taken over 5-10 seconds to minimise photobleaching. To ensure the expanded volume was captured in post-expansion imaging, Z-projections were taken to encompass the features perceived in

the post-expansion imaging from the pre-expansion images. The associated Zen software was used to acquire the image data which was post-hoc Airyscan processed to obtain the final image.

2.5.2. Pre-/Post-ExM Region Tracking and Image Acquisition in Cells

To track the imaged regions between pre- and post-ExM, coordinates were calculated relative to a corner of the gel. This value is then scaled by the expansion factor to provide an approximate region wherein the post-ExM region should be present. Using this technique with 10x magnification images of the regions, providing macroscale structure of the local area, allowed honing into the location of the imaged cells post-expansion.

Images were obtained on Zeiss LSM880 AiryScan using 10x 0.3 NA air Plan Apochromat objective, 40x 1.3 NA oil-immersion Plan Apochromat objective, 40x 1.2 NA water-immersion Plan Apochromat objective. Airyscan mode was used throughout with accommodations to fluorescence reduction, caused by expansion, being adjusted by laser power and gain. Fluorophores were excited using Argon 488 nm and DPSS 561 nm laser lines. The inbuilt spectral detector was used to assist in selection of emission bands and recorded with the in-built gallium arsenide phosphide cathodes (GaAsP) detector. The associated Zen software was used to acquire the image data which was post-hoc Airyscan processed to obtain the final image.

2.5.3. Pre-/Post-ExM Region Tracking in Drosophila Pupal Wing Tissue

Akin to above, it is possible to hone into the location of the wing based upon its position within the gel and the relative distance to a corner. This was paired with using a non-permanent marker to mark the bottom of the coverslip and spot adjacent to the visible wing both pre- and post-digestion. To assist in reducing fluorescence loss, the wing is then located in the microscopes transmission mode before using more specific illumination for imaging. Regions were imaged at 10x magnification for a macroscopic view of the area prior to more detailed image acquisition at 40x magnification, as previously described.

2.6. Image Analysis of Expansion Microscopy Data

2.6.1. Image Analysis

Three key steps to expansion image analysis were performed: image alignment of pre-post expansion data via ImageJ, distortion mapping using Python code inspired by (Truckenbrodt et al., 2019), and Root-Mean-Square error (RMSE) data acquisition and plotting through a custom-written Python code (available via Github: https://github.com/RajSeehra/Expansion-Microscopy-Analysis-Code). Specific protocols of the full analysis, including the distortion maps and RMS error estimation is included in the relevant chapter method sections. All image analysis steps were carried out in a 13” MacBook Pro (Apple Inc) with an Intel 1.7 GHz Dual-core processor, 16 GB of memory and 256 GB in SSD storage and a 14” MacBook Pro (Apple Inc) with an Apple M3 Max processor, 48 GB of memory and 1 TB in SSD storage.

2.6.2. Stack Alignment with SIFT:

2D pre-expansion images were aligned with their post-expansion counterparts using the “Linear Stack alignment with SIFT” plugin (Lowe, 2004) for ImageJ.

2.6.3. Calculating the Expansion Factor:

A transformation matrix can be output from the ImageJ SIFT plugin, of which the structure is composed of X, Y and translation columns. For 2D expansion factor the 2x2 matrix of X and Y data can be used to calculate the scale factor change by calculating the determinant and square rooting the value. This can be directly multiplied by any scale change applied to the pre/post images to calculate the final value (Figure 2-1).

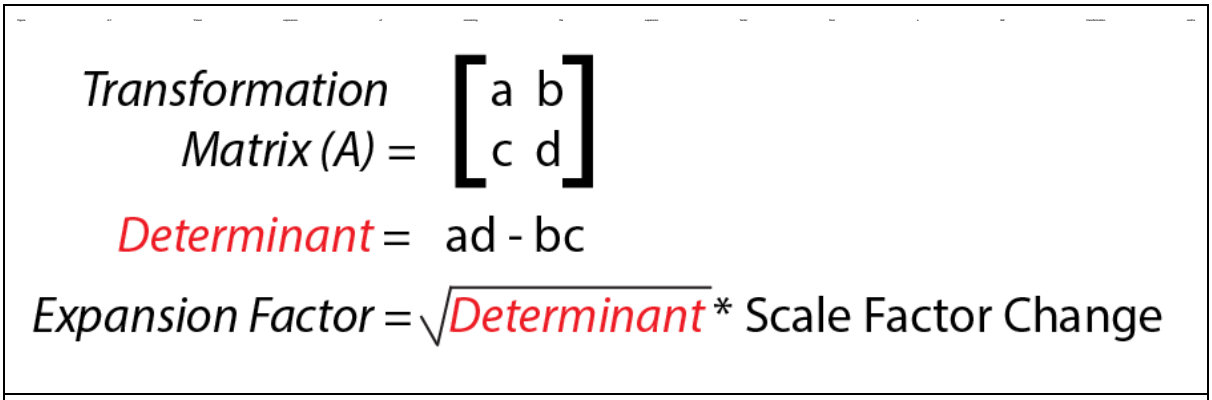

Figure 2-1: Visual expression of calculating the expansion factor from a 2x2 transformation matrix

2.6.4. Calculating the 3D Expansion Factor:

Transformation matrices are composed of axis and translation columns. The scale factor change was firstly calculated from the matrix. As a rigid approach is being used, the base assumption of isotropic expansion indicates the scale factor change should be the same in each axis.

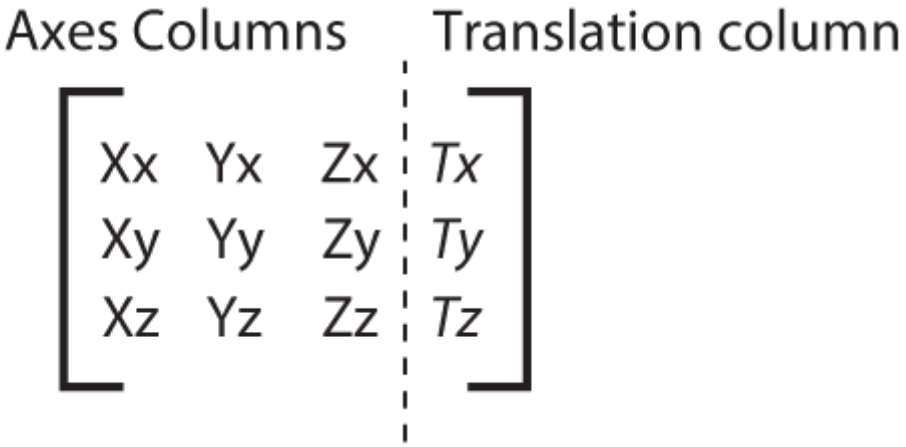

The translation columns were removed from the matrix resulting in a square matrix containing the transformation data from the axis. The determinant of the matrix was calculated and the value inversed. The resultant value was then numerically rooted based on the axis number i.e. X and Y axis data for a 2D image was square rooted, whilst X, Y, Z data in a 3D image was cube rooted.

If any additional scale factor changes have been applied during the alignment process of the image data, the output scale factor change was directly multiplied by the remaining variables.

2.6.5. RMS Error Calculation and Data Plotting

The relative shift in coordinates of features between the upscaled pre-ExM and post-ExM images was determined using the aligned image set. The Gunnar Farnebäck optical flow algorithm (Farnebäck, 2003), as described by Truckenbrodt et al. (Truckenbrodt et al., 2019), was employed to assess this shift. The algorithm generates arrays that detail the magnitude of distortion, separated by axis. These

arrays are then used to create distortion maps for the region of interest, facilitating the visualization of the error.

As isotropy is assumed, the distortion values can be used to calculate the theoretical post-alignment coordinates. The resulting series of theoretical “expanded” pre-expansion coordinates, and actual post expansion coordinates are used to calculate the distance between each coordinate in the series with all other coordinates. Respective values for the coordinate pairs between the two sets are subtracted providing an error measure associated with the original and adjusted overall distance between the coordinate pair. To account for the sizable data load, the series are iteratively processed by removing the coordinate previously used as the fixed position thereby reducing the series size incrementally. To account for this, the data was binned iteratively, and standard error, square sum, and count were collected to ensure each iteration could be combined into the overall RMSE calculation.

Upon completion data was adjusted by the pixel size of the post-expansion image, to convert to a length scale. The resulting data contains the bin position, square sum, standard error and count, which are then used to calculate the RMSE for each bin position, by dividing the square sum by the count to acquire the mean and square rooting for the final RMSE value.

The bin position and RMSE value was then plotted to visualise the distortion over the length scale of the image. Additionally, by normalising the data, RMSE from comparative datasets (i.e. images from the same gel, with the same fluorophore and lens) can be averaged at corresponding bin positions.

2.6.6. 3D Volume Alignment using Fijiyama:

Data was initially drift-corrected as required using ImageJ's "Linear Stack Alignment with SIFT" (Lowe, 2004) and pre-ExM data was adjusted by multiplying the pixel size by an approximation of the expansion factor. This was performed to assist in the initial alignment process.

Both datasets were opened with the Fijiyama (Fernandez and Moisy, 2021) plugin in ImageJ, "Two images registration (training mode)" approach. Initial alignments were conducted manually, using the similarity and 2D viewer settings. Wherein, landmarks were selected and matched between pre- and post-ExM image volumes. Image data was primarily aligned based on structures closest to the coverslip to reduce bias towards optically induced effects that may occur higher into the dataset.

Upon completion the automatic block-matching registration (Ourselin et al., 2000) approach with similarity setting was performed. The block-matching algorithm matches subregions between the image pair using the criterion defined, in this case similarity. After which, the information is collated to calculate the global transformation that best explains the local matches. The automatic process iterates this method adjusting the alignment of the images at each complete iteration to allow the algorithm to hone into the correct registration position. This approach works best when image pairs are aligned to within 15 degrees of one another as scales above this value are less likely to find alignment. Data was subsequently saved and output to the processing folder.

2.7. Designs, 3D printing & Laser Cutting

Modelling was performed in AutoCAD and Fusion 360, depending on the dimensionality of the structure. Creality Slicer 4.8.2 and Snapmaker Luban on Ender 5 Pro and Snapmaker 2.0 3D printer were used to construct our prototypes, with slicer parameters varying based on structure detail and purpose. Primary printing materials included polylactic acid (PLA) and acrylonitrile butadiene styrene (ABS). Early prototypes and the frame inserts for non-PLA/ABS materials were laser cut by Razorlab and Laserweb, wherein acrylic and black silicone rubber were used respectively.

2.8. Prototype Plate and Slide Design and Production:

The laser-cut slides outlined in this section were designed by Izzy Jayasinghe.
The SLA printing and design of the plates outlined in this section were done by Izzy Jayasinghe.

All designs were made to allow for ~4x expansion as per the pro-ExM protocol, hence expansion chambers were built at 4x the size of the gelation chambers.

Plates and slides were designed in both Autodesk Autocad and Fusion360 softwares. The former being used for early prototyping and the latter for 3D modelling the plates. Slides were produced by Razorlab by laser CNC 3mm clear acrylic.

Plate designs were prepared for 3D printing using the Chitubox Basic V1.9.0 slicing software and subsequently printed on an Elegoo Sturn 2 SLA 3D printer. The manufacturing was performed at 100% infill, 50 µm layer thickness, 5 bottom layers,

3.0 s standard exposure times and 20 s bottom layer exposure time. Translucent, low-odour photopolymer resin from Elegoo was used in the creation of the plates.

As the plates were designed to share a profile similar to the standard 6-well plate, fused deposition modelling (FDM) 3D printing was used to generate opaque lids for the plates to minimise light exposure. Designs were produced in Fusion360, subsequently sliced in Cura v5.0 (Ultimaker) and printed with the Snapmaker 2.0 3D printer. The print was produced with standard black acrylonitrile butadiene styrene filament (ABS; Protopasta Ltd) at 0.24 mm layer height, 18% infill density, 2 mm wall thickness, printing temperature of 245°C and bed temperature of 80°C.

2.9. Silicone Frame Design and Production

Frames were designed in Autodesk Autocad using the 20mmx20mm well space as a maximum frame size. The 2D designs were subsequently laser cut by Laser Web Ltd from 3mm black silicone rubber. The rubber was selected for its temperature, oxidation and UV light resistance. Upon arrival all frames were hand washed with soap and hot water to remove residue from the laser cutting process.

2.10. Chemicals, antibodies and reagent

2.10.1. Table of antibodies

Esters	**Catalogue No.**	**Supplier**	**Dilution of stock**	**Stock Concentration**
NHS AZ488	1013-1	Fluoroprobes	1:1000 (reconstituted)	1mg anhydrous
NHS Alexa488	a20000	Thermofisher Scientific	1:1000 (reconstituted)	1mg anhydrous
Primary Antibodies				
Anti-KDEL (Rabbit)	PA1-013	Thermofisher Scientific	1:500	1mg/mL
Anti-Nup98 (Mouse)	sc-74578	Santa Cruz	1:200	0.2mg/mL
Secondary Antibodies				
Alexa Fluor 594 goat anti-rabbit	A11012	Thermofisher Scientific	1: 200	2mg/mL
Alexa Fluor 594 goat anti-mouse	A11005	Thermofisher Scientific	1:200	2mg/mL

Table 2-2: Antibodies and fluorescent dye ester probes used for sample labelling.

Chapter 3. Establishing the Fundamentals of Plate ExM

Sections of this chapter are based on work published in (Seehra et al., 2023).

3.1. Background & Aims:

The traditional method of performing expansion microscopy involves many stages involving manual handling of the sample and subsequent hydrogel (Asano et al., 2018). This approach has been adjusted based on the specific sample type, gel recipe and digestion process required. However, the fundamental stages remain the same (Figure 3-1).

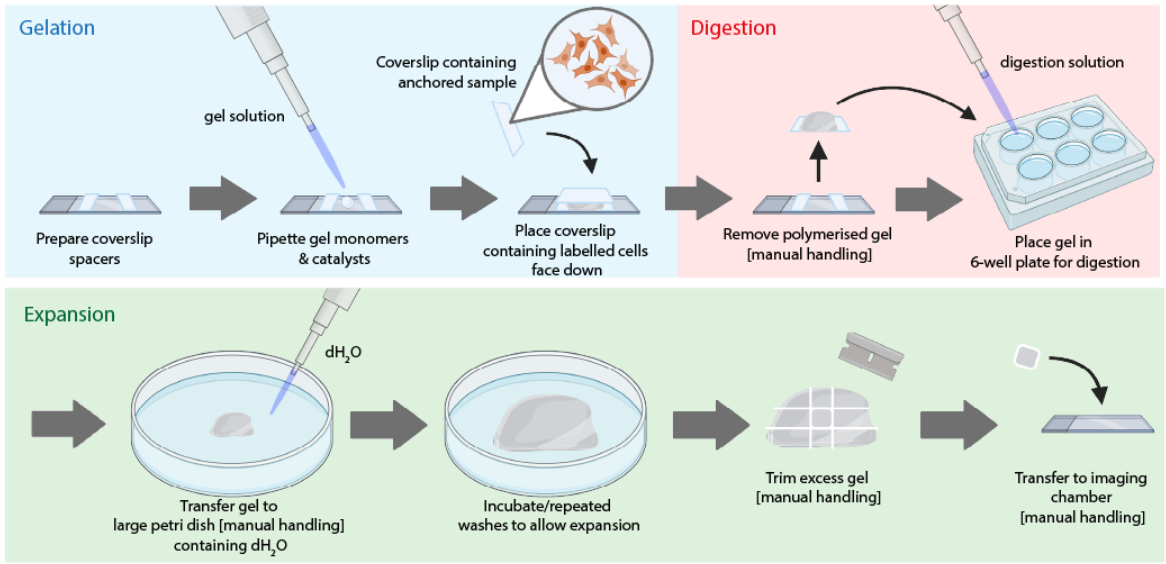

Figure 3-1: Traditional approach to expansion microscopy, adapted from (Seehra et al., 2023)

Panels show key stages of expansion microscopy including: gelation, digestion, and expansion, with main handling stages as the gel is moved.

The hydrogel casting is performed between a slide and the sample coverslip using spacers to create an opening for the gel to polymerise in. This gel is subsequently transferred to a different medium to perform digestion, and then transferred again to a larger dish to expand the sample. The nature of this process introduces a variety of opportunities to lose, damage or otherwise introduce distortions to the hydrogel.
Attempts to address this often work to maximise gel formation and polymerisation, such as, clamping the sample coverslip to the slide to prevent slippage, or wrapping the slide in parafilm to reduce the risk of the hydrogel adhering to the slide. The lab involved in the creation of expansion microscopy have demonstrated the use of paintbrushes to manoeuvre the gel whilst minimising harm (*proExM for tissues: gelation demonstration*, 2017).

Altogether, this demonstrates the requirement for consistent skill when performing expansion microscopy to obtain reliable results. Depending on the type of expansion performed unique methods and idiosyncrasies arise to assist in optimising the process. Hence, preferences from paintbrushes to flexible spatula, are commonplace amongst users to assist the gel handling processes.

Chen et al. (2015) established the analysis approach to expansion microscopy in that of pre-/post-expansion imaging of the same region and root-mean-square error analysis as a function of length measurement. By combining this with distortion mapping we can get an understanding of the accuracy and isotropy of our expanded sample.

This adds an additional layer of complexity to the expansion process as acquiring pre-/post-expansion images of the same region can be challenging. When we factor in the traditional approach and its resultant expanded hydrogel which requires imaging in several pieces, it becomes clear that finding the same region has additional hurdles. Addressing this is a particularly technical task as determining the location of the region macroscopically on the coverslip and then again in the gel can prove difficult.

The analysis is important to understand the error of structure seen in the expanded image and thus the accuracy of the data presented. This hurdle is a key reason why expansion microscopy is primarily a qualitative technique. Quantitative approaches include the measured estimates of expansion factor variance, anisotropy and local distortions which can mar the perceived reliability and reproducibility of the technique.

If pre-/post-expansion data has been acquired, then rigid or non-rigid registration methods can be performed and distortion vectors extracted. However, due to the difficulty in obtaining this information, averaging of the structure of inquiry has become a popular method (Amodeo et al., 2021; Büttner et al., 2020; Kunz et al., 2019).

It is important to find a way to standardize the analysis approach in expansion to allow data to be put into context amongst the community. This can be addressed by providing a simpler expansion framework for data acquisition. In conjunction with using the 4x pro-ExM approach as a standard we can construct a baseline for this process.

Therefore, this chapter aims to present the production and design of a simplified, more accessible approach to expansion microscopy as well as the development and

validation of an analysis pathway to produce the required RMSE data as a function of length measurement. The code developed through this chapter aims to address several of these concerns as well as reduce the burden of accessibility. Thereby, in combination with a simplified practical protocol, provide users with a clearer pathway to analysis and understanding their expansion data.

3.2. Exploration of Plate Development

3.2.1. Prototype 1: an Acrylic Slide-Based Approach to Expansion Microscopy

The laser-cut slides outlined in this section were designed by Izzy Jayasinghe.

Initial concepts in the lab were focused on a slide mechanism wherein gels were cast in a small chamber and subsequently allowed to expand into an associated larger reservoir (Figure 3-2). This prototype consisted of a slide and wedge, with the slide interlocking with the wedge to seal off the larger reservoir allowing all method steps prior to digestion to occur in the smaller sealed region.

Our initial models used acrylic slides with a coverslip attached to the bottom of the main imaging slide with silicone polymer (Figure 3-2). To test the efficacy of this technique, the slides were attached together to produce the smaller sealed chamber and water was added. It quickly became clear this approach would prove difficult due to the immediate capillary diffusion of the water in the contact areas between the wedge and attached coverslip (Figure 3-2.b.ii).

The additional issue of the difficulties in culturing cells in such a small volume resulted in the subsequent adjustments to the prototype.

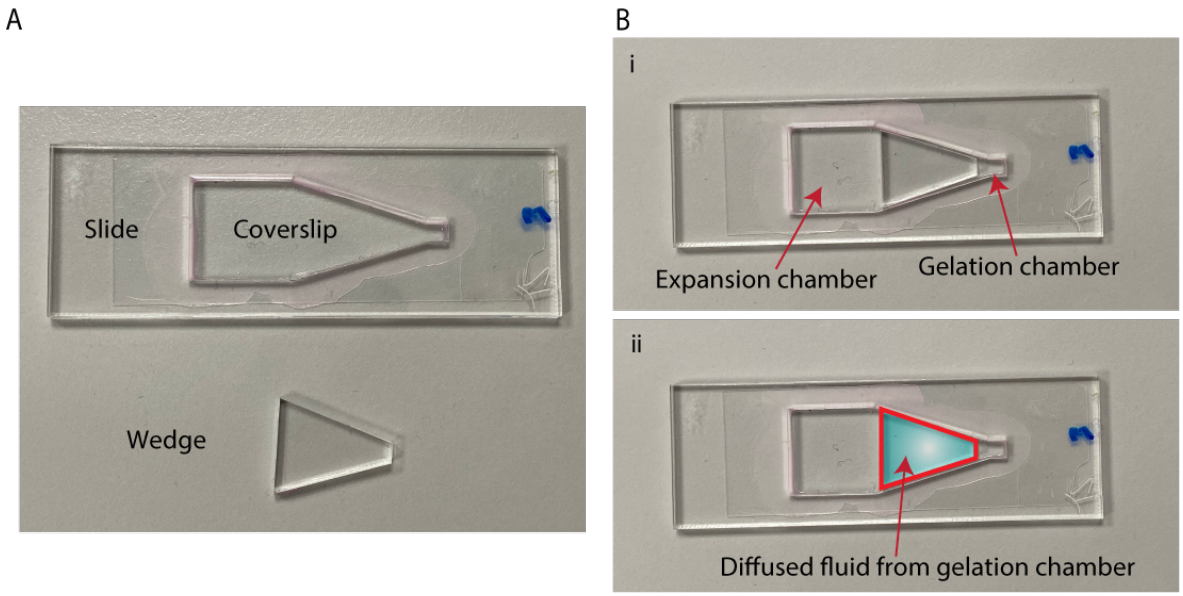

Figure 3-2: Prototype 1 components and example of usage

A) Acrylic slide with coverslip attached with silicone polymer, with an acrylic wedge used to isolate the gelation chamber. **B) i.** Prototype 1 in practice, the wedge is placed creating the gelation chamber. Once removed gels can expand into the expansion chamber. **ii.** Illustration of the region where capillary diffusion of fluids occurs.

3.2.2. Prototype 2: Acrylic Sheet with Bottle Formation.

The previous issues of capillary diffusion and difficulties in cell culture were the main areas addressed in this approach. The capillary diffusion seemed to be aggravated by the reduced contact between the surfaces due to excess polymer near the attachment point between coverslip and acrylic slide. This prevented the surfaces from lying flat against each other.

To address this an acrylic sheet with a larger 5x5mm profile attached to a larger region to produce a bottle-like design. The previous second slide was adjusted to a second sheet with trapezoidal acrylic units protruding, which acted akin to the previous wedge. This unit would be placed below the neck of the bottle to seal the 5x5mm region for the relevant pre-digestion stages and the two sheets could slide against each other to release the mechanism. Similar to before, once cast, the gel would be freely released into the larger volume to expand (Figure 3-3).

This resulted in reduced capillary action when tested with water, with water being wicked under the blocking unit but not past it into the larger well. With the main focus at this point being to limit the contents of the smaller region to that singular area this was a key part that needed to be addressed or designed around.

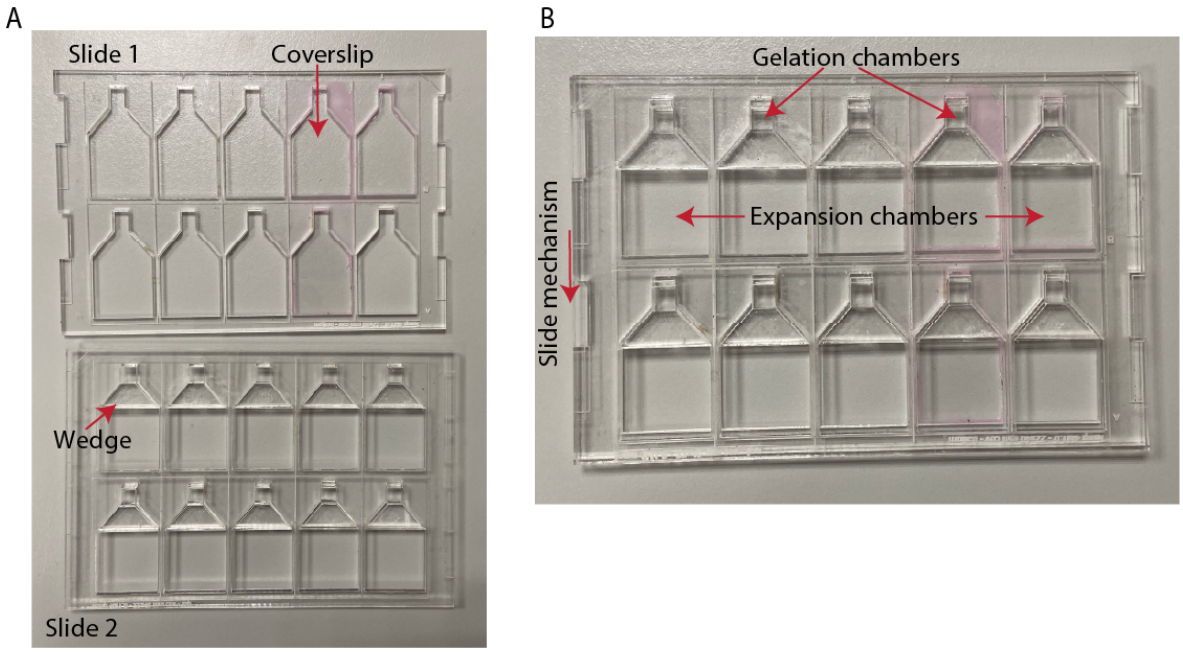

Figure 3-3: Acrylic sheets with sliding mechanism to cast and expand gels
A) Two acrylic sheets designed to fit together. Slide 1 contains the chamber layout and coverslips. Slide 2 has affixed wedge structures placed to seat into slide 1. **B)** When combined slide 1 and slide 2 form a 5x5mm gelation chamber. Slide 2 can be moved to transfer gels from the gelation chamber into the expansion chamber.

3.2.3. Prototype 3: Silicone Frames as a Substitute

It became clearer that the 5x5mm region would also be difficult to grow cells within and this could add a layer of difficulty to the process of expansion microscopy. To attempt to reduce the capillary action we decided to use silicone rubber as a material due to its hydrophobic nature. Hence to address these points, the prototype was redesigned with a simpler approach in mind.

Previous designs required all steps from cell culture to gelation to be carried out in the 5x5mm region with the cast gel being digested and expanded in the larger previously

unused region. This prototype allowed for all steps to be carried out in a 20x20mm well with our newly developed silicone frames being used to cast the gel (Figure 3-4).

These frames were produced slightly smaller than the well and in 2 parts allowing ease of assembly and dismantling as hydrogels would often stick to the previous acrylic material. They contained a central opening of 5x5mm wherein the gel is cast.

An acrylic sheet containing 15 cut sections in a 3x5 orientation was produced with each square section at 20mm x 20mm. Coverslips of a slightly larger size were affixed to each section with silicon polymer to produce a well at each position (Figure 3-4.B).

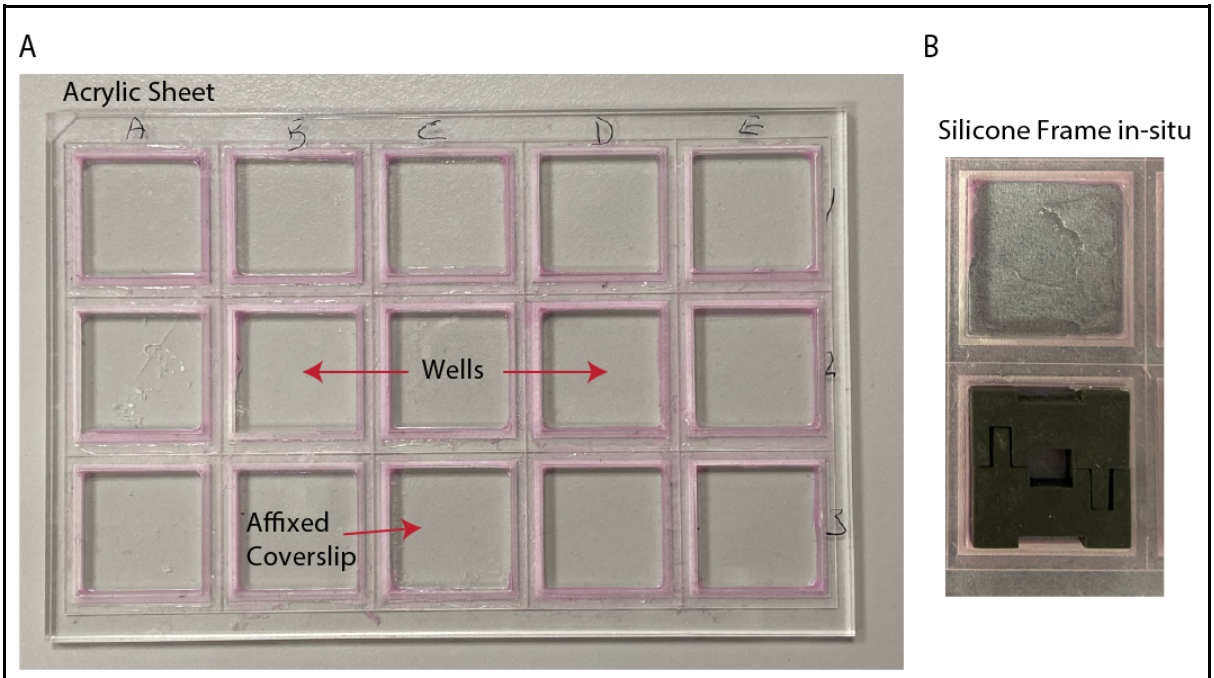

Figure 3-4: Prototype 3 made from 3mm acrylic with glass coverslips affixed with silicone polymer

A) Breakdown of prototype 3, an acrylic sheet with 15 cut regions each of size 20x20mm. Coverslips of size 22x22mm are affixed to each region with silicone polymer to create wells. **B)** Example of silicone frames in-situ. The frame is made of black rubber silicone and cut into 2 pieces that interlock to create a smaller chamber for gelation.

Initial testing was performed by placing the frames into dry wells and adding 4x gel solution to the central opening. Four test conditions were established: acrylic frames, acrylic frames pre-stuck to the coverslip with silicon polymer, silicone rubber frames, and silicone rubber frames pre-attached to the coverslip with silicone polymer.

As expected, the acrylic frames were subject to significant capillary action and resulted in two outcomes: gels being cast in the wicked areas, and no gel being cast (Figure 3-5). The acrylic frame pre-attached with silicone polymer was able to cast the gel,

however upon removal of the frame the silicone polymer was difficult to remove from the cast gel without notable disturbance as it had bonded to the gel. This would limit the expansion process. Finally, the silicone rubber frame-based approaches were able to cast gels in the required region in all cases. The issue with freeing the gel persisted in the silicone frames that were pre-attached to the coverslip and highlighted the gel casting ergonomics of using only the silicone frame. All cast gels were subsequently expanded for completeness and reached ~3-4x expansion.

The height of the expanded gels exceeded that of the wells we had produced and was a target to address in future designs, alongside the limited well volume from the shallow wells.

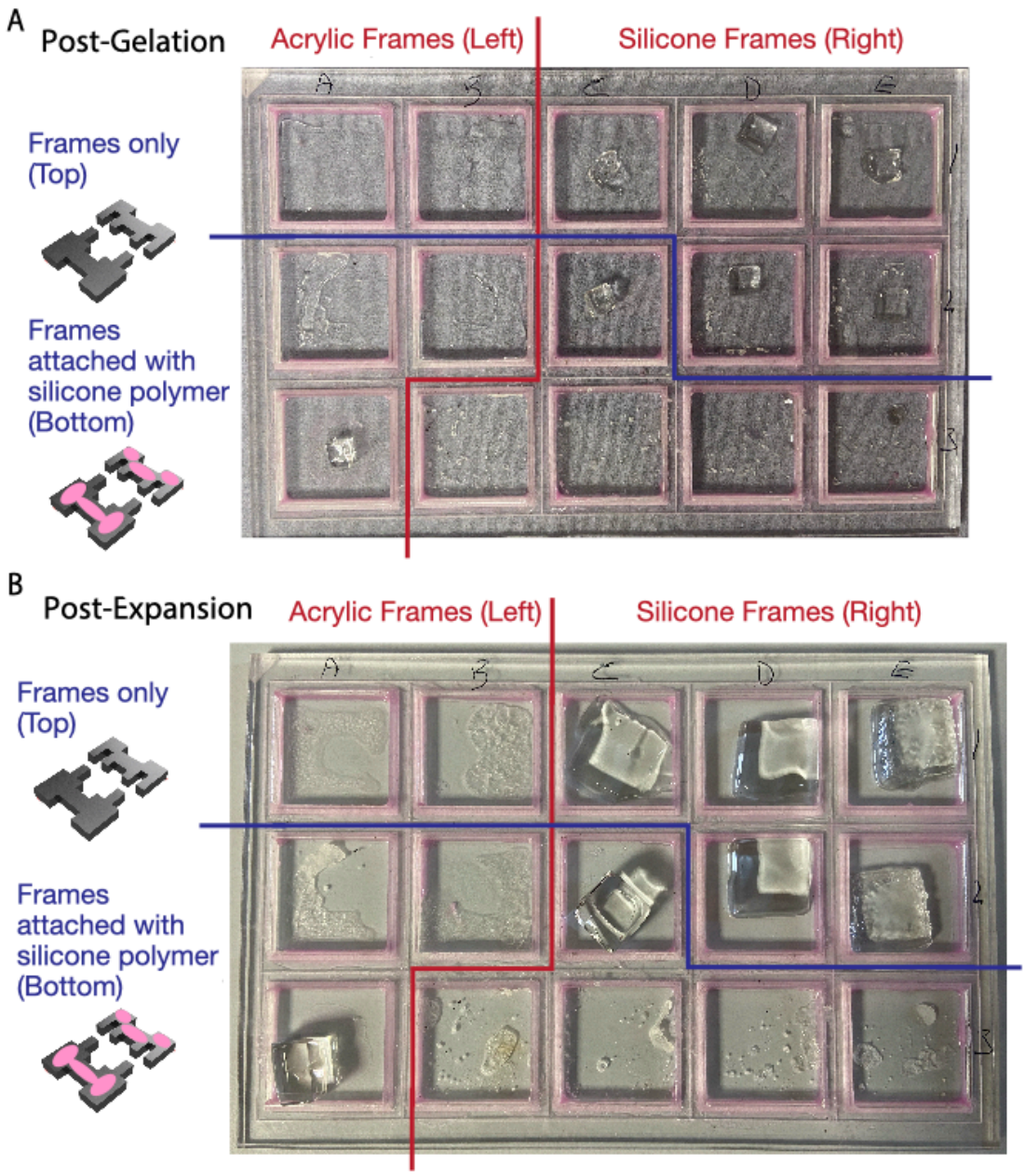

Figure 3-5: Gel casting experiment with frame designs in prototype 3

Comparison between acrylic frames and silicone frames (red line) separated by frames affixed with silicone polymer and those without (blue line). The silicone frames without the silicone polymer were significantly more successful compared to the other conditions. **A)** Post-gelation image of gel cast in frames, showing 7 successfully cast gels, 5 with silicone frames only, 1 with silicone frame and silicone polymer, and one with acrylic frame and silicone polymer. **B)** Post-expansion image showing expansion of successful gel by ~3-4x.

3.2.4. Version 1: Plate-Based Design

Combining the core components of a square 20x20mm well, silicone frames and multi well capacity from the previous prototypes a plate-based design was produced. This plate shared the footprint of a 6-well plate to maximise compatibility, now containing 8 of our square wells. This design was chosen to allow the microplates to be used with devices compatible with a 6-well plate. For example, microscope stage holders and plate readers. Additionally, each microplate well aligns with the well positions of a 96 well plate. The plate was resin printed, to allow for rapid prototyping with a chemically resistant structure and had appropriate depth to conduct ExM experiments within (Figure 3-6). Resin printing has the additional advantage of full 3D construction of elements allowing for detailed additions to be made over the previous laser cut acrylic.

Previous testing had shown that silicone polymer-based attachment of coverslips was not particularly effective and it was possible to detach them with little force. Hence, we moved to using epoxy resin to bind the coverslips to the plate.

Initially, this proved highly effective and the plates were able to grow cells within them suitable for expansion microscopy. Full testing of expansion microscopy within the plates showed functionality at each step (further expanded on in the next chapter). However, two issues became immediately apparent: leakage of solution from the plates, and frequent capillary issues when using the silicone frames to produce gels.

The leakage was isolated down to a difference in thermal expansion between the resin plates, the coverslip and the epoxy that bound them resulting in imperceivable gaps wherein fluid would slowly leak from.

The newly occurring capillary action with the frames was associated with the epoxy resin. This was due to excess epoxy resin on the inside of the well lifting the silicone frames at the corners, creating an area for the gel solution to leak into.

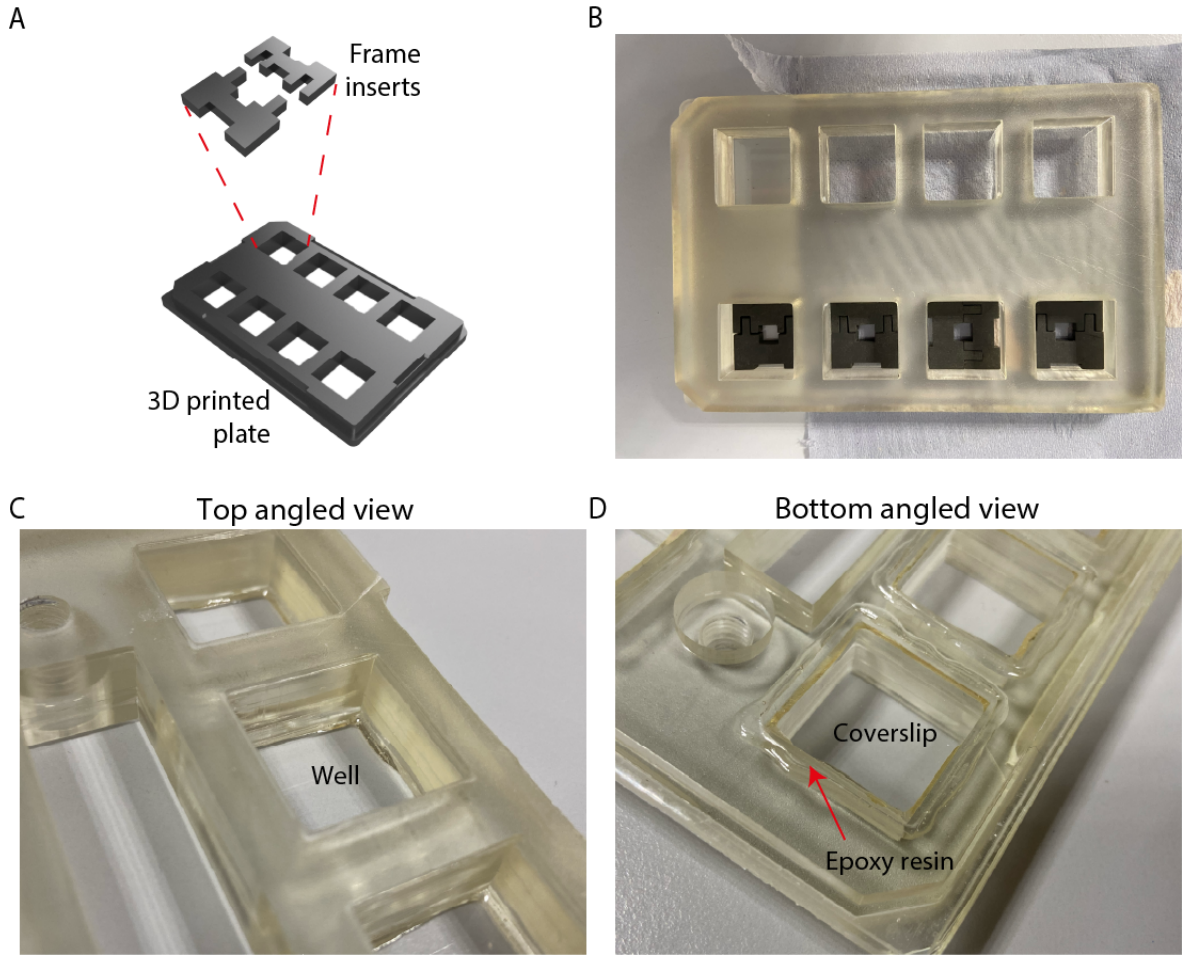

Figure 3-6: Plate based design for expansion microscopy

A) Schematic model designed in Fusion 360 illustrating the plate and silicone insert. **B)** Top view of the resin printed plate, with silicone frames placed into the wells. **C)** Angled top view close-up of a well to illustrate the structure. **D)** Angled bottom view close-up illustrating the attachment of the coverslip to the plate with epoxy resin.

3.2.5. Version 2: Adjustments to Design to Facilitate Usage

With the epoxy being a prominent issue, we reverted to using silicone polymers to attach the coverslips. Investigations into a stronger silicone polymer, capable of holding the coverslip to the well without detaching when probed with a pipette, were done and upon testing this proved effective at holding the coverslip to the well.

To facilitate the attachment, maximise bonding region and reduce the excess polymer that entered the well area, the attaching surface on the bottom of the plate was adjusted to have a groove structure.

Slightly smaller frames were also produced to allow for better seating in the well minimising any lifting that could occur.

This resulted in a marked increase in the success rate of successful gel polymerisation in ExM experiments performed in the plates from a previous ~50% to an 80-90% (Figure 3-7).

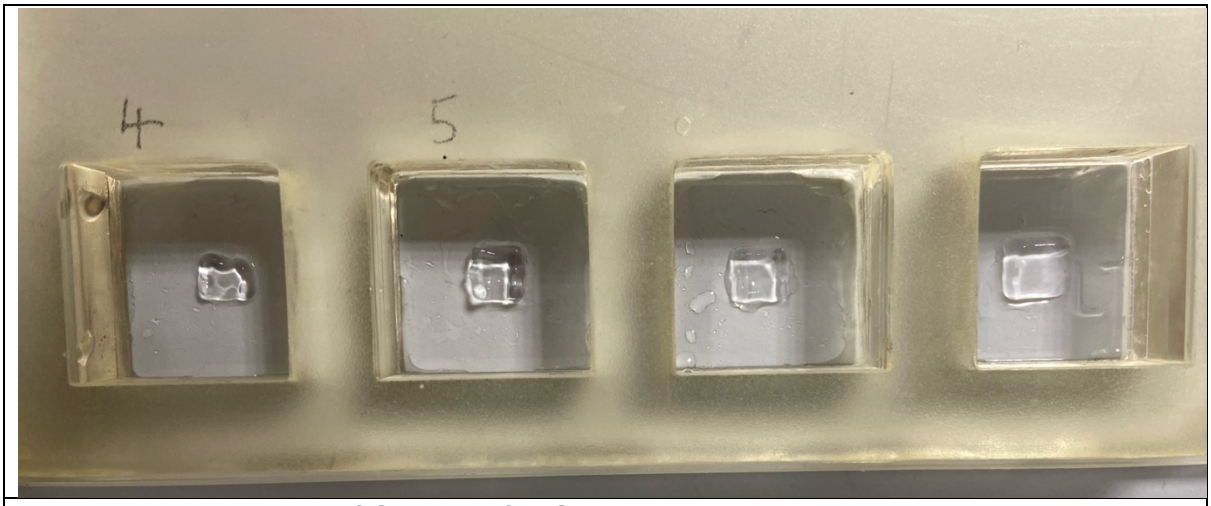

Figure 3-7: Example of Successful Gel Polymerisation in Plate
Example of 4x expansion gels being successfully formed in four successive well in a single plate. Images were taken post-frame removal to better illustrate the presence of the gels.

3.2.6. Exploring Other Designs

To increase accessibility to the design, ABS-based plates were produced by 3D-printing. The ABS-based plates had coverslips attached using silicone polymer.

Initial testing to test leaking by adding water to the wells were successful. However, problems arose when attempting to culture cells in the plate. Media leakage would occur, resulting in the cells dehydrating. Isolating the leak proved ineffective and is thought to be due to the presence of micropores in the 3D printing of the plates.

On detaching the coverslips and drying the plates on a tissue, a purple solution was found on the tissue the subsequent morning. This incident provided the necessary clue for the cause of the leakage. When 3D printing with a filament deposit printer, the internal structure of the model can be filled with a pattern to promote stability whilst minimising filament usage, resulting in a standard 20% infill. The micro-apertures

between the layers as a result of filament printing provided capillary action for fluid which accumulated in the infill cavities. This was determined to be a fatal problem to the design, requiring a non-toxic plastic sealant to allow practical usage.

3.3. Development of Python Source Code for Expansion Microscopy Data Analysis

Expansion microscopy analysis code is split into two categories, distortion mapping and RMS error as a function of length measurement. Taking inspiration from Truckenbrodt et al. 2018 (Truckenbrodt et al., 2018), Färneback optical flow (Farnebäck, 2003) was used to generate the distortion vectors between the pre- and post-expansion aligned imageset. Färneback optical flow applies a 2D gaussian structure to subsets of the image pairs and compares the resulting matching sub-image regions. This allows for a quadratic calculation on the resulting spatial difference between the image subsets and thus acquire the vectors we use herein. Optical flow distortions are dependent on a reference point shared between the images; this is artificially selected for by the alignment process. This optical flow method was used under the following assumptions:

- Isotropic expansion
- Global structural similarities
- Depth of field variance is accountable.

These assumptions are based on an optimal pair of pre- and post-expansion images, wherein, the sample has expanded isotropically, all structures in the pre- expansion image are present in the post-expansion, and images have comparable depths of field to contain said structures and information for comparison.

The distortion code outputs 2D arrays containing distortion values for X and Y independently (Figure 3-8). The magnitude of these values in each direction can be used to calculate the angle of the distortion at each pixel in the image.

By using this distortion data, the RMSE can be calculated. Classically, RMSE can be used to compare two images. However, this provides a one-dimensional assessment of the similarity between the images as a function of the pixel intensity. Additionally, to this process helps account for the bias introduced by the alignment algorithm and optical flow process by comparing local distortions. This effectively corrects for the optical flow global bias by comparing at matched point pairs between the data.

In ExM, RMSE is calculated with its relation to length measurements across the image. Specifically, calculating the difference between: A-> the distance between a pair of points in one image, B-> the distance between the same pair of points (distorted) in the other image. The difference between B and A is the absolute error which is paired with the original distance between the points to provide the absolute error at a known length scale. By calculating these values across an image, the data was collated and binned. Within each bin, the absolute error values were root-mean-squared to provide the RMSE at that length measurement.

This approach allows for a two-dimensional assessment of the similarities by comparing the difference in the structures present over the length scale of the image and thus an estimation of the difference and hence error between them.

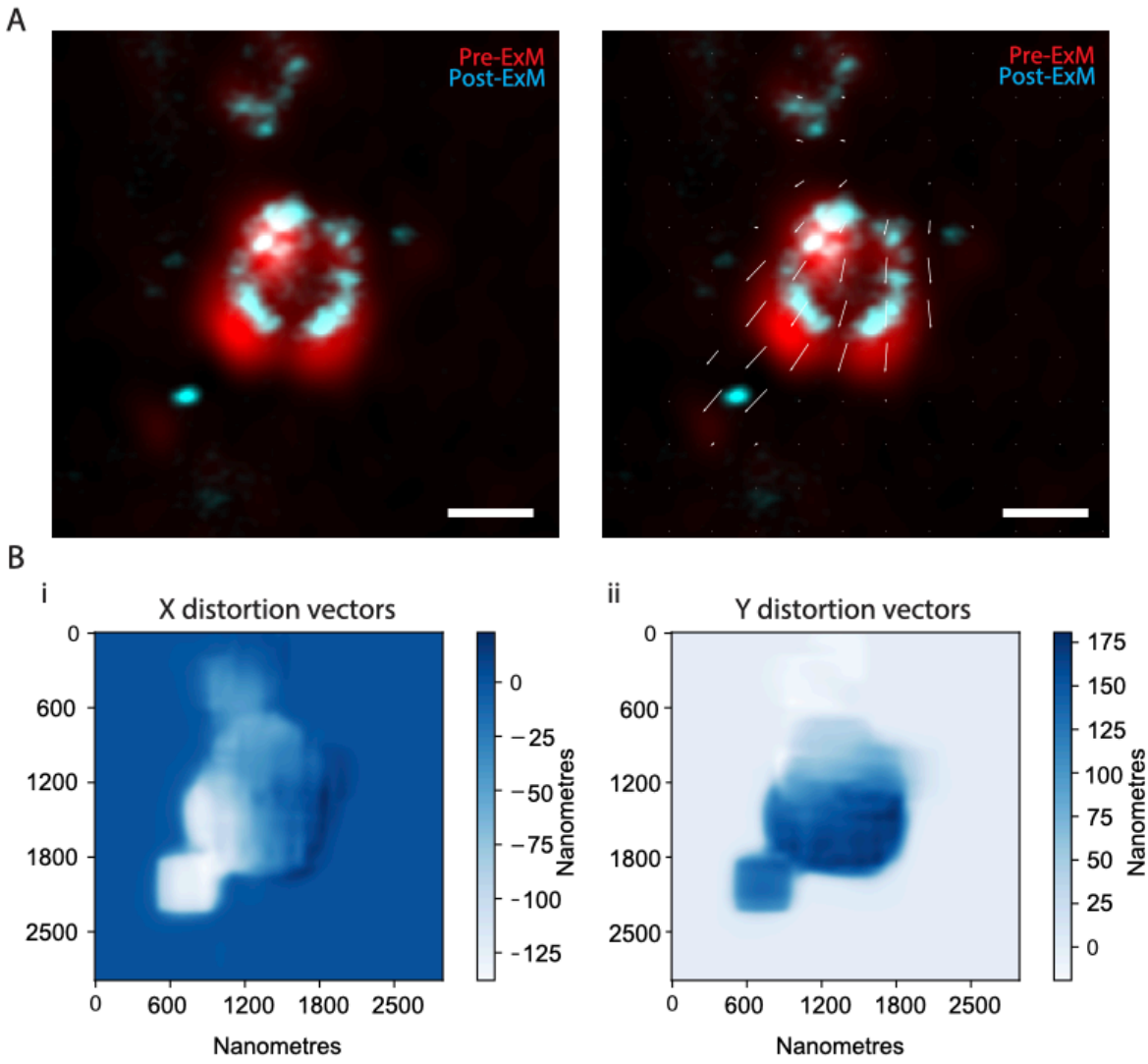

Figure 3-8: Image data representing the overlaid pre/post-ExM images and the distortion vector information

A) Pre- (reds) and post-ExM (blues) data, with second image with distortion vector overlay. **B) i.** X distortion vectors indicating a predominant leftward vector preference. **ii.** Y distortion vectors indicating a predominant downward vector preference. **Scale Bar:** 500nm (pre-expansion scaled)

In regard to coding this process, the task was divided into 4 sections (Figure 3-9):

1. Distortion vector acquisition
2. Bright point selection and vector extraction
3. Distance and difference calculation between pairs of points
4. Binning and RMSE calculation.

Classically, all points from the images are used for RMSE calculations, however, for larger datasets this impedes the speed of the process and includes large regions of background data in the analysis. To counteract this, selection criteria was established to include points likely associated with structure of interest. This was done by masking the fixed post-expansion image to include the brightest points. After which a skeletonisation can be applied to further focus the mask to the centre of the structures highlighted by the previous step. To verify the structural selection of this process, array outputs at each stage were generated and compared. These showed striking similarities to the original image with the expected reduction in points (Figure 3-10). The skeletonisation exhibited an interesting effect on denser regions wherein these areas were evenly divided such that the skeletal regions were encompassing the overall structure of the region.

In Figure 3-8 the change in detail is apparent as the threshold changes. Therefore, it is important to determine an effective number of points when using this process. Too few could negatively bias the distortion data whilst too many would overly increase the processing time. As such, initial thresholding tests should be performed to ensure all relevant data is included. This could vary vastly depending on the size and density of the structures of interest.

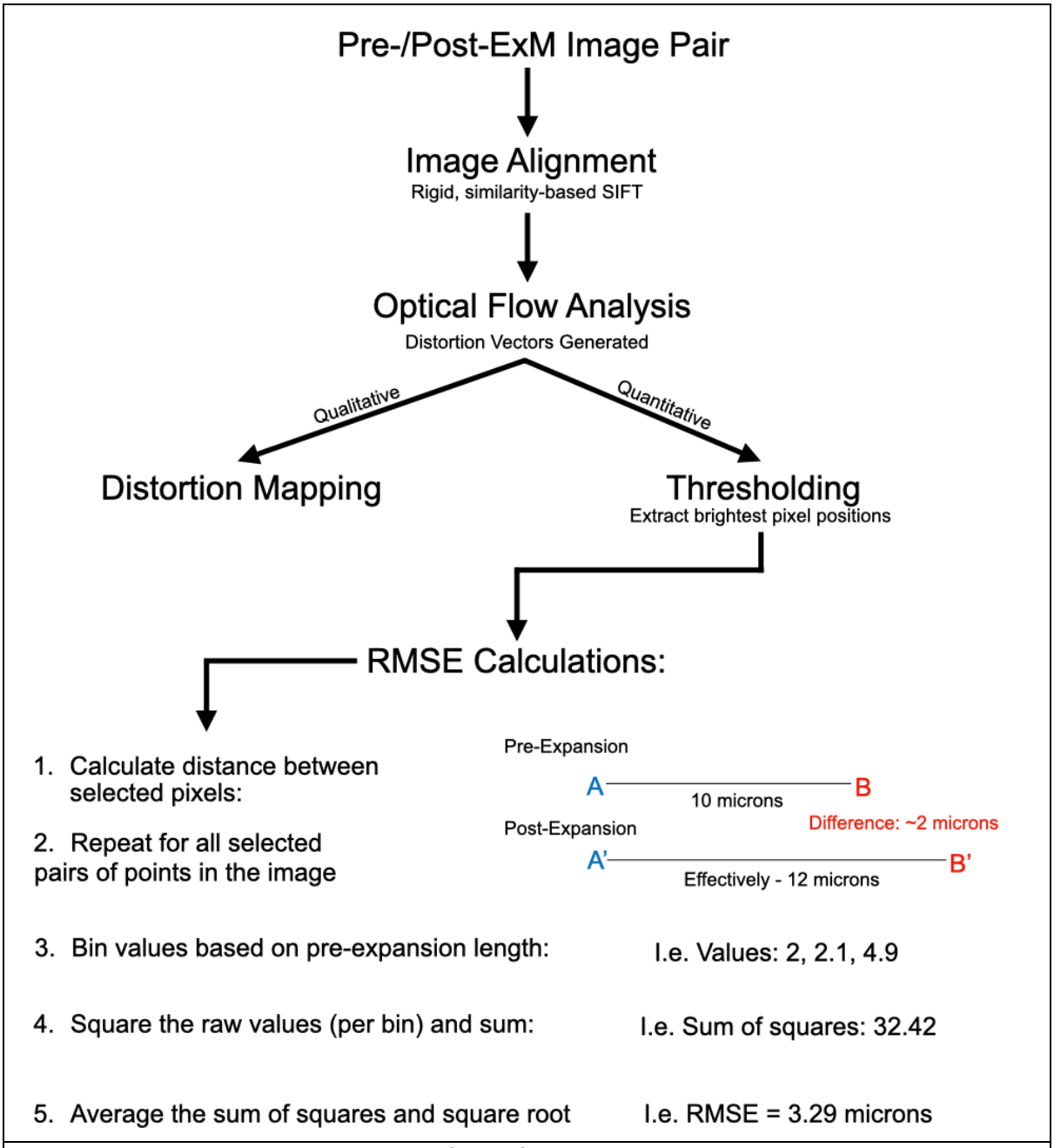

Figure 3-9: Analysis Flowchart of Pre-/Post-Expansion Image Data

Image analysis follows a basic protocol based on qualitative or quantitative outputs. Data is initially aligned using rigid, similarity-based SIFT. Subsequently, optical flow is used to generate distortion vectors which can be used to create a distortion map or proceed toward RMSE calculations. Thresholding the data to yield high structurally significant pixels allows for the distance between selected pixels to be measured. The difference between pre-/post-ExM images yields the distance error. These values are collated and processed through root-mean-square approach to provide the RMSE for each measurement length data bin.

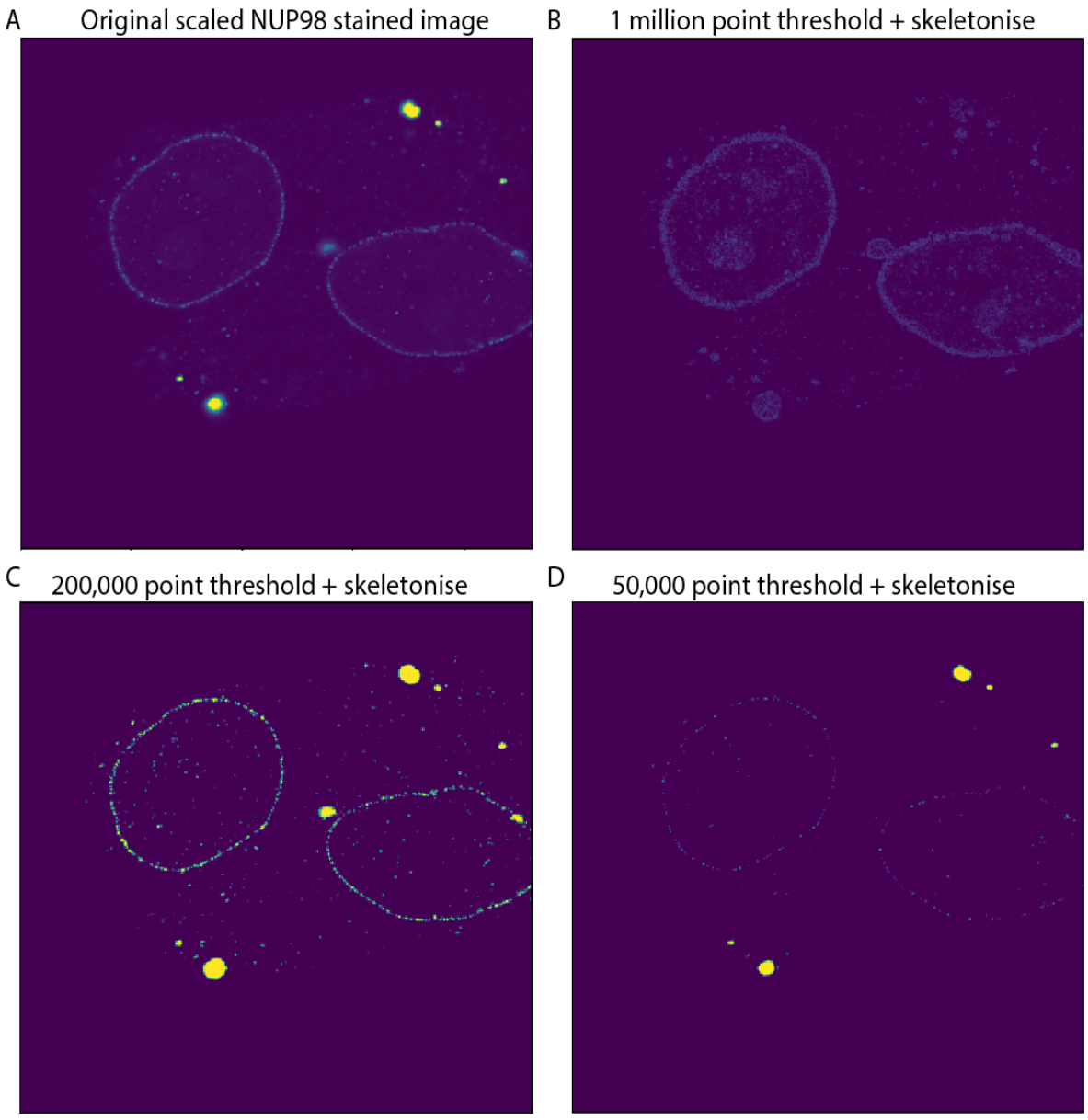

Figure 3-10: Validation of the threshold + skeletonise process, showing retention of key structural points between reducing degrees of retained bright points

HeLa cells stained with NUP98 used as image data. **A)** Original scaled image data to allow better viewing of structures. Image data was separately subjected to bright point thresholding and skeletonisation at varying numbers of bright points from: **B)** 1 million bright points, **C)** 200,000 bright points, **D)** 50,000 bright points.

The coordinates from these thresholding methods were collated to provide the list of points to be used for the RMSE calculations (Figure 3-9). The distance between every point in the list to all other points in the list was calculated using the numpy based linalg.norm at the second order to calculate the euclidean distance (Harris et al., 2020). As we only require the distance between points once per point pair, we can take the lower triangle of the array of point pair distances. In regards to the code this means that with each iteration of calculations where one point is measured against all others, we can remove that point from subsequent iterations. This reduces the overall memory usage with each subsequent iteration being faster than the previous. At each stage the distance between point pairs can be subtracted from the equivalent pair in the distorted dataset. This provides us with a measure of absolute error between the original distance and distorted distance for each pair of points.

With each iteration this data was compiled into a binning array to collate data sequentially and allow for feedback during the analysis (Figure 3-9). This also allows for larger datasets to be analysed as the number of points are reduced to prevent exceeding the memory capacity of the machine. In a practical case, for a 1000-pixel square image we have 1 million pixels of data, if we select 10,000 (1%) of these points, we are dealing with 100,000,000 pairs of points. Subtracting the duplicate and same point pairs we are left with ~50,000,000 points. Computationally, due to how the Python code handles array data, each point will occupy space in the RAM. As this value scales up for more points this can overflow into hard disk space. 50-million-point pairs is approximately equivalent to the megabyte scale. This size is significantly more manageable than the full array used by other methods which would be on the terabyte scale for space usage. By sequentially calculating the distances we can reduce this

array back to 10,000 for the initial iteration, reducing memory load and increasing the speed of the process. Thereby allowing machines with less capacity to process the data.

3.4. Discussion

3.4.1. Designing New Methods for Expansion Microscopy

The traditional approach to expansion microscopy includes several stages where care and dexterity are required to minimise losses and errors. In particular, the stages of gel handling and transference pose a risk for every experiment performed and increase the difficulty of being consistent with the technique.

By minimising the risk of these stages, it becomes possible to increase the reproducibility of the technique. By reducing the effect of manual handling the remaining factors influencing the sample and distortion production can be elucidated. For example, a tear in the sample could be caused by either manual handling or incomplete digestion. By reducing the likelihood of manual handling causing this issue, digestion steps can be more accurately optimised within the classical approach (Asano et al., 2018).

Moving forward from this approach to a more generalised technique can help to regulate the field and provide a structure to the analysis. The attempt to consolidate the expansion process to a single chamber can be considered a step in this direction. The traditional approach holds merit in its versatility and can be especially powerful in knowledgeable hands. However, now that established techniques (U-ExM (Alonso, 2022), TissU-ExM (Steib et al., 2022b), Magnify (Klimas et al., 2023)) for imaging

different sample types with expansion microscopy are being developed, it is clear that providing a way to standardize this process will increase the usability and therefore, development of this field of microscopy.

As seen by the Hi-ExM approach (Day et al., 2024), developing a plate-based system compatible with automation systems would allow large upscaling in throughput and data collection. However, is currently limited by the lack of clear standardisation of the technique and regulation in image analysis. The approach can be considered a future advancement for ExM as the technique grows and becomes more robust. Comparatively, the plate-based approach described here allows for a balance between automation and manual experimental approaches. The wells are sufficiently sized for both gel formation and researcher interaction, whilst having the footprint of a multi-well plate, allowing for compatibility with plate readers and similar equipment.

The current plate design underwent several changes from its initial slide-based inception. The current iteration, using silicone frames to cast gels, holds the advantage of allowing the entirety of the experiment to be performed within the plate. This actively reduces the manual handling and transference steps from a minimum of three stages in the traditional approach to none in the microplate approach. This allows for a more regular approach that is similar to standard 6-well plate fluorescence experiments.

This does come with several limitations in: compatible protocols, gel casting, and production material. The plate currently only allows for 4x expansion protocols. The silicone inserts are designed to cast a gel 4x smaller than the well, and it is technically possible to cut this gel to a smaller size to enable expansion protocols of greater than

4x. This would reintroduce the manual handling of gels and require a degree of dexterity by the user in question. Having personally attempted such, it became clear that gel recipes, such as x10 ExM (Truckenbrodt et al., 2018), that are more amorphous on casting are less pliable to such an approach and resist being cut till some expansion has occurred. Comparatively, TREx gels could be used here as a more robust gel recipe could provide the needed structure to allow division of the gel.

Secondly, as the wells have been exposed to prior solutions for cell culture and immunostaining, residual fluid left on the coverslip can increase the likelihood of fluid being drawn under the silicone frames. This can be significantly reduced by an additional pass to remove excess fluid from the well, in addition to ensuring the inserts are placed as flat to the coverslip as possible. Hence, it is advisable to test the fitting of silicone inserts to the well of the plate prior to an experiment to ensure the fitting.

3.4.2. Analysis Pathway and Standardisation

The initial Chen et al. (2015) (Chen et al., 2015) paper introducing expansion microscopy had established a framework to validate the technique and this lay the foundation for the gold standard of pre-/post-expansion imaging of the same region and RMSE analysis. Aspects of this approach have been utilised when others have validated their novel additions to the technique (Steib et al., 2022b; Chang et al., 2017; Damstra et al., 2022).

Iterative ExM (Chang et al., 2017) analyses its approach using pre-ExM STORM imaging with post-ExM confocal imaging of microtubules. This is displayed through comparative images, overlays and an example RMSE graph. A non-rigid approach

was used to calculate the deformation vectors. However, distortion maps are not present in the paper or its supplementary material, forcing a reliance on the overlaid pre-/post-ExM images as a means of qualitatively assessing the distortion.

TissUExM (Steib et al., 2022b), used pre-/post-ExM imaging with rigid registration methods to calculate the distortions and expansion factor. The RMSE was then calculated from these distortion vectors. This data was combined with the use of basal bodies as molecular rulers to quantify isotropy in their zebrafish and mouse embryo data. Whilst this combination of approaches was performed, the distortion analysis data is only shown for the zebrafish data in the supplementary information. Comparable data for the mouse embryo and *Drosophila* wing samples that underwent the TissUExM process would provide further insight into the efficacy of the technique.

TREx (Damstra et al., 2022) on the other hand was validated using the gold standard approach at multiple stages for each variation tested. The primary data illustrates the comparative resolution between post-ExM TREx data and pre-ExM 3D STED data with RMSE and deformation field information providing further context. Registration was performed with rigid-based methods differing from the previous approaches. Expansion factor values were corroborated with standard structure measurements providing a secondary validation to the approach.

This has led to variations in the analysis method bespoke to the samples, imaging modalities and expansion size of the technique. Broadly speaking in regards to the analysis, rigid and non-rigid registration approaches have been used to differing effects. Non-rigid approaches have been used to directly align and extract the

distortion values allowing for both computation of the distortions and attempting to correct them. Rigid approaches on the other hand, refrain from attempts to correct the distortions and focus on expanding insight into the nature of the distortions.

Both hold value in the expanding nature of this field, in particular, the baseline assumption of isotropic expansion allows us to understand that deviations from the expected model are distortions present in the data. From a rigid approach perspective, we can highlight the distortions between the pre- and post-expansion images and get a clear visual representation of the location and prominence of these distortions. Whilst from the non-rigid approach we can further delve into the actual shape of the structures present. This latter aspect can still be regarded as being in its infancy when applied to ExM in that the information is primarily used to perform distortion analysis. However, with the advent of machine learning and artificial intelligence, integrating a non-rigid model with additional structural data could allow for reconstruction of distorted post-ExM data, akin to current methods in histology research (Ke et al., 2023).

Hence, the focus for the code developed here is using rigid, uniform methods to provide us with the insights necessary for this foundational understanding of the gels cast and the structures of inquiry.

Specifically from a coding perspective, previous programs have been designed in a variety of languages with Python as the most common (Damstra et al., 2022). Focus on both image alignment and distortion vector calculations have been explored (Damstra et al., 2022), however, notation and functionality are often optimised to the creators intended purpose. This can introduce a wide variance in the understanding

of how the code is producing the data with clear difficulty of investigation without being well-versed in the field. Combined with the limitations created by larger and more complex image sets in computation time, there is a clear accessibility issue which has arisen.

The approach developed herein can allow less powerful computers to process large-scale expansion data whilst providing simple feedback on the stage of the analysis. Having split the distortion vector mapping from the RMSE calculations we can take advantage of the shorter time required to produce the distortion map as a separate program for the user to run. This results in several minutes to produce the distortion map, compared to hours of time to produce both distortion map and RMSE data when run on a standard university managed desktop machine. This better delineates the process of expansion analysis to: pre-/post-expansion image alignment, distortion mapping, and RMSE calculations and plotting.

3.5. Concluding Remarks

The development of a standardised and accessible method of ExM has highlighted the new avenues to further integrate ExM as a staple tool for researchers. By shifting from a slide-based approach with multiple stages of manual handling to a microplate approach has allowed for a reduction in these potential error causing steps. By being able to perform the entirety of ExM in a microplate the process can be streamlined, improving reproducibility and consistency.

The methods established here are primarily for a 4x ExM recipe, and further investigation could yield adaptations to allow for larger expansion recipes. Through a

combination of modifications to plate design and the use of robust gel recipes this is a clear future development for a plate-based ExM approach.

The introduction of a Python-based coding pathway for ExM data analysis with adjustments to improve data processing efficiency, whilst maintaining accuracy, maintains the ethos of democratisation that ExM is known for.

In conclusion, the plate-based approach to ExM streamlines the technique's procedure. Applications of this approach are broad and help to reduce the factors needed to optimise an expansion experiment. Therein allowing for a scalable, reliable approach to biological imaging through expansion microscopy.

Chapter 4. Validation of Microplate ExM and Distortion Analysis

Sections of this chapter are based on work published in Seehra et al., 2023.

4.1. Background and Aims:

As a technique, ExM is predominantly qualitative with distortion analysis being required to validate the robustness of quantitative measurements. Thus, the process of extracting greater detail and information from ExM has been explored in a myriad of ways to further understand the data collected. The current gold standard of expansion microscopy analysis includes: pre-/post-expansion imaging of the same cells, distortion analysis and RMS error quantification as a function of length measurement (Truckenbrodt et al., 2019). This approach does result in difficulties in discussing nanoscale distortions due to the inherent limitations in alignment algorithms, and the perceived RMSE from the data.

Together these provide a measure of how much insight can be obtained from the sample and the limitations of resolution as improved by the expansion process. Whilst isotropic expansion is often assumed, using these measures it is possible to assess the presence and scale of distortions and add a quantitative value to the accuracy of further analyses.

The inherent difficulty with collecting pre-/post-expansion data has led to alternative approaches to assessing these quantitative measurements. These include averaging of structures (Büttner et al., 2021; Chen et al., 2021; Kuang et al., 2022; Wen et al.,

2021b), macroscale expansion factor calculations (Gaudin et al., 2022; Sun et al., 2022; Truckenbrodt et al., 2019; Yao et al., 2021) and additional roundabout measures (Königshausen et al., 2021; Marongiu et al., 2020; Scardigli et al., 2021) to obtain a more generalised interpretation of the distortions present and the expansion factor of the sample.

However, with the inherent heterogeneity of each expansion sample, this adds additional layers of error that are not easily accounted for. These include incomplete expansion of denser structures and heterogeneity in the gel matrix. By minimising the introduction of inconsistencies prior to image acquisition, the robustness of expansion microscopy can be improved.

In regard to expansion analysis, qualitative distortion mapping and quantitative RMS error are the main processes. Each provides insight into the errors present, with distortion mapping being more comprehensible as a visual technique and RMS error profile providing the length-based structural confidence in the data.

Distortion mapping involves measuring distortion present between the pre-/post expansion images and plotting the vectors of these distortions. The acquisition of these vectors is through two possible approaches: B-spline non-rigid registration and optical flow-based assessment.

The non-rigid approach attempts to warp the pre- and post- image data to one another, and the resulting transformations provide the information for the distortion maps.

Conversely, the optical flow-based approach assumes isotropy in the images and attempts to match similar regions to one another.

This data can then be used to calculate the RMSE using the acquired position data of registered structures between both images. Calculation of RMSE as a function of length measurement is done to understand the difference in length between pairs of points in each image, providing a difference value that is incorporated into the error. By understanding the length scales at which errors occur, it becomes possible to fully assess expansion data.

By providing a more robust methodology in the plates, this chapter presents the acquisition of pre-/post-expansion data and analysis of the acquired data in the context of the microplates. Therefore, considering the degree to which the expansion plates perform relative to the gold standard of expansion microscopy.

4.2. Results

4.2.1. 2D Pre/Post Image Acquisition:

4x expansion microscopy in the microplates was validated using the traditional gold standard of pre/post expansion imaging, wherein the same cells are imaged prior to expansion and post expansion. This allows for distortion mapping and calculations of root-mean-square error in the datasets to assess the anisotropy of expansion.

Pre- and post-expansion Airyscan image pairs of cultured HeLa cells stained directly with AZ488 NHS ester, an analog of Alexa Fluor 488 NHS characterised previously as an ExM counterstain, provided an effective measure of tracking the same region with

a minimal or known amount of gel rotation. The greater fluorescence and non-specificity of the NHS ester made it simpler to identify previously imaged cells post-ExM. Multiplexed data was also obtained with KDEL/NHSAtto594, KDEL/NHSAZ488 and NUP98/NHSAZ488. KDEL, targets the endoplasmic reticulum allowing for structural information outside of the nucleus that spans into the cytoplasm. NUP98, targeting the nuclear pore complexes present on the nuclear membrane. And paired with the ester label NHSAtto594 or NHSAZ488 for their nondescript labelling pattern. This allowed for direct comparison between pre- and post-ExM imaging demonstrating the resolution improvement provided by ExM (Figure 4-1).

4.2.2. 2D Alignment of Pre/Post Images

Alignment of the pre- and post-ExM matching images (Figure 4-2) was tested using imageJ plugins: “Linear Stack Alignment with SIFT” (Lowe, 2004), and “BUnwarpJ” (Arganda-Carreras et al., 2006). Linear Stack Alignment with SIFT remained the most consistent with the same preparation performed as per section 2.6.2 prior to running the plugin. The mosaic-like appearance in the BUnwarpJ aligned data introduces artefacting the adjusted post-expansion image. As this non-rigid transformation data would be used to calculate the RMSE, it is important to determine the degree of influence this has on the data and further investigate. Therefore, this approach may pose a broader problem to the community increasing the need for a standardised approach.

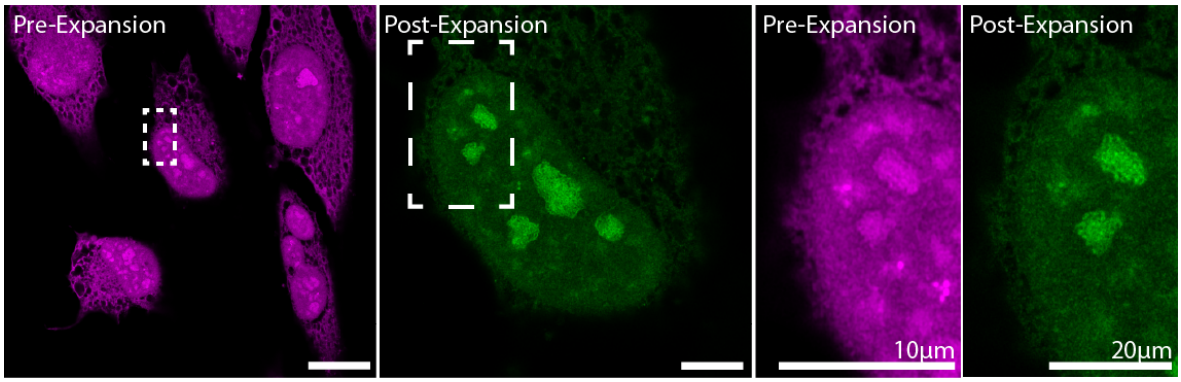

Figure 4-1: Example of pre/post-expansion images and visual resolution improvement between them

HeLa cells stained with NHSAZ488. Pre-expansion images show a widespread staining with significant nuclear staining, including intranuclear densities. The resolution of which are improved upon post-expansion imaging, revealing further structural nuance. **Scale bar:** 20µm (scaled to pre-expansion size).

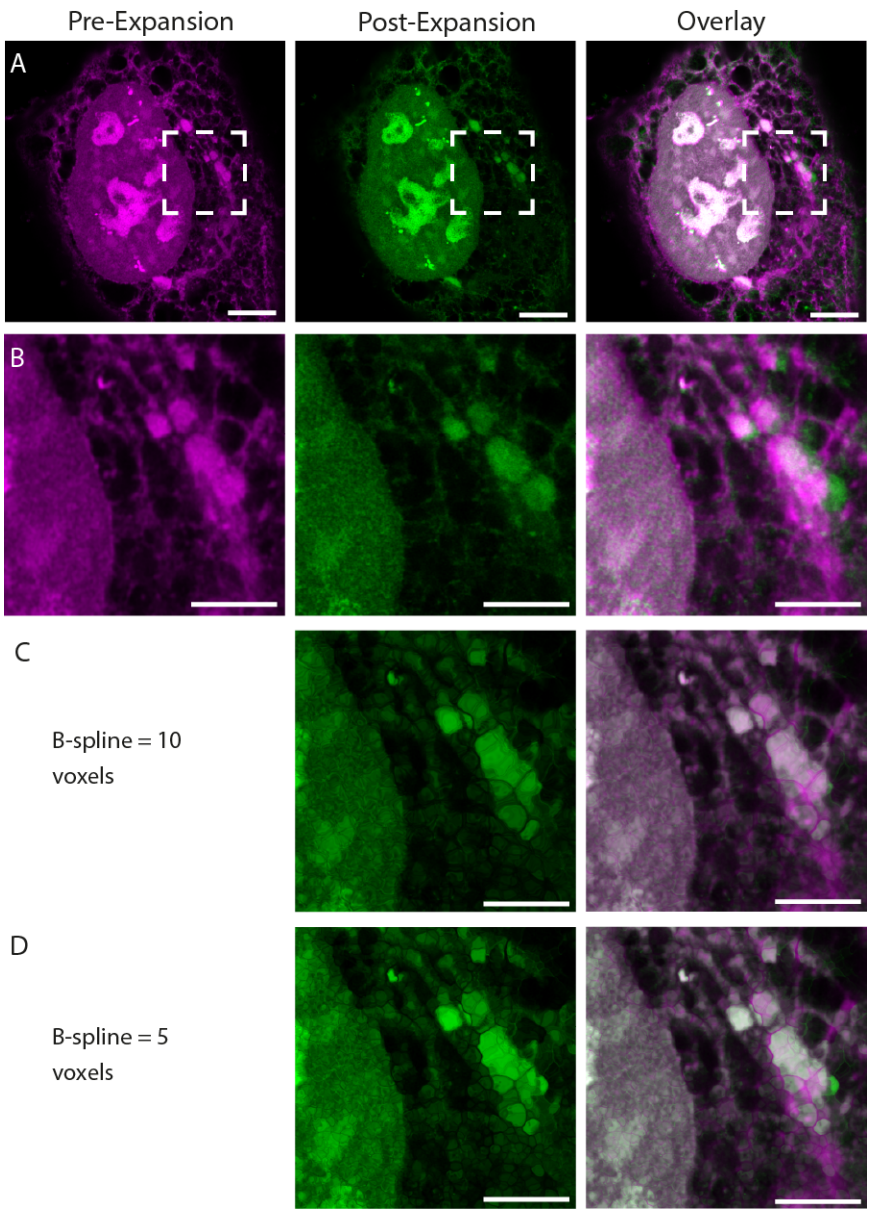

Figure 4-2: Alignment of pre-/post-expansion images with "Linear Stack Alignment with SIFT" and "BunwarpJ"

Representative HeLa cells stained with NHSZA488. **A:** Full imageset of pre-/post-expansion and overlay showing alignment. Dash marked region indicating area shown in subsequent panels. **B:** SIFT aligned data, using similarity approach from uniform scaling. **C:** BUnwarpJ, b-spline approach at 10 voxels. **D:** BUnwarpJ, b-spline approach at 5 voxels. **Scale Bars:** 4 microns scaled to pre-expansion size.

4.2.3. 2D Expansion Factor Calculations

Using the transformation matrix for the aligned image pair the intrinsic expansion factor can be calculated (Table 4-1).

Experiment	Fluorophore	Expansion Factor (±SD)	Count (n)
HeLa Cells	NHSAZ488	3.034 ± 0.607	5
	NHSAZ488	2.853 ± 0.669	7
	KDELAlexa594	3.025 ± 0.677	6
	KDELAlexa488	3.108 ± 0.771	6
	NHSAtto594	3.022 ± 0.859	5
	NHSAZ488	4.483 ± 0.01	3
	NUP98	4.425 ± 0.064	4

Table 4-1: Intrinsic Expansion Factor of the analysed pre- and post-expansion datasets.
Where count (n) refers to the number of paired analysed pre- and post-expansion datasets.

4.2.4. Visualisation of 2D Distortion

Having aligned the sample, distortion maps were produced highlighting the regions with the most anisotropy (Figure 4-3). Distortions were most common near the boundary of the cell, near the interface of internal compartments (ER and plasmalemma of the cell) and in intra-nuclear structures (Figure 4-3).

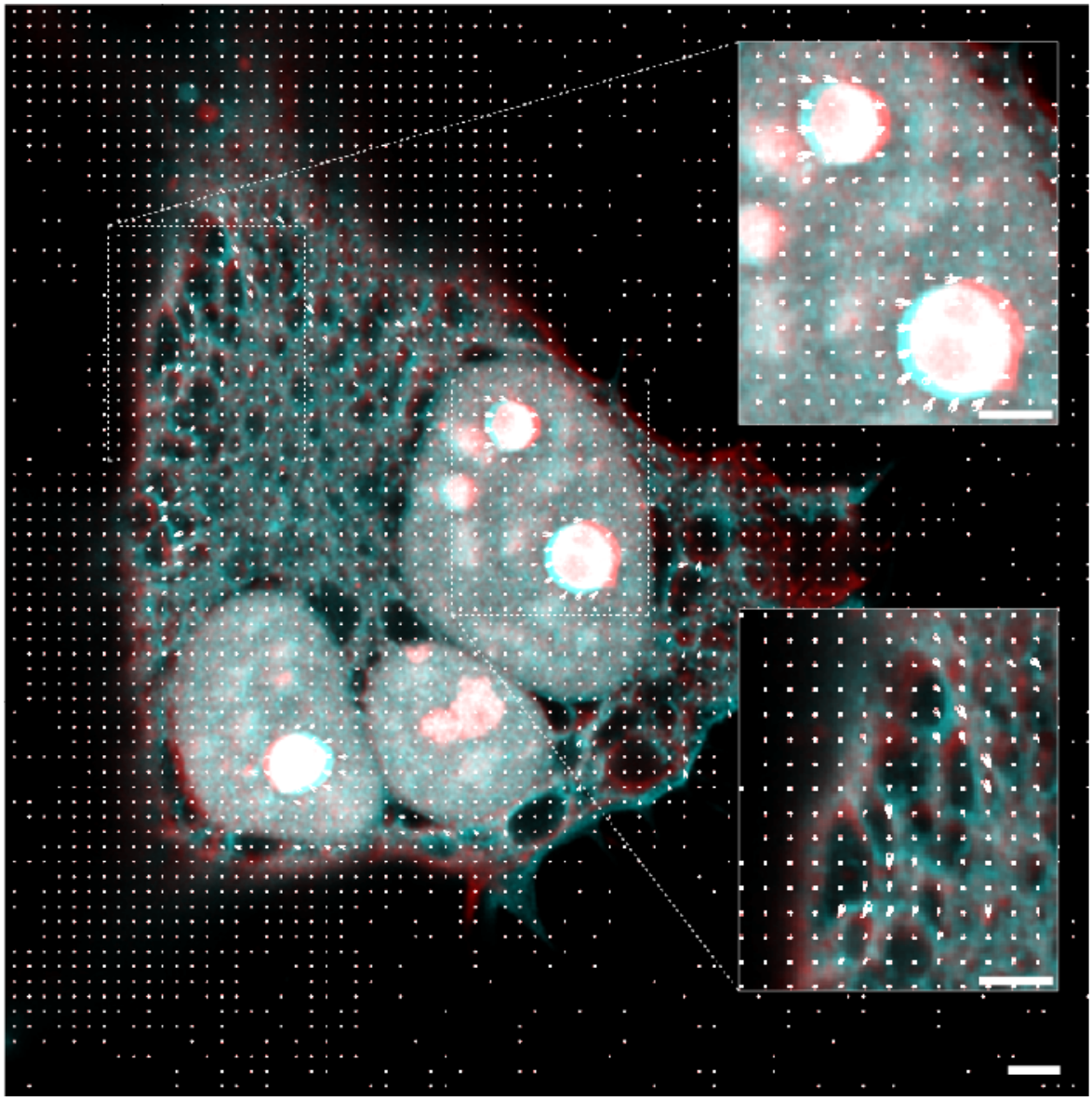

Figure 4-3: Distortion Map of HeLa cell stained with NHSAZ488

Distortion map of HeLa cell stained with NHSAZ488, showing widespread non-descript staining, inclusive of cytoplasmic and nuclear regions. Sub-regions illustrate the more prominent distortions near the borders and denser structures. **Scale Bar:** 2µm

4.2.5. Quantification of 2D Distortion

Distortions were calculated as the RMSE as a function of length, allowing us to identify the scale at which the greatest spatial errors occur (Figure 4-4). These spatial errors are extracted based on the comparison between the expanded and original diffraction-limited images and hence the anisotropies and distortions are on a cell-by-cell and image-by-image basis, showing the impact of local distortions at the cellular level. The RMSE shown in Figure 4-4.A demonstrates a ~50 nm average RMSE across all length scales. This suggests a ~1.2% error rate relative to the largest length scale of ~40 microns, which is in line with expected anisotropy of 1-3% in the conventional approach.

Secondary to this, distortion vectors were visualised by polar plots, which reports any systemic asymmetries or directionalities in the distortion present. The associated polar plots shown in Figure 4.-4.B, shows a uniform distribution in the distortion vectors with an average magnitude of 200 nm. This is suggestive of general anisotropic expansion, in line with what can be qualitatively seen in Figure 4-3 (above).

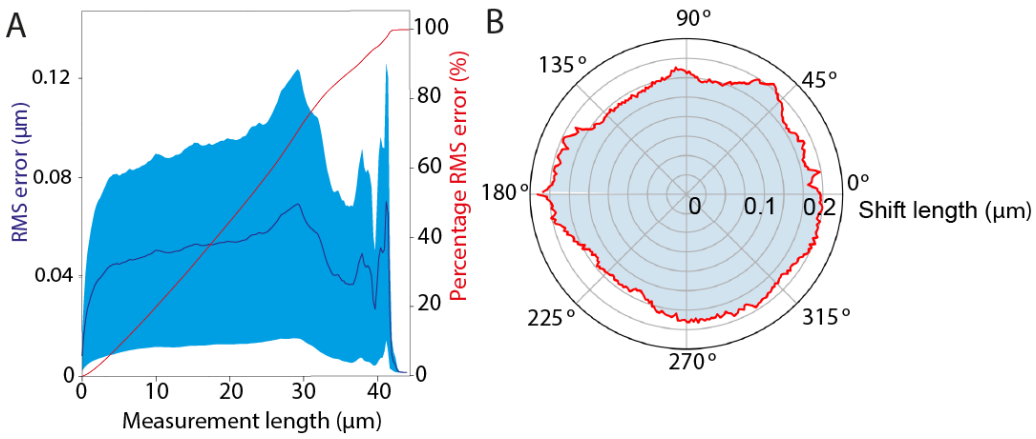

Figure 4-4: Quantification of Distortions through RMSE and Angular Plot

A: Combined plot of: RMSE (blue line with standard deviation), cumulative normalised RMSE (red line), both as a function of length measurement. Showing RMSE of ~ 50 nm. **B:** Polar plot of average distortion vector magnitude (radial axis) against vector direction (angular axis). Showing no clear directional bias to the data.

4.2.6. Multispectral Distortion Analysis of 4x Expanded HeLa cells in Microplates

With a complete imaging and analysis pathway, multispectral imaging can provide a robust insight into the functionality of the microplates and how distortions are assessed. Hence, an ExM experiment using HeLa samples stained with NHSAZ488 and co-immunostained with KDEL, a peptide sequence found in distal endoplasmic reticulum was performed (Figure 4-5). The figure shows registered pre- and post- 4x ExM images individually, after which the overlay of the two for comparison. This is alongside the distortion vector maps, highlighting the distortions present and allowing comparison between the two channels. In particular, the comparison between the analysis of both channels was used to assess distortions associated with linkage

errors which are unique to each label. Allowing further insight into the distortions present.

This is made clear through the non-descript nature of the NHS ester. Information in this channel is useful in recovering distortion information present in the areas devoid of the KDEL antibody label. In this case the nucleoplasm and perinuclear regions are most predominant. Thus, allowing for a more complete picture of the distortion present in the region and how this impacts the data.

The improvement in spatial resolution and contrast as a result of the expansion process is made clear by further overlaying the two channels and pre-/post-ExM images.

Quantitatively, the RMS error plots here illustrate the normalised error from a collection of samples, the cumulative error as a percentage, and the angular distortions present in each channel (Figure 4-6). The ubiquitous staining of the NHSAZ488 ester allows for greater reporting at longer length scales when calculating the RMSE plots. Comparatively, the more localised and structured pattern KDEL exhibits across the cell results in a proportionally smaller number of reports at larger length scales, demonstrated by the lower deviation in the cumulative RMSE value at lengths greater than 35μm.

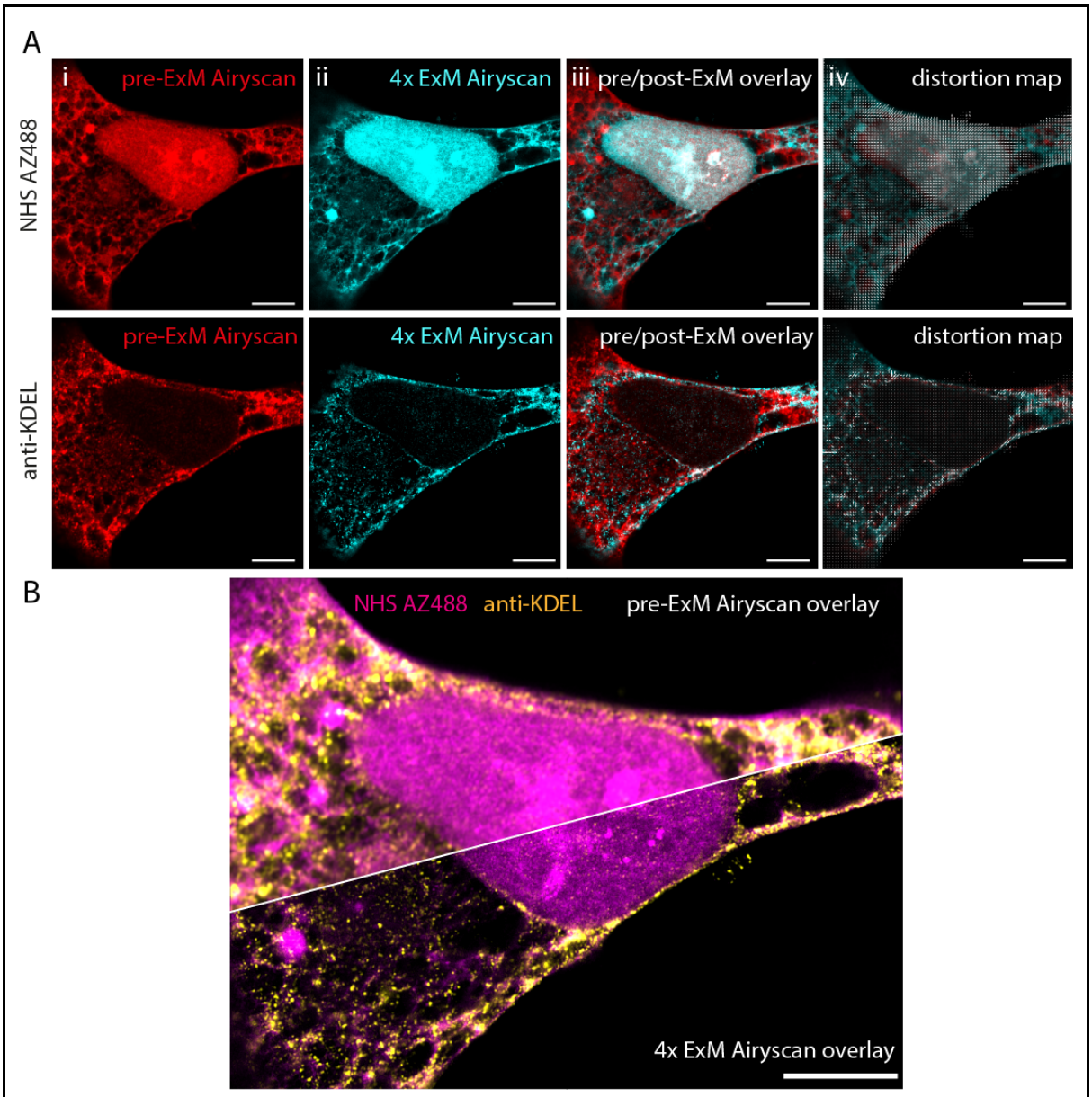

Figure 4-5: Representative multichannel image of HeLa cells stained with NHSAZ488 and anti-KDEL with distortion vector maps

A: i) registered pre-expansion Airyscan images, **ii)** registered post-expansion Airyscan images, **iii)** overlay images of the pre- and post-expansion images. **iv)** distortion vector map overlaid onto the composite images. **B:** Combined pre- and post-expansion multichannel image, showing the difference in contrast and spatial resolution. **Scale Bar:** 5µm (scale corrected by expansion factors in post-ExM images).

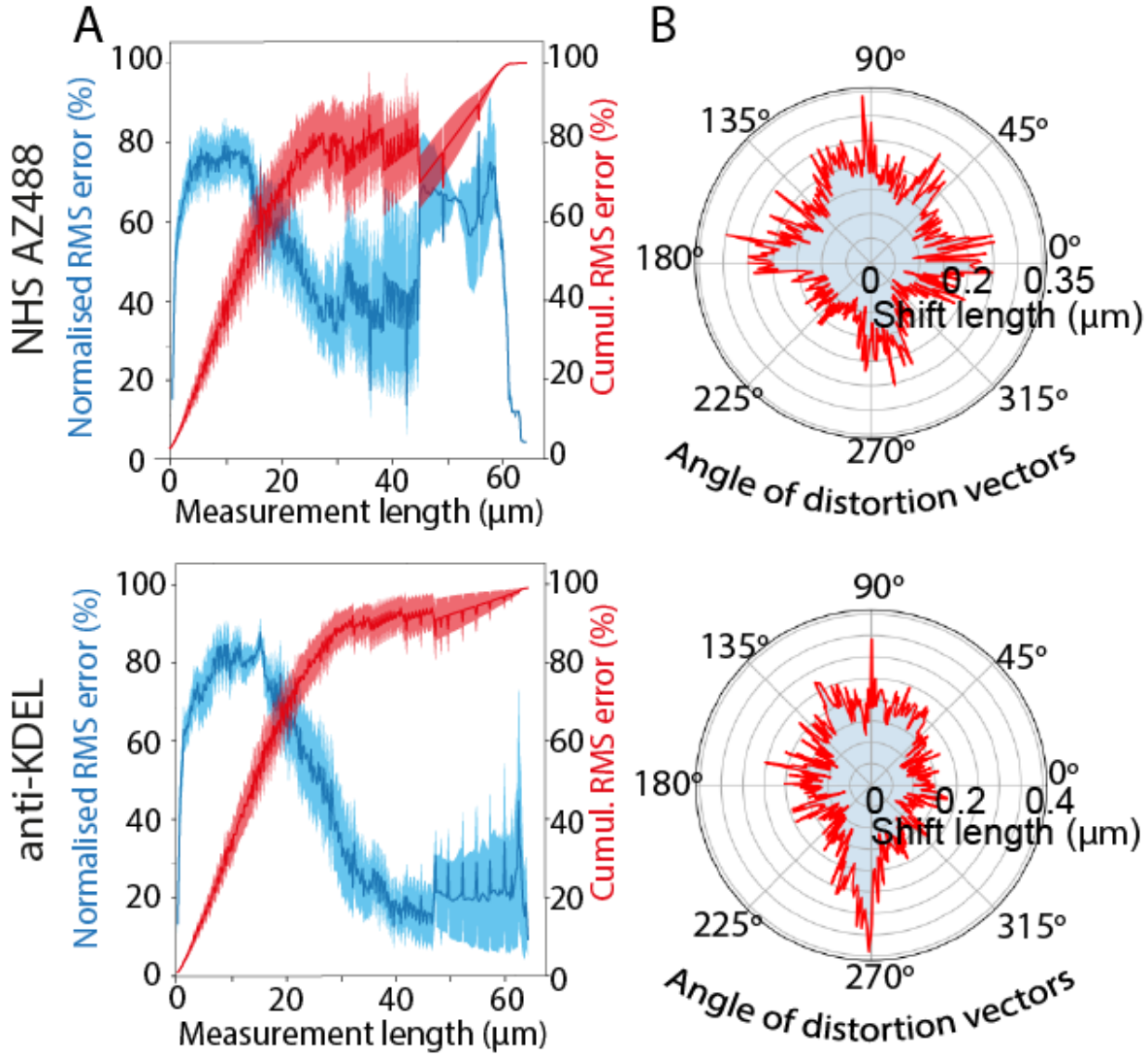

Figure 4-6: RMS error and angular distortion plots of 4x expanded HeLa cells labelled with NHSAZ488 and anti-KDEL

A: RMS error, averaged between 8 image pairs from 8 cells across 4 wells from two microplates, against length measurement. Blue; normalised RMS error, with shading indicating standard deviation. Red; normalised cumulative RMS error, with shading indicating standard deviation. **B:** Average distortion vectors against angular direction, plotted as a polar plot. Showing directional bias in the KDEL channel.

The multi-channel ExM imaging showed consistent distortion within the nuclei and at the nuclear boundary. The dense presence of structures and limitations in accessibility within the nucleus are likely restricting access to the gel monomers as they attempt to cross the nuclear envelope. Thus, resulting in distortions in these nuclear regions.

To investigate this further the analysis pathway was performed on HeLa cells co-stained with NHSAZ488 and anti-NUP98. NUP98, as a key component in the nuclear pore complex, should reveal notable distortions in these structures identifying whether these are artefacts from the ester stain or existing ExM distortions associated with the nucleus.

Qualitatively, distortions were clear in both channels, particularly either side of the nuclear envelope (Figure 4-7). Due to its persisting structure, the registration is favoured towards the nuclear envelope, this was apparent in Figure 4-7.B showing the difference in distortions between intranuclear and perinuclear structures. Structures on both sides of the nuclear envelope have a less prominent alignment relative to the structures in the nuclear envelope itself. Therefore, based on the registration these regions were subject to expansion distortions. By comparing between the two channels, the additional context provided by the wider ultrastructure in the ester channel, allowed for verification of the persistence of distortions.

This is compounded by the angular of the distortions being directionally similar between the two channels (Figure 4-8). Suggesting similar distortions profiles persisting between the channels. Further contextualising the distortion maps with the

RMS error and angular distortion plots, measurements of the scale of the error as well as the active limitations of measuring these structures became apparent. This provided useful information for judging the quality of the expansion experiments and demonstrates that intracellular structures can expand at different rates.

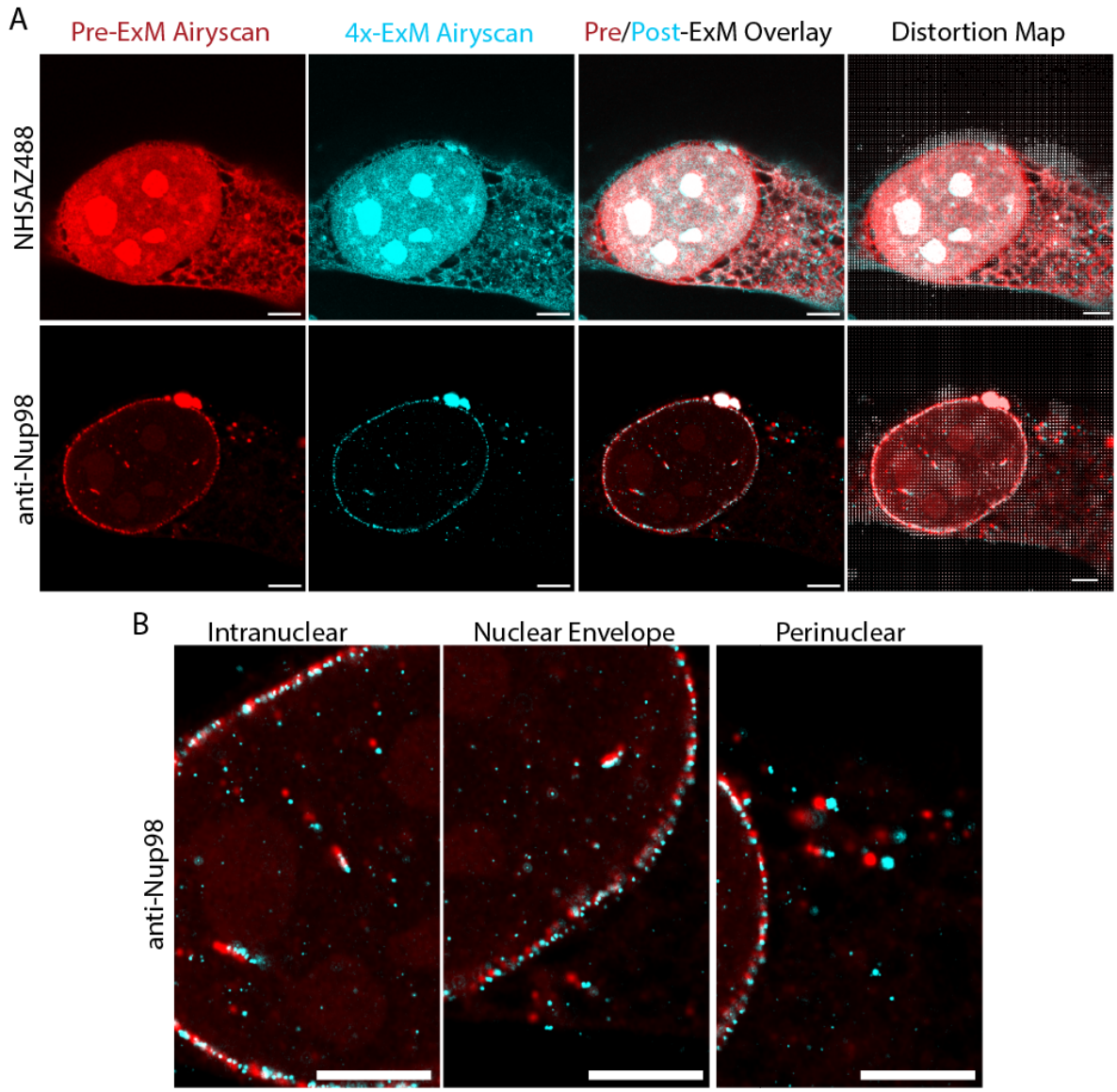

Figure 4-7: Representative multichannel images of HeLa cells stained with NHSAZ488 and NUP98 with distortion maps

A: Registered pre-/post-ExM images with overlay and distortion maps illustrating local area distortions. **B:** Zoomed in NUP98 sections showing distortions at intranuclear, nuclear envelope and perinuclear levels. **Scale Bar:** 5µm (scale corrected by expansion factors in post-ExM images).

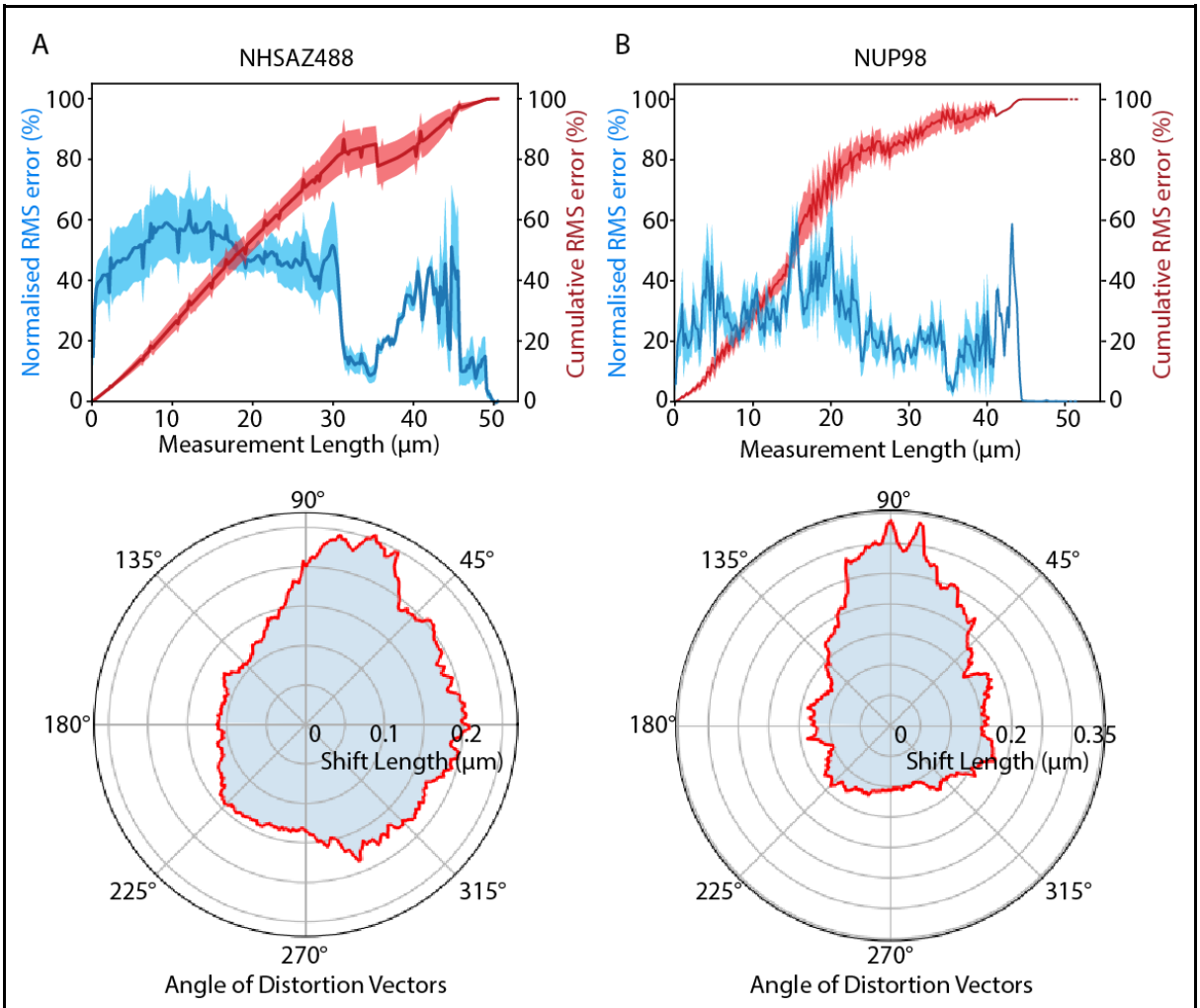

Figure 4-8: RMS error plots and angular distortion maps of 4x expanded HeLa cells labelled with NHSAZ488 and NUP98

A: RMS error, averaged between 6 image pairs from 6 cells across 4 wells from three microplates, against length measurement. Blue; normalised RMS error, with shading indicating standard deviation. Red; normalised cumulative RMS error, with shading indicating standard deviation. **B:** Average distortion vectors against angular direction, plotted as a polar plot.

4.2.7. Multispectral Distortion Analysis of 4x Expanded Drosophila Pupal Wings in Microplates

The Drosophila fly wing tissue was prepared by Samantha Warrington prior to imaging alongside the author. Samantha Warrington provided expertise in Drosophila structural biology to facilitate the experiment. The author provided expansion microscopy experimental and imaging expertise.

Expanding the microplate usage to tissue samples, a similar consistency can be seen with the angular distortion and average local expansion factor between the fluorophore labels. Highlighting the consistency of the approach and the breadth of possible use cases for the microplate.

The denser nature of tissue samples, caused by cells clustering and creating specialised junctions to facilitate connection, can lead to a greater difficulty for monomer infiltration deep into the material. This can lead to greater distortion and hence an optimised preparation and digestion method was used to cast the gel and digest away the cellular structure. The increase in contrast and spatial resolution has improved in the fly wing tissue (Figure 4-9), however, the structural expansion has resulted in clear distortions as when moving away from the centre of the image.

When combined with the assessment of the RMSE, the greatest errors occur in similar directions across both the ester and e-cadherin channels, and this seems consistent across the samples taken (Figure 4-10). The RMSE profiles reveal similar patterns in distortion distribution, revealing the underlying distortion pattern difficult to visually perceive in the distortion map of the ester channel. In the case of tissue samples, the

nondescript labelling of NHSAlexa647 is providing a less contrasting image between the pre-and post-ExM image points. Thus, the global distortion pattern is difficult to qualitatively perceive. However, in the e-cadherin channel the specific but global labelling of the tissue provided detailed ultrastructure unmarred by the increased density. In particular, structures can be better registered, and the distortions present more easily distinguished.

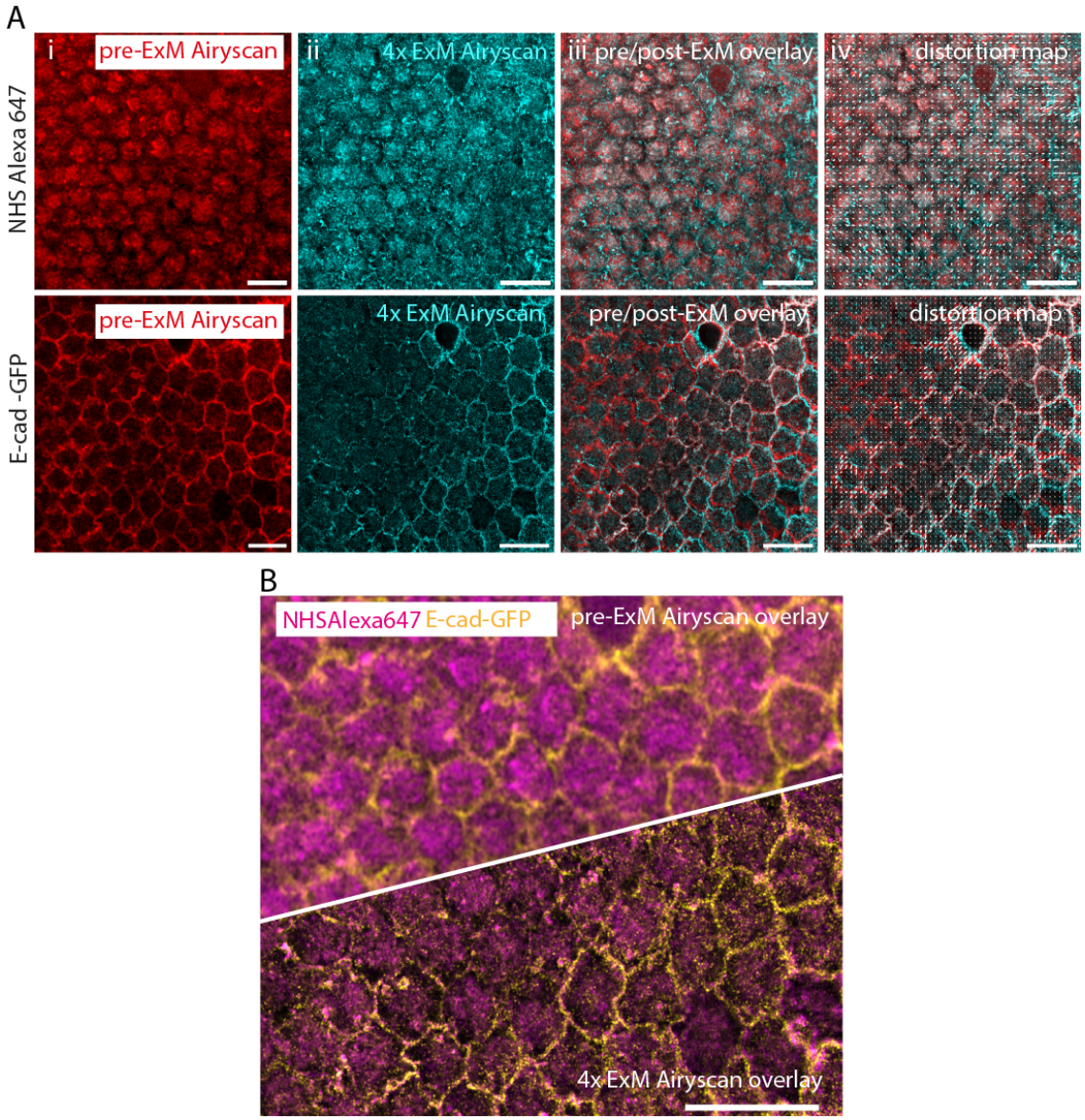

Figure 4-9: Representative multichannel image of Drosophila pupal wings stained with E-cad-GFP and NHSAlexa647 with distortion vector maps

A: i) registered pre-expansion Airyscan images, **ii)** registered post-expansion Airyscan images, **iii)** overlay images of the pre- and post-expansion images. **iv)** distortion vector map overlaid onto the composite images. **B:** Combined pre- and post-expansion multichannel image, showing the difference in contrast and spatial resolution. **Scale Bar:** 5µm (scale corrected by expansion factors in post-ExM images).

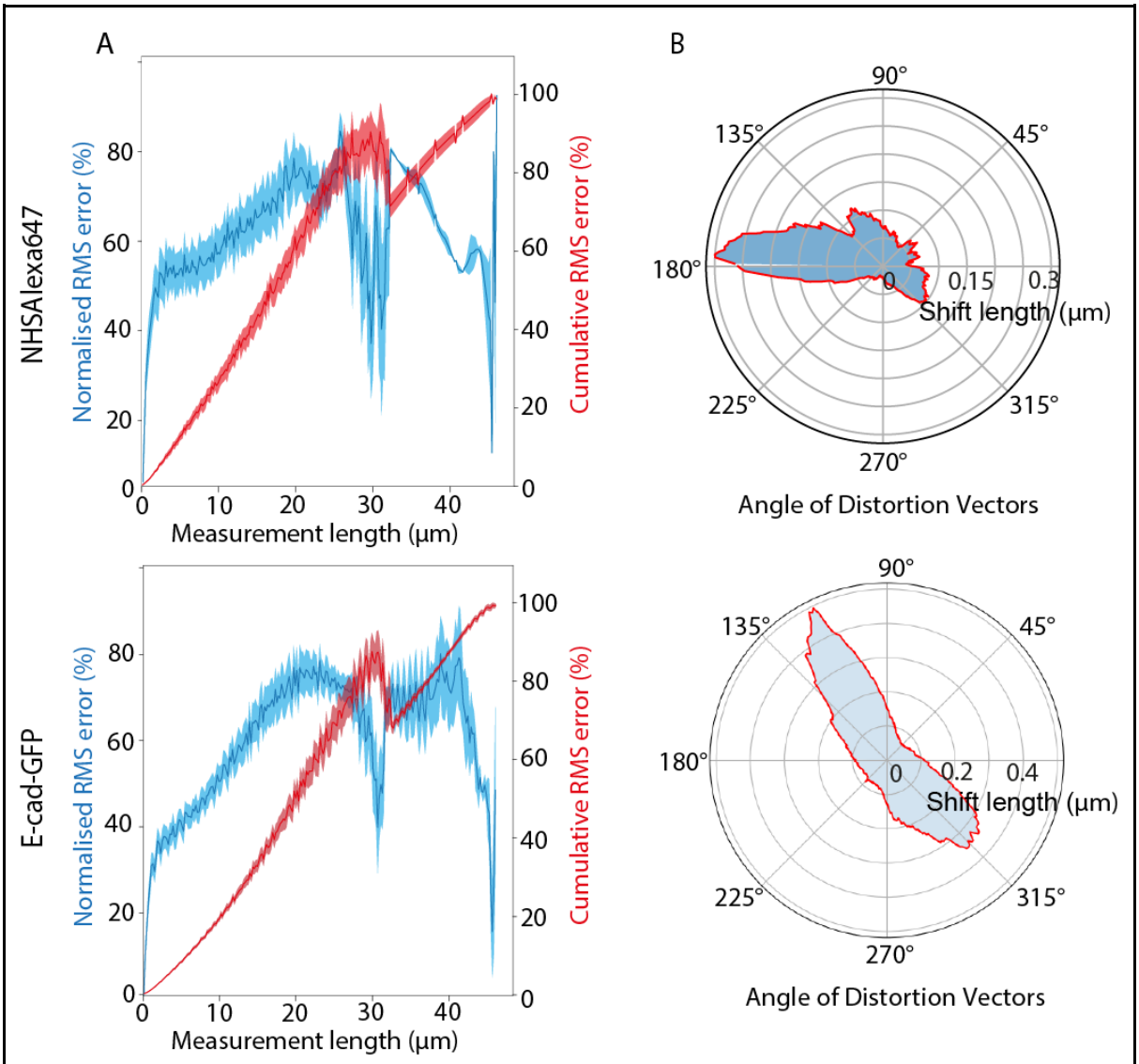

Figure 4-10: RMS error and angular distortion plots of Drosophila pupal wings stained with NHSAlexa647 and E-cad-GFP

A: RMS error, averaged between 9 image pairs from 2 fly wing tissue samples, against length measurement. Blue; normalised RMS error, with shading indicating standard deviation. Red; normalised cumulative RMS error, with shading indicating standard deviation. **B:** Average distortion vectors against angular direction, plotted as a polar plot. Shows directional bias in both channels.

Experiment	Fluorophore	Mean ± Standard Deviation	Count (n)
Fly Wing Data	anti-E-cadherin-GFP	3.051 ± 0.065	9
	NHSAtto647	3.048 ± 0.075	8

Table 4-2: Intrinsic expansion factor of Drosophila pupal flywing data, stained with anti-E-cadherin-GFP and NHSAtto647
Where n = number of paired pre-/post-expansion samples.

4.2.8. 2D Multi-Time Point Imaging

Making use of the ability to track the sample, repeated imaging of HeLa cells was performed at pre-digestion, post-digestion and post-expansion time points (Figure 4-11). It is important to note that the greatest distortion here is visible between the pre- and post-digestion timepoints (Figure 4-11.D). This indicates that the area wherein distortions are most likely to occur and propagate from is during the digestion process. These errors also appear to cluster around the more prominent landmarks in the image.

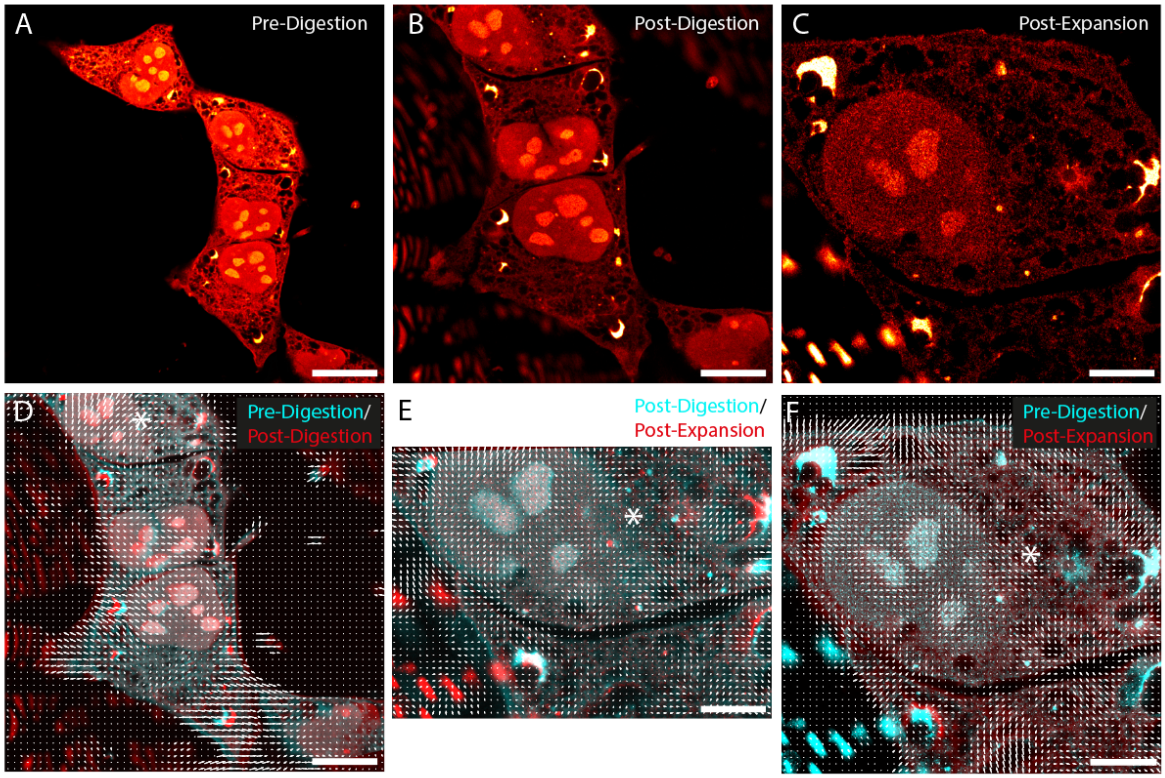

Figure 4-11: Visualisation of 4x ExM distortions in HeLa cells stained with NHSAZ488, at pre-digestion, post-digestion and post-expansion timepoints

A: pre-digestion, **B:** post-digestion, and **C**: post-expansion time points. **D, E, F:** Distortion maps of data between the timepoints. **D:** Overlay of pre-digestion (cyan) and post-digestion (red) images. **E:** Overlay of post-digestion (cyan) and post-expansion (red) images. **F:** Overlay of pre-digestion (cyan) and post-expansion (red) images. The distortion maps illustrate wide, low-scale distortion, with more significant distortion towards the edge of the image data. The asterisk denotes the same cell which has increased in size due to the expansion process. **Scale bar** = 20µm

RMSE analysis of this data qualitatively supports the claim, showing a larger average RMS error in the pre-/post-digestion comparison of ~ 0.04µm. Compared to ~0.02µm in the post-digestion/post-expansion comparison and ~0.004µm in the pre-digestion/post-expansion comparison (Figure 4-12).

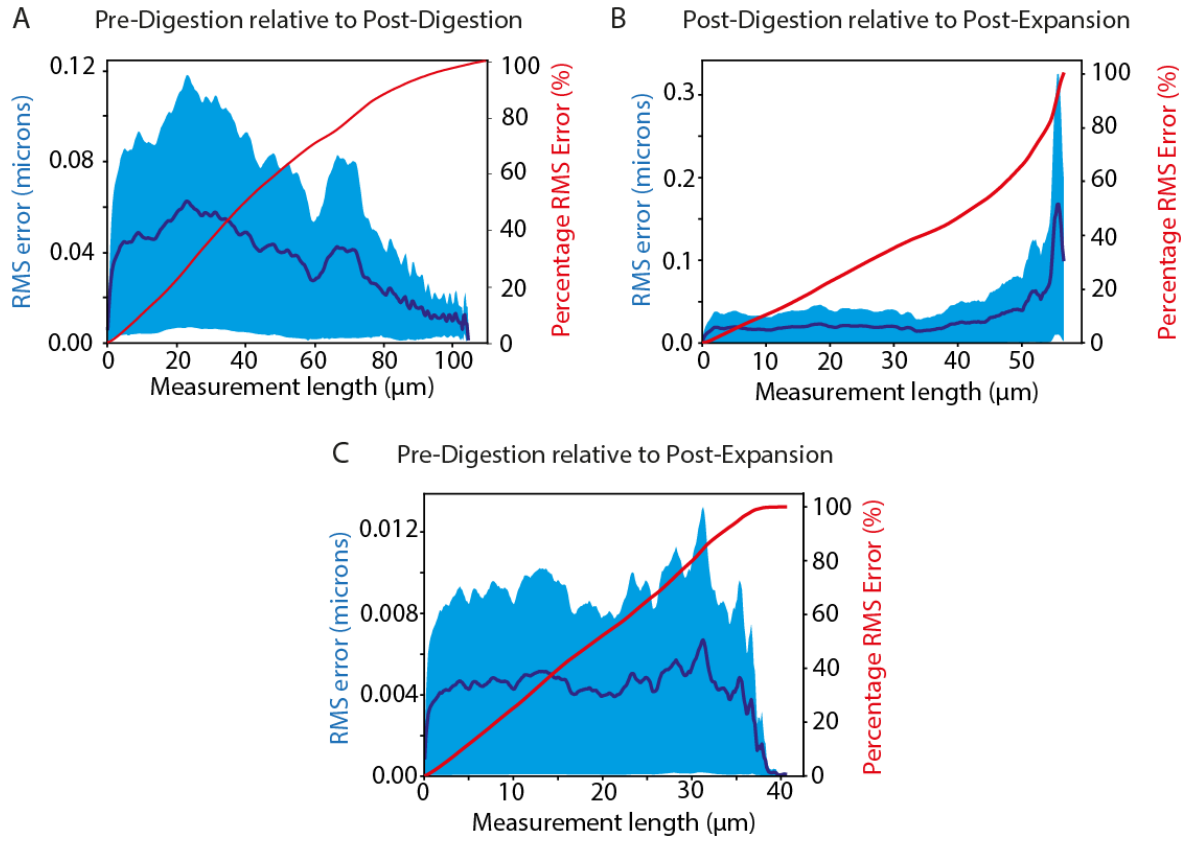

Figure 4-12: RMSE plots comparing error between experiment timepoints; pre-digestion, post-digestion and post-expansion

RMSE (solid blue line; standard deviation shaded) from the paired comparisons, and cumulative normalised RMSE (red line) as a function of the length measured.**A**: Pre-Digestion vs Post-Digestion, showing error ~40 nm. **B:** Post-Digestion vs Post-Expansion, showing error ~30 nm. **C:** Pre-Digestion vs Post-Expansion, showing error ~ 4 nm.

The pre-/post digestion comparison point also featured a modest expansion of the sample (by a factor of ~1.5x). Comparatively, the post-digestion/post-expansion time points revealed a further ~2.5x expansion factor with smaller proportional distortion vectors relative to the new dimensions of the cells (Table 4-3). This resulted in an overall ~3.7x expansion factor for the cells.

Experiment	Fluorophore	Expansion Factor (± SD)	Count (n)
Multi-point Imaging			
Pre-Digestion vs Post-Expansion	NHSAZ488	3.749 ± 0.028	2
Pre-Digestion vs Post-Digestion	NHSAZ488	1.549 ± 0.035	2
Post-Digestion vs Post-Expansion	NHSAZ488	2.416 ± 0.101	2

Table 4-3: Intrinsic expansion factor of the multi-point imaging datasets paired by timepoints. Pre-Digestion, Post-Digestion, and Post-Expansion timepoints
Where n = number of paired pre-/post-expansion samples.

4.2.9. 2D Pre-/Post-ExM Analysis of the Impact of Different Objective Lenses on Images in Microplates

Expansion microscopy is reliant on the current hydrogel-based formulations. In combination with the drop in fluorescence intensity, inherent to all ExM samples, it is important to consider the refractive index and light collecting ability of the objective lens used. Hence, 40x water (NA 1.2) and oil immersion (NA 1.3), objective lenses were used to image pre- and post-ExM imaging in microplates and the signal-to noise ratio assessed as a measure of light collecting ability.

Qualitatively, the pre-expansion image collected with the oil immersion lens appears slightly more out-of-focus than the water immersion lens twin. However, this difference is indistinguishable in post-expansion imaging between the two lenses (Figure 4-13). Structures in the post-expansion are clearly defined suggesting the difference in lenses is less apparent at the larger post-expansion length scales.

When assessing the signal-to-noise ratio in the images the drop-off in SNR between pre- and post-expansion was as expected. This drop-off was consistent between the water and oil samples in regard to the magnitude and fold change in SNR between them (Figure 4-14).

The calculations of the local expansion factor showed similar values at an average of ~3.2x EF in both water and oil datasets, averaged over 8 and 7 image pairs respectively (Table 4-4).

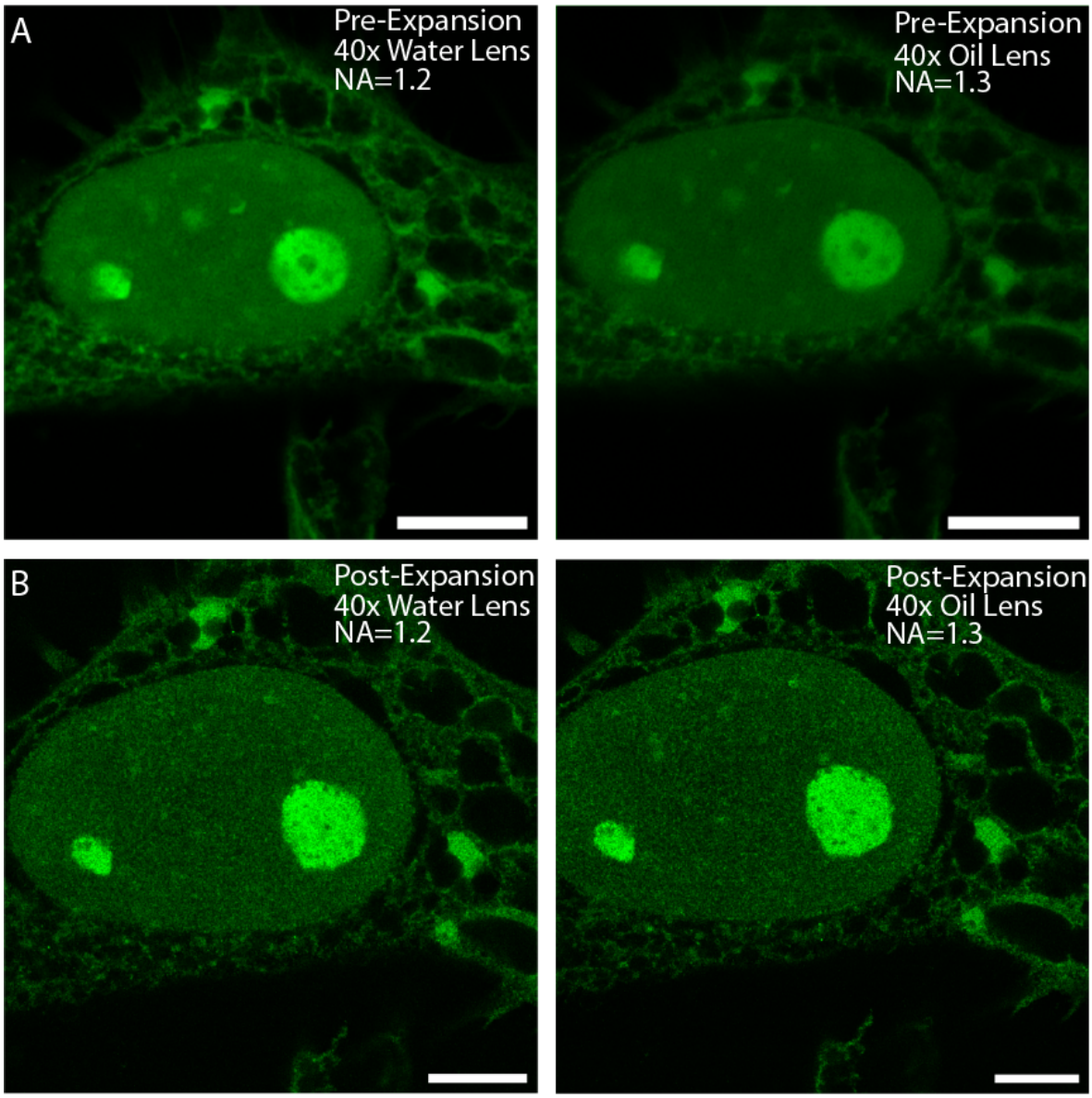

Figure 4-13: Qualitative comparison of pre-/post-expansion images collected from the same region with 40x water and oil objective lenses

HeLa cells stained with NHSAZ488 imaged by Airyscan, showing similar image quality for the microscope setup used. **A**: Pre-expansion images taken with water (left) and oil (right) lenses. **B**: The same cells re-scaled post-expansion, imaged with water (left) and oil (right) lenses. **Scale bar**: 10 µm

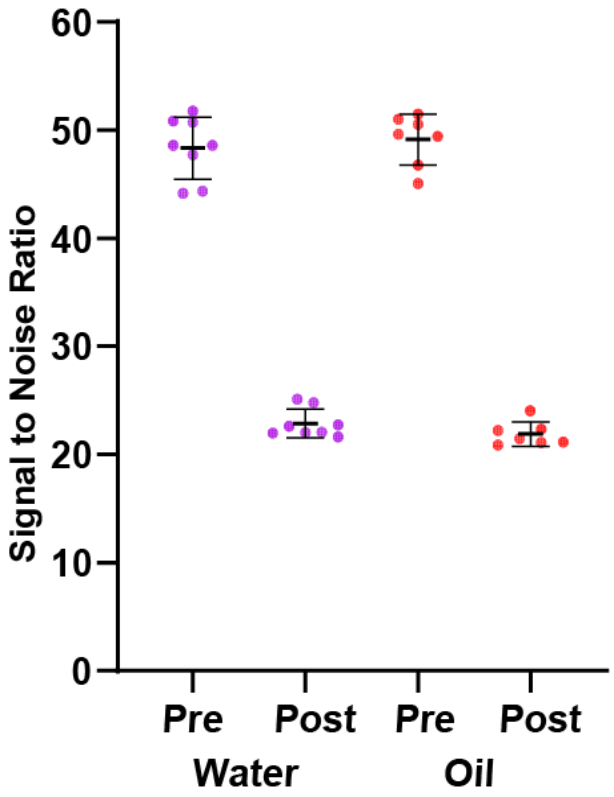

Figure 4-14: Dot plot of mean signal-to-noise ratios from 8 pre-/post-expansion images

Figure shows similar SNR between the water and oil objective data at the same image points of pre-expansion and post-expansion. SNRs were estimated using the ImageJ plugin, developed by Daniel Sage (*http://bigwww.epfl.ch/sage/soft/snr/*)

Experiment	Fluorophore	Mean ± Standard Deviation	Count (n)
Water vs Oil Immersion			
40x Water Objective (NA 1.2)	NHSAlexa488	3.201 ± 0.412	8
40x Oil Objective (NA 1.3)	NHSAlexa488	3.234 ± 0.391	7

Table 4-4: Intrinsic expansion factor of the water vs oil immersion lens datasets.

4.3. Discussion:

4.3.1. Image Acquisition and Region Tracking

Pre-/post-expansion image tracking has remained a problem for ExM and led to the community actively finding alternative approaches to understanding the distortions and expansion of their samples. This is due to three key factors: the difficulty in pattern matching, fluorescence reduction from bleaching and spatial separation, and imaging region loss from gel-based issues. On these factors the microplate approach can be considered superior to the traditional approach.

The difficulty in finding the same region between pre-/post-ExM imaging is directly tied to the structure remaining of similar shape and intensity to allow for identification. The spatial separation of fluorophores leads to a direct decrease in fluorescence density and the added effect of bleaching from pre-ExM imaging decreases the fluorescence further. The issue of signal retention is a known factor in the ExM community, and several papers have explored this issue. Alexa 488 and Atto647N retain ~57% of their signal (Chen et al., 2015), whereas, AF647 only retains ~7% (Tillberg, 2021). Hence, fluorophore selection is important when factoring in pre-post-ExM imaging and needs to be accounted for in accordance with the expected fluorescence loss from the factors above: the expansion process, signal retention, and bleaching.

The microplate approach addresses bleaching indirectly. The configuration of the microplates allows for keener tracking of the gel via a known geometry thus reducing the search area when looking for the same cells post-expansion. By reducing the search area and by extension time the exposure of a sample to non-acquisition-based bleaching is reduced thereby reducing fluorescence loss. Specifically, as the gel can

only be in four possible orientations due to the geometry of the well and gel, identification of the same region now possesses fewer degrees of rotational freedom. Overall, by combining the geometry-based region constraints, making finding the same area simpler, with the reduction in fluorescence exposure, signal is more likely retained through the post-ExM imaging process.

The risk of losing an area previously imaged pre-expansion is a considerable issue. Areas imaged in prior to the ExM process are difficult to define and identify in the traditional approach without meticulous rigor. Factors such as coverslip rotation, gel rotation and preparing the gel for post-ExM imaging can result in losing track of the regions for identification and imaging in post-ExM. In the traditional approach, an expanded gel is divided into sections that are placed into chambers for imaging. This process can actively result in loss of the regions imaged in pre-expansion.

The microplate approach tackles this by directly eliminating the need for manual handling of the gel directly. Whilst the silicone inserts still require manual handling the main risk is a singular time on their removal from the well. Whereas in the traditional approach, the degree of manual handling is notably greater thereby increasing the number of opportunities for gel loss, damage or sample loss. The entire process being performed in the microplates has resulted in an approach to image acquisition that, assuming adequate fluorophore intensity, can be reduced to imaging in pre-expansion and noting the approximate location within the gel and then searching said region in the expanded gel. This simplifies the process, and ensures that imaged regions remain in the gel, as the gel is never removed from the well.

This method remains limited to 4x expansion recipes; however, the principles can be adapted for larger expansion factors.

4.3.2. Pre/Post Image Alignment

Image alignment in expansion samples is predicated on two assumptions: isotropic expansion of the pre-expansion data and feature persistence between pre- and post-expansion. This allows us to generate systems to understand the distortion present by constructing a hypothetical isotropically expanded image and considering the difference in structure between this image and the obtained post-expansion data.

Non-rigid methods were originally used to register pre-/post-ExM data (Chen et al., 2015; Gambarotto et al., 2019; Tillberg, 2021), from which the distortion vectors could be acquired. The use of rigid registration methods in ExM was first introduced by Truckenbrodt (Truckenbrodt et al., 2019, 2018), and has seen usage in analysis similar to non-rigid methods. These techniques follow opposing assumptions due to their method of function.

Non-rigid methods assume anisotropy, mapping the distortion vectors from the warping effect of the registration. Rigid methods, conversely, assume isotropy in alignment and then the distortion vectors are subsequently calculated from the registered data.

The former has the potential for wider application with the advent of machine learning and AI. Collating distortion information from samples and then applying this directly to post-ExM images it may be possible to eliminate pre-/post-ExM imaging. However,

significant progress remains to be made and wide scale data for different samples and gel recipes would be vital to this process.

The rigid registration methodology conversely is more suited to a ground up approach to ExM. By considering both pre-and post-ExM data as the same structurally, deviations from this are distortions. The Farnebäck optical flow algorithm (Farnebäck, 2003), originally designed for two-frame matching, is built to assess the differences between the images based on similar structures being present.

The persistence of features are key to expansion microscopy as a technique and provide landmarks that are key to alignment algorithms such as SIFT (Lowe, 2004). Functionally, SIFT performs a rigid similarity transformation including; translation, rotation and uniform scaling, optimising for the identified features. This allows an isotropic matching of the data and as illustrated above allows for extraction of the local EF via the transformation matrix.

A degree of qualitative judgement is required to assess the performance of SIFT as variables such as the octave value and feature size can impact the effectiveness of the alignment process. This is an issue inherent to registration approaches as sample variance can impact the scope of the algorithm and the preferred structures used to align.

4.3.3. Visualisation and Quantification of Distortions

Being able to comprehend the distortions present both visually and mathematically allows us to understand how the data has been impacted by the sample preparation

process. This methodology was established in the original Chen et al (2015) paper, wherein distortion maps and RMSE as a function of length measurement are used to validate the data. The approach to obtaining this data has been adapted in several different ways from the use of non-rigid to rigid registration methods to variations of the RMSE code in different programming languages.

The code written to analyse the distortion data uses Farneback optical flow as the mechanism to obtain this data and uses gaussian structures to guide its process. This provides the baseline distortion values in each axis used for the qualitative and quantitative analysis approaches.

The distortion maps are then easily generated by overlaying this data over normalised versions of the original pre-/post-expansion images. Depending on the structures involved distortions can be perceived. This is highlighted especially in the NHSester samples as the fluorophores label the majority of the structures.

Distortions are notably more present at boundaries within the cell, such as the cell membrane and nuclear membrane. In particular, intranuclear structures seem to distort to a greater degree. This is likely due to the lower accessibility of antibodies and gel components due to the compact nature of such structures. Digestion also plays a role here, as it is important to maximise digestion whilst minimising fluorescence loss. This leads to erring on a safer digestion period, leading to reduced digestion of these dense structures.

This is clear to see in the ester labelled data as the cells are non-specifically labelled and thus structures from all compartments are able to be imaged. The use of an ester label to provide further context is a possible method through which the reliability of the expansion data can be better assessed. This could also lead to further insight into optimising digestion and thus possibly addressing compartment level distortions.

By comparing the distortions present close to these regions to other distortions in the image, the distortions present can be qualitatively understood. For example, if nuclear distortions are present and show a translation in a particular direction, it is likely that a translational distortion is present in the local region. Comparatively if distortion vectors are in opposing directions as in the fly wing tissue above, the presence of a rotation- or scale-based distortion is probable, which in a tissue sample could result from incomplete digestion of the appropriate regions.

Distortion visualization and quantification are performed to help a researcher better understand their expansion data. However, interpretation of this data is often limited to the expansion factor and a determination of isotropy based on the magnitude of the RMSE. The interpretations of the data herein are attempts to better understand the data presented, however, considerations of how to target and improve the process to remove and eliminate distortions remain sample dependent.

4.3.4. Understanding RMSE as a Function of Length Measurement

Moving forward to quantitative analysis, the RMSE allows a strict look at the scale of distortions across the length of the image. This is calculated based on the distortion

vector acquired previously, which is used to measure the difference in length between pairs of points within each image. The difference between these lengths is calculated and can be plotted against the original length between the pair of points.

By applying this to many points the scale at which distortions are prevalent as well as the magnitude can be assessed. Classically this has been reported as 1-3% (Chen et al., 2015), to which the microplate based data falls comfortably within. Although larger distortions may be present in the image, if the overall structures remain consistent in location and expanded size, then RMSE reporting will tend to a lower value as the difference in lengths calculated remains similar.

This analysis is often time consuming as the number of pixels in the image or features assessed proportionally increases the number of pairs of points to assess at a rate of ((n-1)^2)/2. As an example, a 500x500 pixel square image results in over 31 million pairs of points to assess. This rapidly scales as the value increases and impacts the analysis time similarly.

This was approached in two ways to maximise the useful data and minimise time spent. The primary approach involved identifying structures of interest as the brightest structures in the image and extracting the distortion information for the associated points. This reduced the number of points assessed whilst still allowing for the relevant data to be included in the analysis.

The secondary approach was directed at targeting the data handling of the pairs of points. As each point needs to be measured against all other points within each image,

each set of points were managed in pairs. Subtracting the measured point and working through the mathematical construct of the lower triangle. This meant that the first point being measured took the greatest time to process, with subsequent points taking less time as less data is present at each pass. This data was binned based on predefined bin sizes relative to the image and allowed the measuring of 200,000 points worth of data (~20 billion pairs of points) in approximately 1 hour in python (Refer to methods section 2.6.1 for computer specifications).

This allows the data analysis of these points to no longer be limited by the need for large CPU and GPU computational systems to process the RMSE for larger datasets, thereby extending the access to this analysis approach.

This approach is primarily limited by time, whilst the algorithm allows expansion data of all magnitudes to be processed, as the number of points to be processed increases, so does the burden on the system. This remains an exponentially increasing problem as long as the measurement difference between pairs of points is used to calculate the RMSE as a function of length measurement.

A bespoke application in a more fundamental coding language may be able to handle the data more efficiently and increase the throughput of the analysis.

4.4. Concluding Remarks

The microplates are able to reduce the steps that introduce error and maximise sample consistency. The consistency between the expansion factors and angular distortions

in imaged datasets, speaks to the stability of the technique and with a general RMSE of 1-3% the distortion profile is consistent with the traditional approach.

The tools developed to assist in the analysis open more accessible means of performing expansion microscopy analysis, as well as an alternative approach whilst utilising as much data as possible.

Together the microplate approach with these analysis tools provides a robust novel approach to expansion, that further increases the accessibility of the technique to newcomers and helps to build robustness for veterans.

Chapter 5. Exploring 3D Distortion Analysis and Improvements in Axial Resolution

5.1. Background and Aims:

In ExM, fluorophores are spatially separated by the expansion of the hydrogel matrix. This expansion occurs both laterally and axially, offering a hypothetical resolution improvement in the axial plane. This combined lateral and axial resolution improvement is unique to ExM amongst contemporary super-resolution techniques.

4Pi microscopy through the use of high aperture lenses has been able to achieve axial resolutions approaching 100 nm (Nagorni and Hell, 1998). When combining the 4Pi illumination patterns with STED imaging along the axial direction, resolutions of 30-50 nm have been reported (Hell, 2003). However, early approaches had limited resolution information in the remaining lateral dimensions (Dyba et al., 2003; Dyba and Hell, 2002). IsoSTED nanoscopy using depletion patterns designed for both axial and lateral planes allow manipulation of the PSF thereby increasing the resolution in an isotropic manner. This has allowed for a reported 20-50 nm resolution in all three dimensions (Schmidt et al., 2008).

Modern STED microscopes have allowed for acquisition of the full XYZ information through the use of adaptive optics and refractive index matching to reduce fluorescence loss. The Abberior Easy3D system is one such example, reporting 90 nm resolution in all three axes.

3D STORM takes advantage of the encoded axial information in each particle's PSF and exaggerates this through astigmatic lenses. This results in elliptically structured PSFs which can be used to determine the axial centre of the particle and localise its position in 3D space. This approach results in a reported 50-70 nm axial resolution; however, it is limited by the range of the focal plane (Herrmannsdörfer et al., 2017). This approach is also limited by the imaging depth with deeper planes having reduced localisation accuracy (Huang et al., 2008; Olivier et al., 2013; Xu et al., 2015; Albrecht et al., 2022).

DNA-PAINT's capacity for large-scale multiplexing allows for increased sample collection and compatibility with RESI for further resolution enhancement to the single nanometer range (Schnitzbauer et al., 2017). However, the technique is limited to the coverslip to maximise effectiveness and takes a significant amount of time and specialist equipment to perform.

MINFLUX, utilising a donut laser and multiple image acquisition with sub-nanometer adjustments can effectively target single molecules and trace them in both fixed and live-cell imaging (Balzarotti et al., 2017). However, the time required to collate data across a large field of view is limited to the associated widefield imaging technique.

Comparatively, ExM allows for expansion in all planes as well as being able to image deeper into the sample. The limitation of imaging depth remains due to the expansion process, with larger expansion recipes having the potential to move structure beyond the working distance of the objective. The expansion factor is vital in determining whether structures within the maximum working distance of the

microscope will be moved beyond the field and are a vital consideration when imaging deeper samples.

Current literature in ExM demonstrates the use of matched 2D planes in pre- and post-expansion, wherein an initial 2D pre-expansion image is aligned with the equivalent region post-expansion (Chen et al., 2015; Damstra et al., 2022; Truckenbrodt et al., 2019). The post-expansion image is often a projection of a small Z-stack reflective of the optical section of the pre-expanded data. This is often done based upon viewing the data and selecting for the ends of the Z-stack. Quantitation of the expected size and predicted axial expansion factor of the optical section remain unexplored in the literature.

The expansion process separating fluorophores leads to an additional issue when approaching 3D expansion microscopy. The separation results in a reduced average intensity in post-expansion images compared to pre-expansion. When combined with the increased bleaching from the acquisition of Z-stack data, this limits the accessibility of this approach. Through the investigation of these factors in this thesis, 3D ExM is poised to be established as a standardised technique.

Having demonstrated the capacity of the microplates for ExM, this chapter aims to explore the nature of 3D expansion microscopy. Through the generation of a novel analysis pipeline, leading into the acquisition of practical 3D pre-/post-ExM data, the effects of dimensional bias and optical foreshortening in expansion microscopy will be investigated. This framework will be accompanied by insights into the expansion factor and thus the effect of distortions into and across the axial plane.

5.2. Results

5.2.1. Image Acquisition of 3D Expansion Microscopy

Pre- and post-ExM images of 4x pro-ExM samples were collected to contain as much axial information as possible. In an attempt to collate cell-wide structural information for identifying distortions, NHS ester AZ488 was chosen as the initial fluorescence marker. However, due to bleaching of the NHSAZ488 ester under pre-expansion Z-stack imaging, it became evident that this method was insufficient. The bleaching, combined with the expansion process spatially separating the fluorophores, resulted in no discernible fluorescence during post-expansion imaging making it impossible to find and identify the same regions.

Hence, RPE-1 cells were stained with NUP98 (Alexa594) and ATP5A1 (Alexa488), for nuclear pore complexes (NPCs) and mitochondrial structures respectively. The known regular structure of NPCs was advantageous here as their small size and widespread coverage of the nucleus act to map the nuclear envelope and could better reveal distortions. The antibody stains were visible post-expansion, and regions were identifiable as in the 2D approach (Figure 5-1). The abundance of fluorescence in the nucleus is due to the image plane being close to the coverslip face of the nucleus hence collating data from this region in the final data.

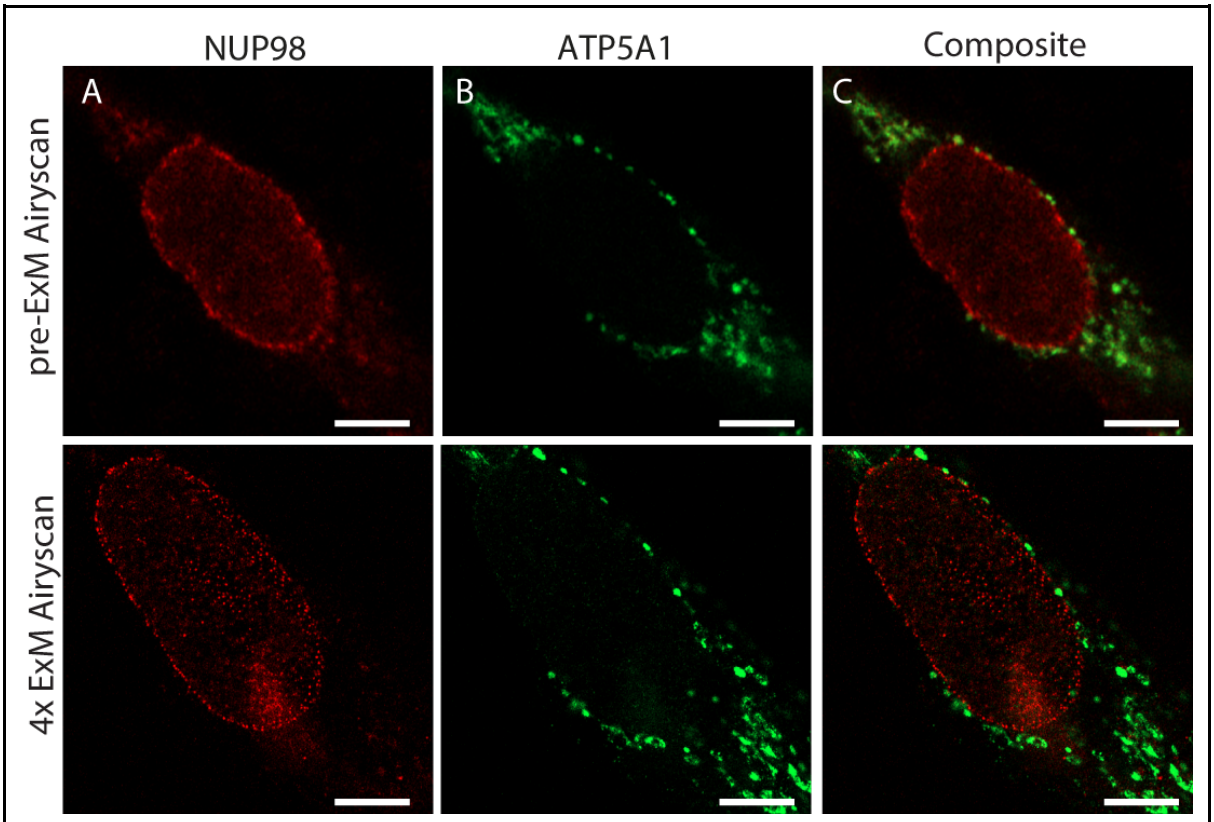

Figure 5-1: Representative pre-/post-ExM images of RPE-1 cells stained with NUP98 and ATP5A1 antibodies

Pre-/post-ExM images of: **A)** NUP98 stained cell, closer to the coverslip, showing nuclear pores, **B)** ATP5A1 stained cell, showing mitochondrial structures in the cell cytoplasm, **C)** composite image. **Scale bar:** 5 µm scaled to pre-expansion size.

5.2.2. 3D Volume Alignment of Pre- and Post-ExM Data with Fujiyama ImageJ Plugin:

The data sets were treated as volumetric structures for data alignment. This is due to the expansion process moving structures apart in space and thus a structure present in a pre-ExM slice may be split over many slices in the post-ExM data. The Fijiyama plugin (Fernandez and Moisy, 2021) allows for this volumetric assessment and employs the block-matching algorithm (Barjatya, 2004) for 3D volume alignment.

This process uses ‘blocks’ composed of voxels of the structure to find matching structural information to aid in the alignment. The resulting output was then assessed to calculate a global transformation that best explains the local correspondences (Figure 5-2).

To facilitate the process an initial manual alignment of the data was performed, with preference given to structures closer to the coverslip. This was done to reduce the influence of any optical aberrations that may occur further into the sample.

The block-matching algorithm was performed using the similarity-based tools: rotation, translation, and uniform scaling. Hence, the resulting transformation matrix contains data reflective of the 3 axes present. However, the considerations for how well the images are aligned was determined by accuracy to 1-2% of the overall image features, a factor dependent on the initial alignment and determined by the output variable of the automated block-matching algorithm.

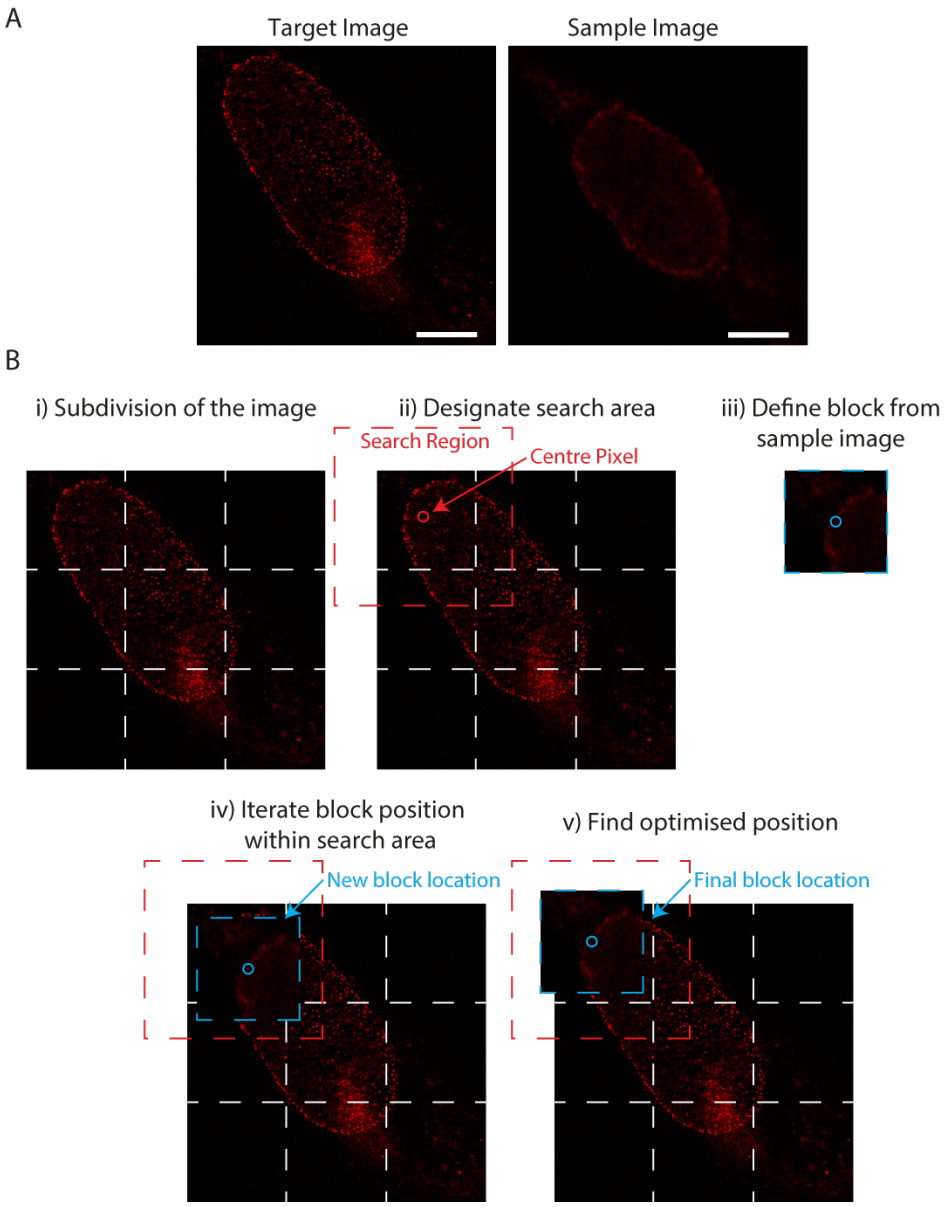

Figure 5-2: Block-matching process for two-image matching, a 2D representation of the 3D process

A) Assign the target (post-ExM) and sample (pre-ExM) images. **B) i)** The target and sample images are subdivided into blocks (voxels). **ii)** A central pixel and a corresponding search volume are designated in the target image. **iii)** The equivalent block from the sample image is defined. **iv)** The sample block is iterated within the 3D search volume. **v)** Information regarding the optimised position is recorded. This process repeats for all blocks.

To address this the use of a standard approach was employed. Firstly, the data would be initially aligned within Fijiyama (Fernandez and Moisy, 2021) with preference to structures near the coverslip. Secondly, the automatic block-matching algorithm with similarity was employed using the default settings. Finally, the aligned data would be viewed to determine if the alignment had occurred and whether it needed to be repeated. This final step was a quality control step to ensure that the data showed alignment in the expected orientation. If automatic alignment resulted in a significant misalignment from the manually aligned data, such that few similar features remained in proximity, the process would be repeated with greater care to align the initial data and prevent a negative bias (Figure 5-3).

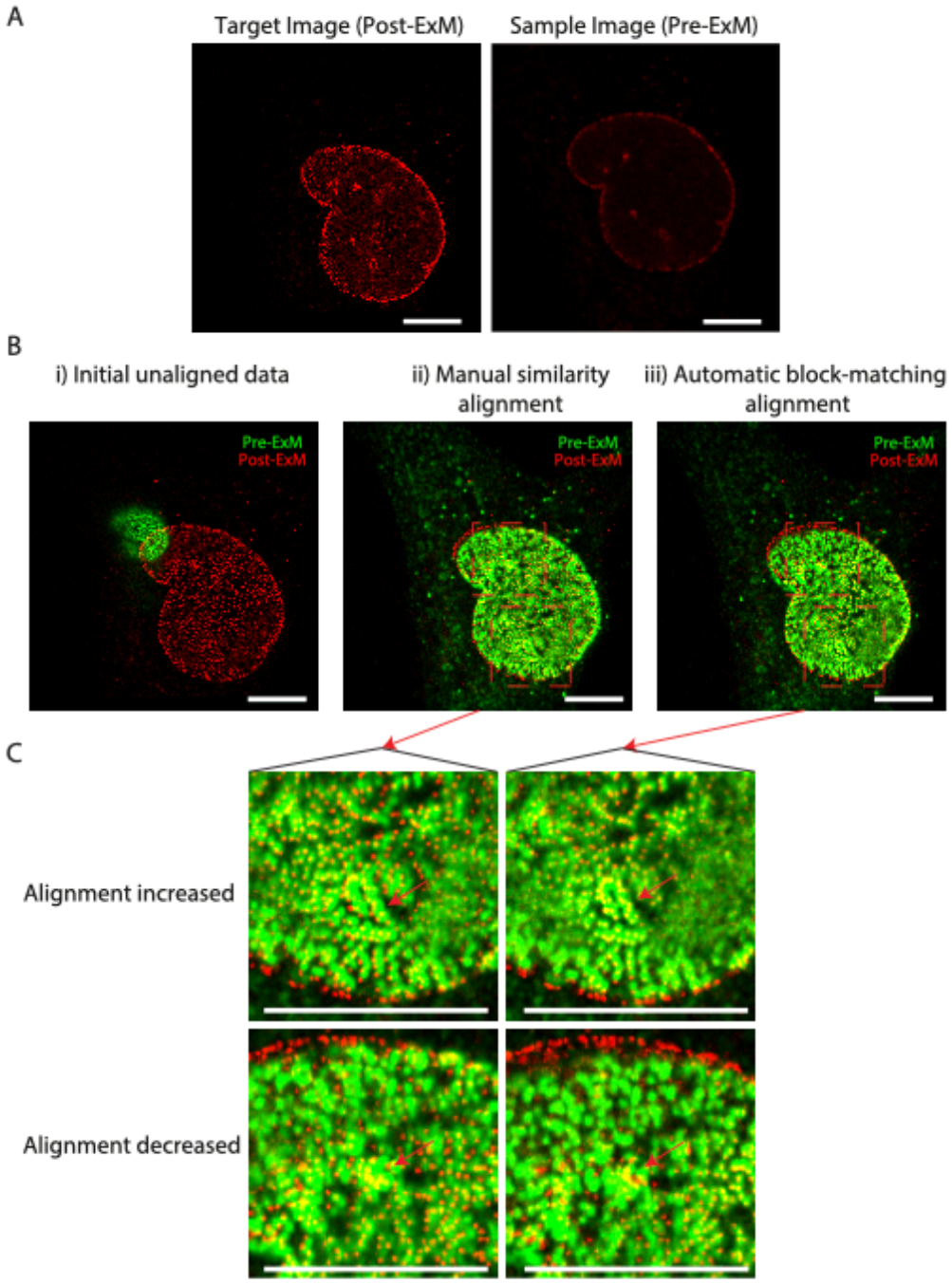

Figure 5-3: Example workflow of Fijiyama usage

A) Designating the pre-/post ExM images. **B) i)** Initial presentation of unaligned pre-ExM (green) and post-ExM (red) data. **ii)** Initial manual registration using similarity alignment. **iii)** Aligned data after automatic block-matching algorithm with similarity. **C)** Representative images showing alignment changes between manual and automatic. **Scale Bar: A/B:** 2 µm (all pre-expansion scaled)

5.2.3. Expansion Factor Calculations and Comparison

As addressed in the methods section (section 2.6.4.), calculating the expansion factor of the local region was obtained from the transformation matrix. The 3x3 matrix representative of the 3D transformations connecting the pre- and post-ExM images provide an overall expansion factor, assuming an isotropic expansion.

The global expansion factor was calculated for two experimental datasets: RPE-1 cells stained with NUP98, and RPE-1 cells stained with both NUP98 and ATP5A1. The single stain NUP98 showed an expansion factor of 3.96 ± 0.04, wherein 5 pre-/post-ExM data points were collected from 4 cells within the region (Figure 5-4).

The dual-stained datasets showed a NUP98 expansion factor of 2.85 ± 0.32, and a ATP5A1 expansion factor of 3.21 ± 0.27. This was taken from data collected across 2 wells observing 3 independent regions for 4 sets of paired data points. NUP98 and ATP5A1 data points were taken simultaneously to allow for comparison in the same local region (Figure 5-4). The difference in expansion factor between the NUP98 and ATP5A1 datasets is likely due to drift effects across the image. As the NUP98 data is primarily central to the image, these effects are mitigated compared to the ATP5A1 data which is more global in presentation. This was minimised by reducing the exposure time, however, it is clear in the more stretched appearance of the ATP5A1 data that this drift was not even between planes.

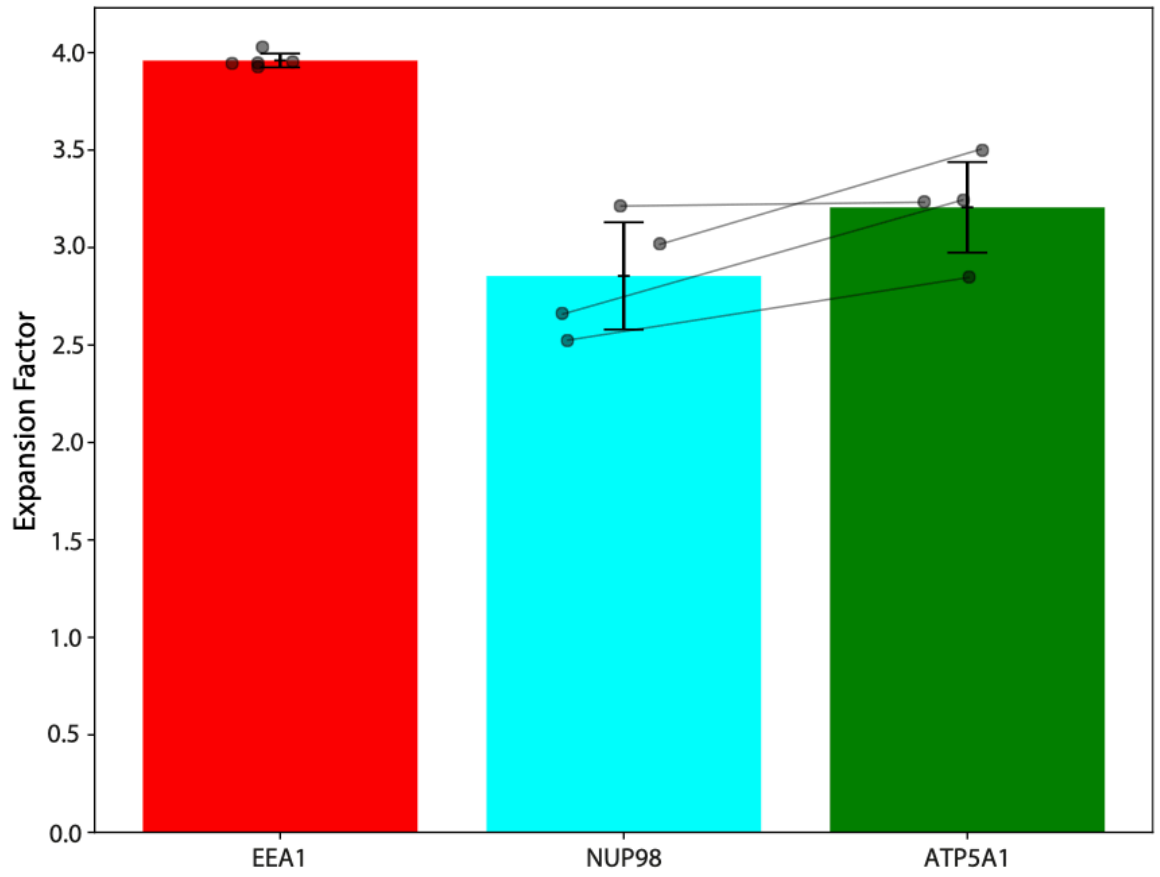

Figure 5-4: Bar graph of expansion factors as calculated by the transformation matrix

Mean expansion factor with error bars denoting standard deviation. Single fluorophore EEA1 with 3.96 ± 0.04 EF from 5 paired datasets. Dual fluorophore NUP98 and ATP5A1 with 2.85 ± 0.32 and 3.21 ± 0.27 EF respectively from 4 sets of paired datasets.

5.3. 3D Distortion Analysis:

5.3.1. Validation of Farneback Optical Flow 2D Approach in 3D ExM

As per 2D distortion analysis, Farneback's optical flow algorithm (Farnebäck, 2003) was used to assess distortions. To incorporate 3D data, the algorithm was applied to the comparative 2D XY and XZ planes of the image sets to compile the distortion data. Comparisons of the distortion data of the shared axis from XY and XZ were used to validate the process. The absolute sum of the shared X axis distortion data was the same between the two planes.

5.3.2. Application of 3D Distortion Mapping with Comparative 2D Regions

Using this approach, the distortion vectors were used alongside the pre-/post-ExM image data to produce visualisations of the distortions present. This 3D visualisation is a representation of the 3D surface render of the data. By limiting the vector amount visualised the distortions were observable.

The qualitative observability of distortions arises from both the difference in pre- and post-ExM overlays, and the magnitude of the local distortion vectors. The distortion vectors were colour coded and scaled by the magnitude of the data. (Figure 5-5)

By observing the 2D distortion map, distortions within the presented slice are apparent. Comparatively the 3D distortion map presents this data in context to structures above and below in the plane. The 2D distortion map appears less

heterogeneous than the 3D distortion map and this is predominantly due to the large region imaged and the nature of the fluorophores used here. The NUP98 fluorescence pattern is regular throughout the membrane of the nucleus and the dense pattern shows clearly the visual obstruction that can occur.

In less densely arranged structures, such as endosomes, the advantages of 3D distortion mapping become clearer. Here we can see the pre-/post-expansion images and the clear trend of the distortion in the local region (Figure 5-6).

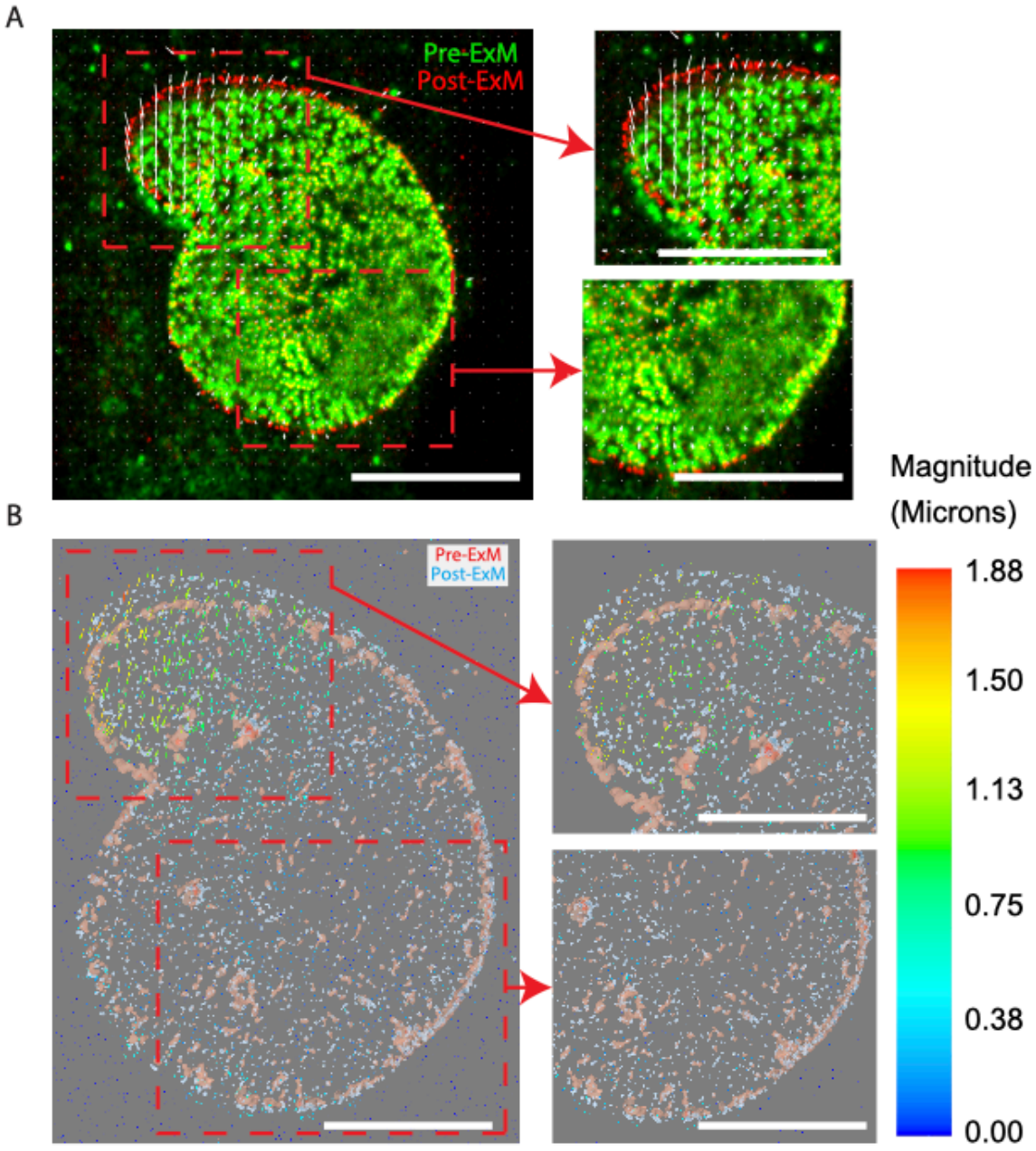

Figure 5-5: 2D distortion map with comparative 3D viewpoint of an RPE-1 cell nucleus stained with NUP98

Staining and distortion maps show large distortion to the top of the image in line with the visual distortion present **A)** 2D distortion map with sections illustrating high and low distortion. **B)** 3D distortion map in the same plane wherein the size and colour intensity of the distortion vectors illustrate high and low regions of distortion. Scale bar: 2 μm (all pre-expansion scaled)

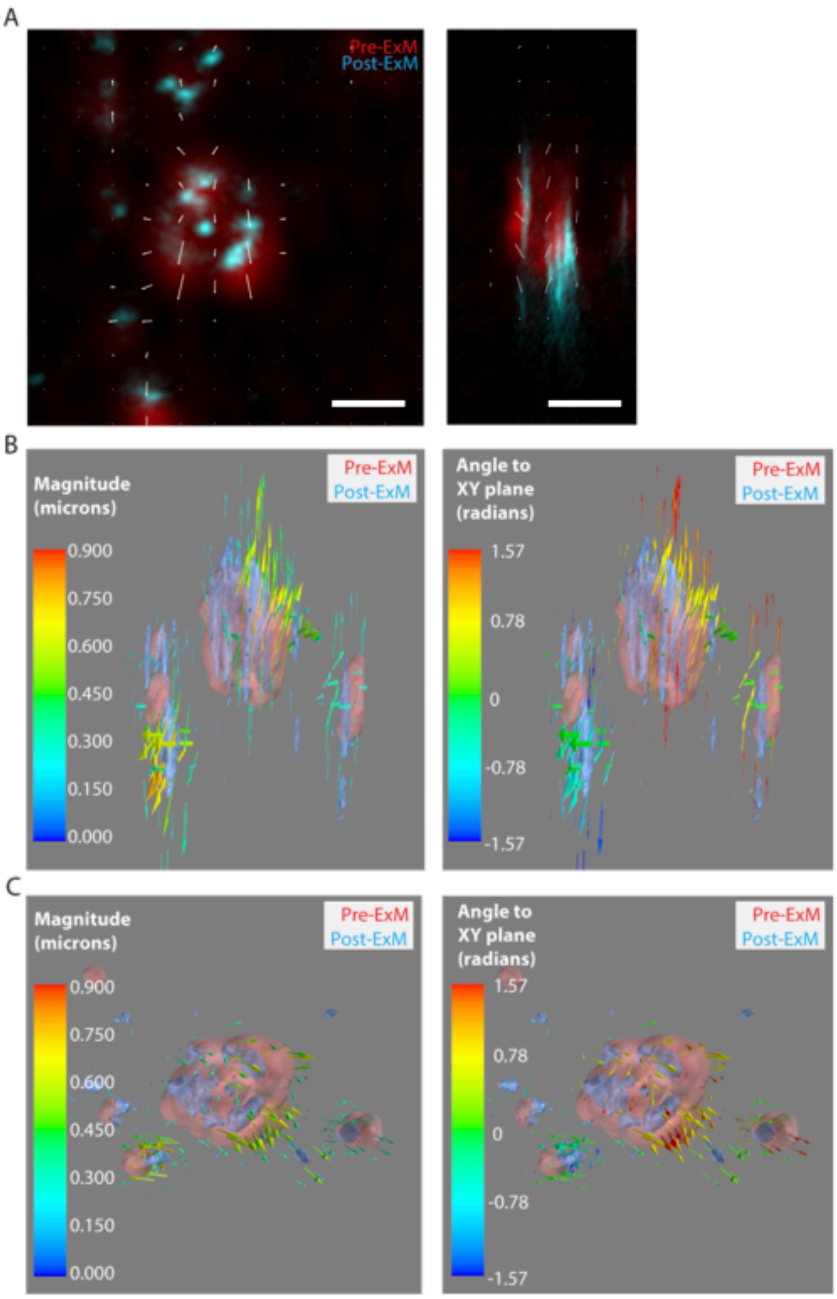

Figure 5-6: 2D distortion map with comparative 3D viewpoint of an endosome within an EEA-1 fluorophore stained RPE-1 cell

A) 2D XY and XZ distortion map slices from the centre of the Z-stack. **B)** 3D XY full volume distortion maps illustrating the magnitude of distortion and the angle of the distortions relative to the XY plane. C) 3D XZ full volume distortion maps illustrating the magnitude of distortion and the angle of the distortions relative to the XY plane. **Scale Bar:** 500 nm (pre-expansion scaled)

5.3.3. RMSE as a Function of Length Measurement Calculations for 3D Distortion Data

To quantify the impact of 3D distortion vector information on the overall error in the post-ExM images, the RMSE code required further development. In particular, the 2D RMSE code uses a list of coordinates as its input. These are subsequently processed using linear algebra to acquire the distance measurements required to calculate the RMSE. This list of coordinates contains only X and Y values.

The numpy.linalg.norm (Harris et al., 2020) function performed at order = 2 is equivalent to the Euclidean distance. Therefore, adapting the code to process the 3D data, required amending the list of coordinates to contain the coordinates for all 3 axes.

Applying the code, within the NUP98 dataset the greatest error is seen near the top of the image wherein the upper lobe of the nucleus contains more distortion than the lower lobe. This is visible in the RMSE data with an initial peak at low length scales (<5 microns), indicative of the many points that are nearby to one another but locally distorted. This is also visible in a second peak at the ~15-micron length scale wherein the far border of the nucleus accumulates the error in distance from the distorted region (Figure 5-7). The error at these scales is ~ 25% at low length scales of <1 micron, and ~2% at the second peak. This indicates that there is notable distortion in the position of the nuclear pores between pre- and post-expansion. A finding otherwise masked by the larger visible distortion in the image.

Applying this to the previous endosome data we can perceive that the RMSE is large at this scale. Classically, ExM expects an error of 1-3%, here we can see that at the 3-micron length scale the error is ~0.75 microns. This results in an RMSE of ~25% at this scale (Figure 5-8).

The notably larger error at the smaller length scales differs from that of 2D ExM RMSE. This is likely the influence of error in the Z axis where the pixel size is four times larger than the XY plane. Therefore, a single pixel of misalignment would be significantly scaled as an error in the RMSE analysis. Combined with any degree of single axis anisotropy, this would appear as an overall shift in the data.

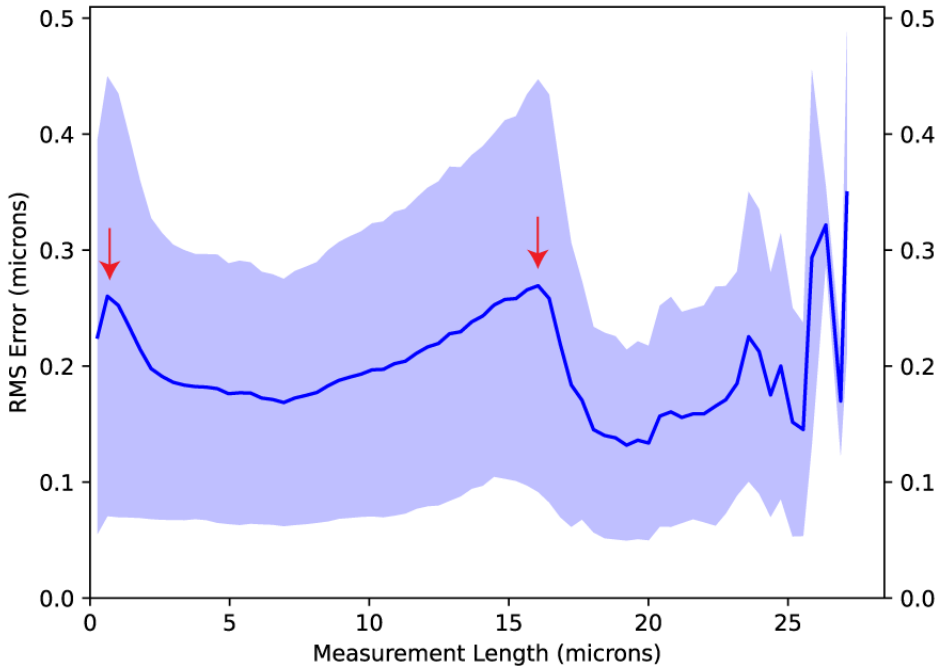

Figure 5-7: RMSE as a function of length measurement in XYZ for an RPE-1 cell nucleus immunostained with NUP98

Blue line indicates the RMSE, shading indicates the standard deviation. The first and second peaks are highlighted (red arrows) for their structural relevance.

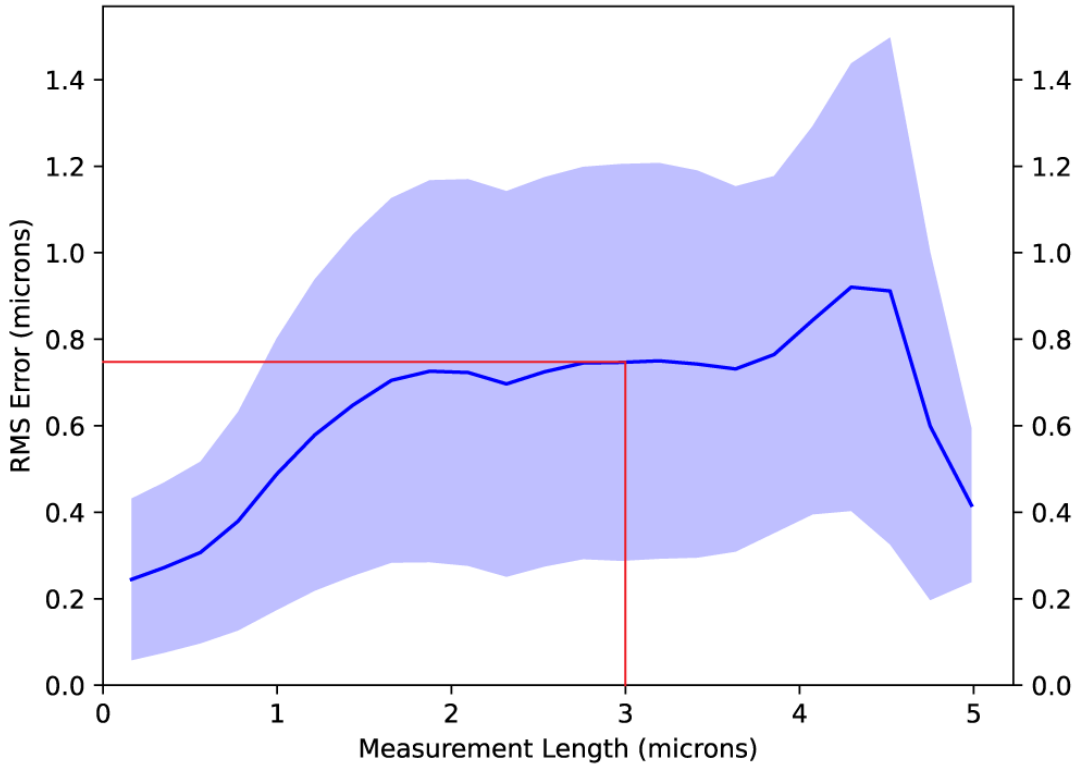

Figure 5-8: RMSE as a function of length measurement in XYZ for a single endosome

Blue line indicates the RMSE, shading indicates the standard deviation. The error at a structurally significant scale of 3 microns is illustrated with the red markers.

5.3.4. Plane-Dependent Comparison for RMSE as a Function of length Measurement for 3D Distortion Data

Due to the difference in sectioning between lateral and axial planes, it was deemed prudent to separate the components of RMSE based upon their relative planes. Using the increased flexibility of the algorithm the relevant axes were selected to compare the magnitude of the error in each plane. Thereby allowing the collection and production of RMSE graphs for XYZ, XY, XZ and YZ planes.

The RPE-1 cell nucleus immunostained with NUP98 shows a similar profile in the RMSE profile between the volume and the individual planes. The RMSE in each plane illustrates a larger error in the YZ plane. This is likely correlated with the distortion having a visibly larger Y axis component resulting in the RMSE showing greater peaks (Figure 5-9). Comparatively, the visible error in the X axis is low hence the overall lower RMSE in the XZ plane.

Interestingly the XY RMSE aligns with the XYZ RMSE at values >6 microns. This is likely due to the noted distortion in the position of NPCs at these scales. Alongside this, at length scales of <5 microns, the error the RMSE of the XZ and YZ data is notably larger than XY, likely due to the axial alignment and difference in pixel size.

Comparatively, the RPE-1 endosome immunostained with EEA1 antibody shows reduced RMSE in the XY plane. As this is a smaller image volume, the alignment can more accurately register the axis with greater information present. In this case the greater resolution inherent to the XY plane allows for more accurate registration in this plane. Without the need for additional structures to balance the registration against the singular endosome is prioritised. As per the distortion map visualisation the error is expectedly greater in the XZ and YZ planes (Figure 5-10).

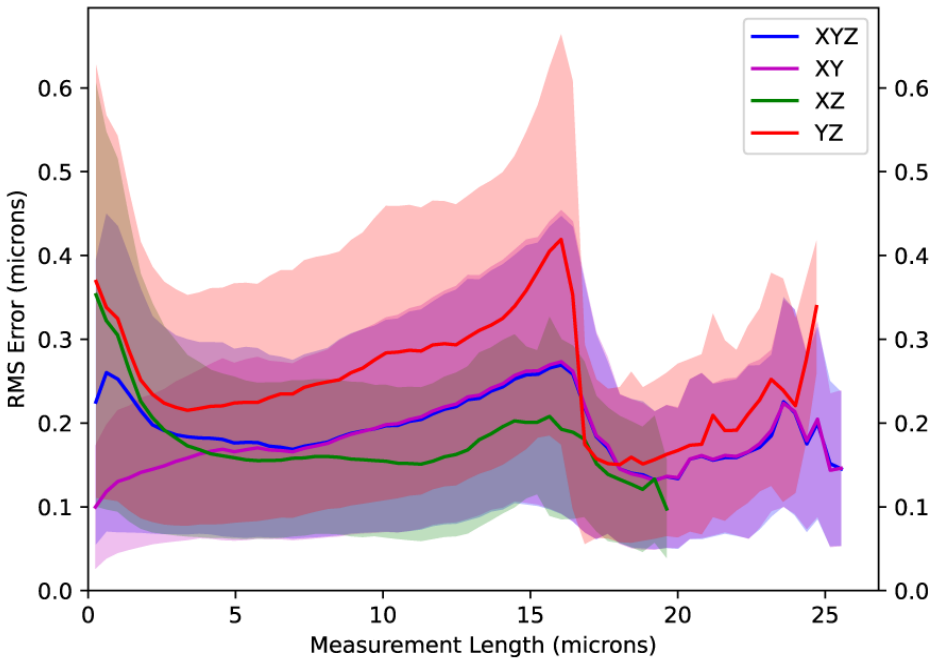

Figure 5-9: RMSE as a function of length measurement in XYZ (blue), XY (magenta), XZ (green) and YZ (red) planes for an RPE-1 cell nucleus immunostained with NUP98

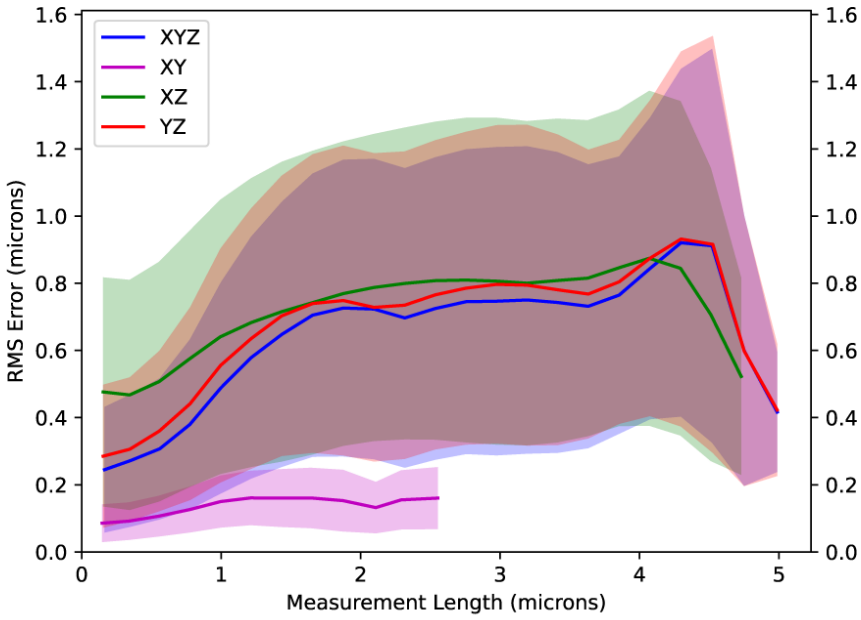

Figure 5-10: RMSE as a function of length measurement in XYZ (blue), XY (magenta), XZ (green) and YZ (red) planes for an RPE-1 cell endosome immunostained with EEA1

5.4. Applying 3D ExM to Drosophila Flywing 3D Data

5.4.1. Distortion Analysis and 3D Visualisation

Revisiting the flywing data from chapter 4, the 3D dataset was passed through the analysis pipeline. The 2D data representations show distortion distal to the centre of the image, with notable shift in the upper left quadrant (Figure 5-11). Conversely the 3D data shows the post-ExM information being within the 3D space of the pre-ExM structures. The distortion vectors are significantly more in the Z plane as per panel B in the figure. This indicates that to optimally align the data a degree of Z variance was included and unable to be fully accounted for.

This would be suggestive of non-uniform distortion of the sample, in particular, the lower right quadrant of the data appears to be shifted between the pre-and post-ExM images. This may be due to incomplete digestion, or a magnified tilt of the sample when being suspended in the hydrogel. Therein resulting in the sample not being as homogenous in the Z axis post-ExM relative to pre-ExM.

Identification of these factors could highlight methodologies to increase the robustness of tissue based ExM experiments.

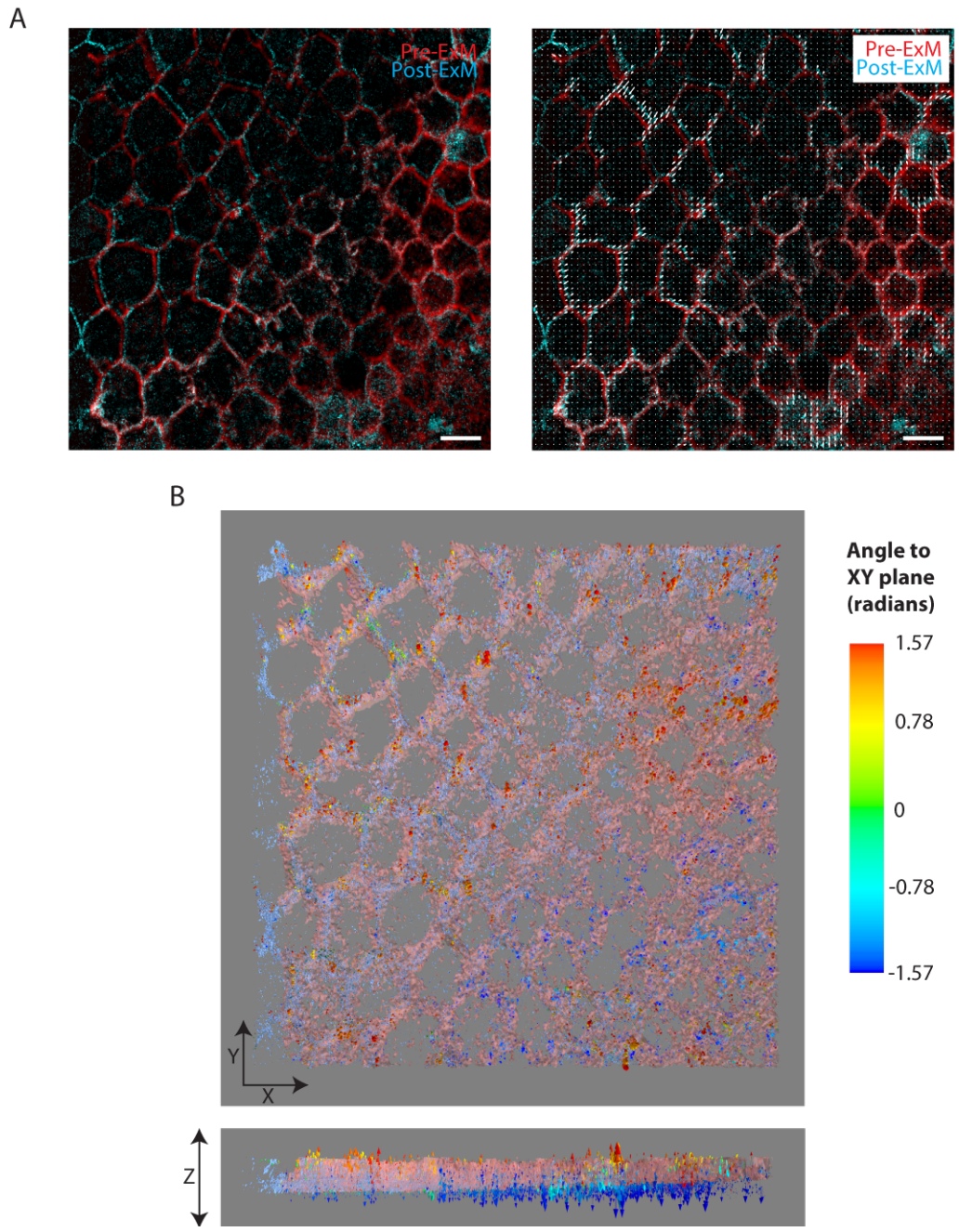

Figure 5-11: 2D distortion map with comparative 3D viewpoint of *Drosophila* flywing data with endogenous cadherin

A) 2D XY and XZ distortion map slices from the centre of the Z-stack. **B)** 3D XY full volume distortion maps illustrating the magnitude of distortion and the angle of the distortions relative to the XY plane. **C)** 3D XZ full volume distortion maps illustrating the magnitude of distortion and the angle of the distortions relative to the XY plane. **Scale bar:** 10 microns.

5.4.2. RMSE Analysis Across Three Dimensions

Comparison of the RMSE shows similar consistency between the 3 planes and volume (Figure 5-12). The XZ and YZ planes show greater distortion than the XY and XYZ. With a divergence at ~30 microns measurement length. This is related to the greatest distances in the sample. Therefore, is likely due to the offset between pre-/post-ExM in the upper left quadrant and the Z shift predominant in the lower right quadrant of the data (Figure 5-11).

This correlates with a peak at these greater length scales (~50 microns) in the XY and XYZ RMSE. Particularly as such length scales would comprise the largest diagonal of their representative plane.

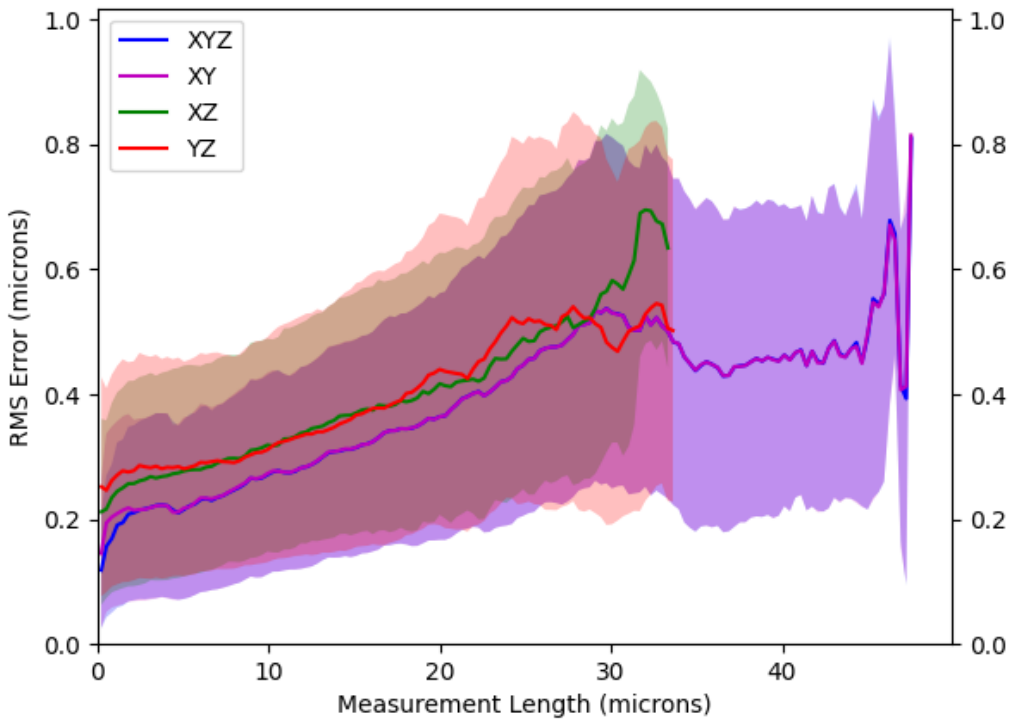

Figure 5-12: RMSE as a function of length measurement in XYZ (blue), XY (magenta), XZ (green) and YZ (red) planes for a *Drosophila* flywing sample stained with endogenous cadherin

5.5. Comparing Expansion Factor Axially versus Laterally

5.5.1. Variance between XY and Z Expansion Factor Qualitatively

Whilst performing alignment, it was noted that structures further from the aligned plane were moving significantly out of alignment. This was consistent across the dataset. Commonly, this was seen as the post-expansion dataset having a perceived greater expansion in the Z axis than the X and Y axis.

Figure 5-13 illustrates an example of this case. RPE-1 cells were immunostained with EEA1, for identifying early-stage endosomes. The alignment was performed with preference to regions near the coverslip, as mentioned previously. However, the post-ExM endosome is notably out of alignment with its pre-EXM counterpart.

Structurally, the post-ExM endosome appears stretched in the Z axis, giving the appearance of being larger than the pre-ExM counterpart. The same structure post-ExM, when viewed from in the XY plane, appears smaller and translated relative to its counterpart.

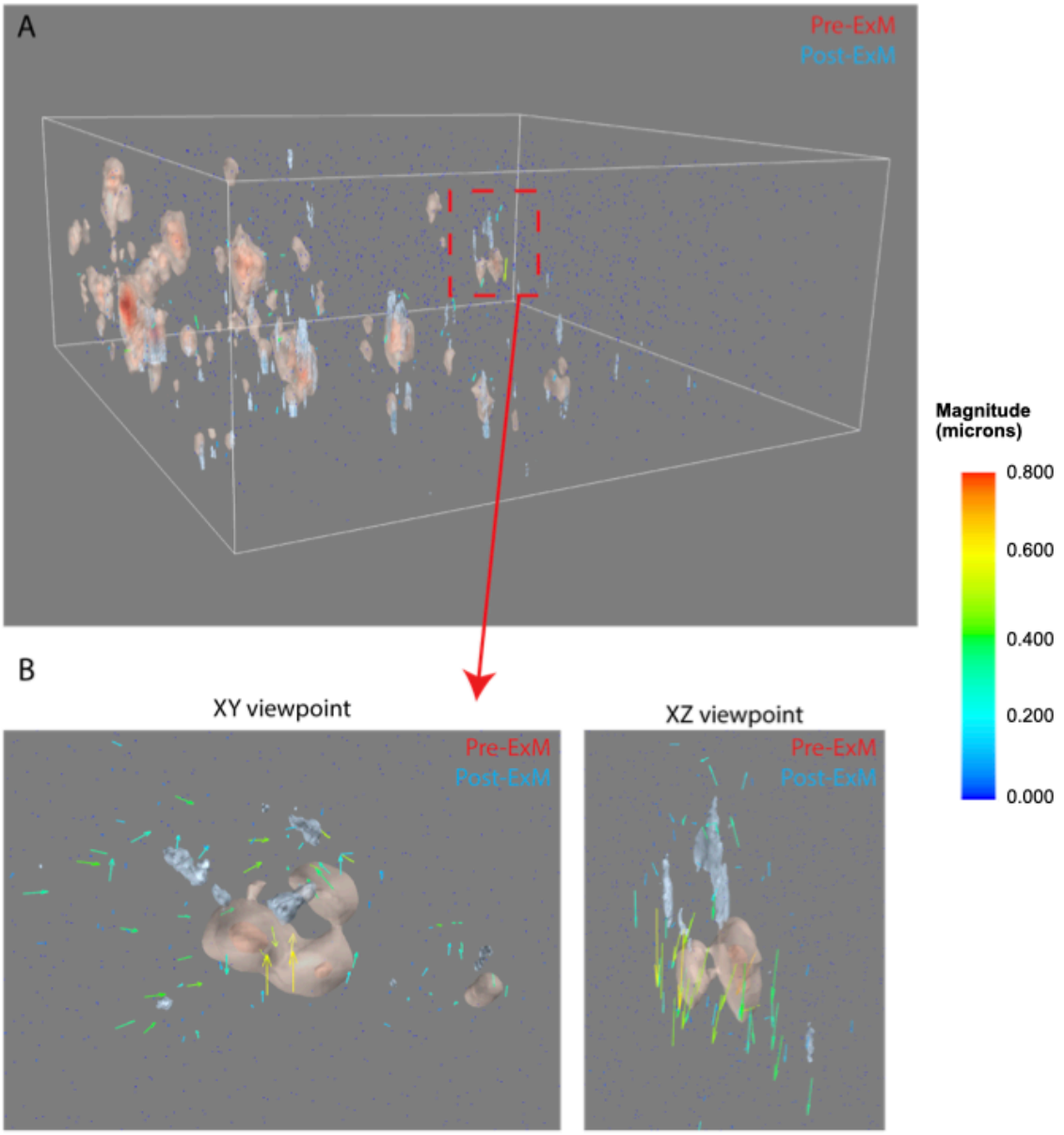

Figure 5-13: Distortion map of RPE-1 cell immunostained with EEA1 identifying endosomes

Pre-ExM (Red) and post-ExM (blue) data with distortion vectors superimposed. A) Full volume image of aligned dataset. B) Singular endosome from XY and XZ viewpoints.

5.5.2. Measuring Difference in EF in X, Y and Z Quantitatively

To investigate this quantitatively we compared the size of the same endosomes between pre- and post-expansion.

In the lateral plane, the area of the endosome was calculated and in the axial plane the FWHM of the largest section of the endosome was calculated. This was compared with data from the same region in post-expansion. The EF was calculated by dividing the pre- and post-expansion values by one another and averaging the results.

The lateral expansion of 3.43x, compared to the axial expansion of 5.60x, showed an increase in the EF in the axial plane compared to the lateral plane (n=7) (Figure 5-14). When compared to the average EF of the image data the endosomes were collected to of 4.01x (5 paired pre-/post-expansion datasets) we can see local contraction in the lateral plane and local expansion in the axial plane.

As this data contains paired observations from the same sample and we can assume the distribution should be normal, a paired t-test was performed resulting in a $p=0.014$, showing statistical significance.

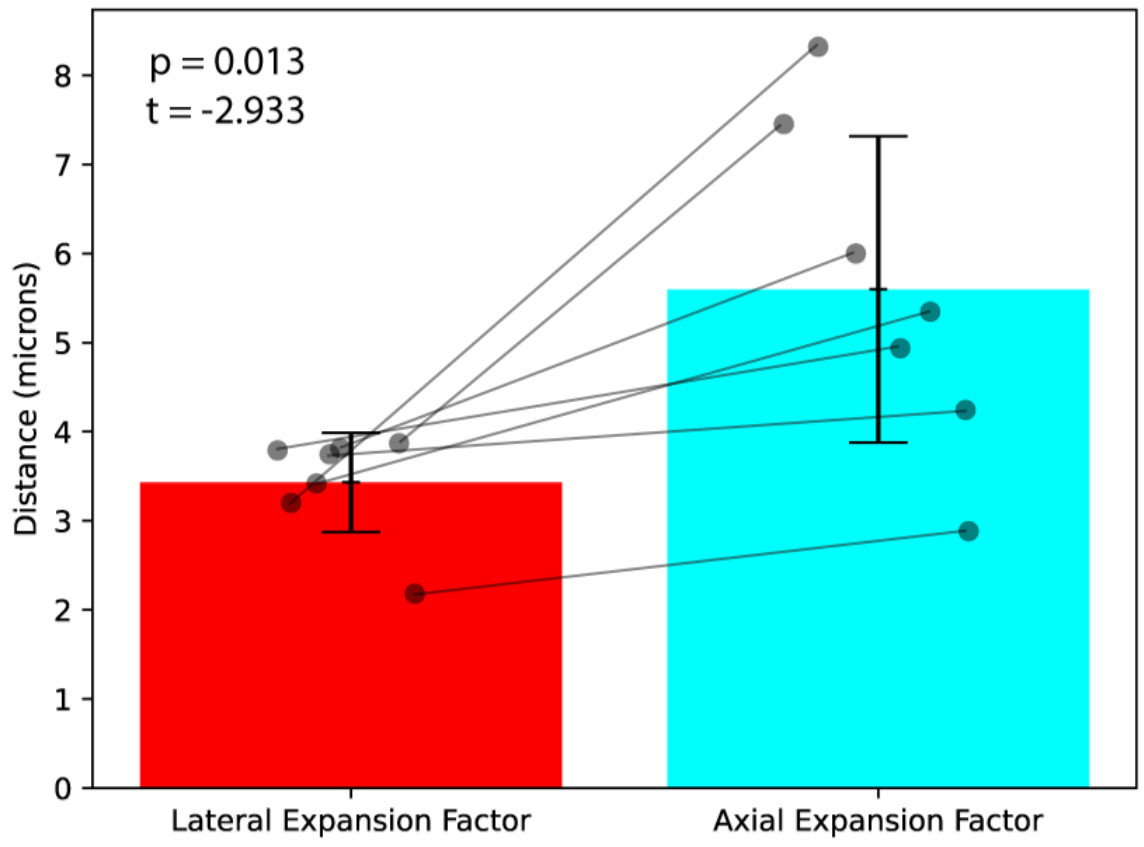

Figure 5-14: Bar chart with error bars showing the lateral and axial expansion factors

The lateral expansion factor has a mean of 3.43, the axial expansion factor has a mean of 5.60 (n=7)

5.6. Discussion

5.6.1. Expanding the Analysis Pipeline to 3D ExM

ExM has allowed the acquisition of high-resolution data without the need for specialised equipment. With the abundance of hydrogel recipes (U-ExM (Gambarotto et al., 2019), TREx (Damstra et al., 2022), x10 ExM), there are myriad ways to investigate a biological question.

Developing ExM by using the full three-dimensional information available allows a unique opportunity to leverage these advantages to gain a better understanding of the cellular ultrastructure in an additional dimension. Validation methodology has been key to ensuring data is appropriately interpreted, with each innovation in the ExM technique using a similar structure (Chen et al., 2015; Damstra et al., 2022; Gambarotto et al., 2019). The use of pre-/post-ExM images to identify distortions and compute the RMSE have been used to assess this robustness as discussed in Chapter 4. Therefore, the 3D ExM pipeline developed here emulates this model.

Registration of pre- and post-ExM images is vital to the analysis process. However, as we are now dealing with volumes instead of 2D images, the data needs to be treated as such. Landmark-based registration algorithms allow for manual alignment but in 3D data this works better as an approximation. This is due to the additional axis of data providing an additional level of uncertainty to a human user when attempting to align the images.

Comparatively, SIFT-based alignment methods perform automated frame-to-frame matching within the stack. Due to the expansion of the sample resulting in a greater

number of frames to cover the same region between pre- and post-ExM, data would need to be prepared to make an equivalent frame count between the image sets. This process would be limited by the lack of knowledge of the local expansion factor between the image pair. Estimations of the EF may assist this process but ultimately these would be qualitatively biased.

Advanced registration and image processing programs such as BigStitcher(Hörl et al., 2019) provide automated processes with both pairwise matching (landmark) and global point assignment based methods. These primarily focus on aligning adjacent image data and using the tools to correct for the deviations between the samples. Additionally, several of the alignment processes including iterative closest point (ICP) (Besl and McKay, 1992) or random sample consensus (Fischler and Bolles, 1981) use non-rigid methods to compensate for aberrations. Under the base assumption of isotropy, non-rigid methods for registration would inherently contradict this process and the subsequent computation of distortion vectors.

Hence, image data must be considered as volumes and registration should be volume-to-volume. Additionally, an automated rigid process is preferable to reduce additional bias. The Fijiyama plugin (Fernandez and Moisy, 2021) has allowed this process via its block-matching alignment algorithm. By considering the voxels in the local region and finding best fit locations, under the constraints of a similarity match, the overall volume can be transformed providing subpixel adjustment based on the registration information of all blocks that are matched.

Robust registration methods are the underpinning of the subsequent steps of visualisation and error quantification. A poorly aligned image will lead to inaccuracy in the error calculations as the data will be translated by the margin of misalignment. Therefore, the development of a bespoke pre-/post-ExM registration software that can cater for the base assumptions made would be an invaluable tool for the future of the technique.

Moving forward to the distortion map, visualising the data is crucial. A qualitative way to examine the usability of an imageset allows for swift decision making regarding the degree of distortion present in the data and the likely reliability of subsequent quantification. If distortions are visually significant, a dataset can thus be discarded prior to further quantitative analysis. Understanding the 3D distortions adds a layer of visual complexity to the data which is more easily seen in 2D data distortion mapping.

To combat this, the initial conception of a 3D model as generated through the Mayavi (Ramachandran and Varoquaux, 2011) module in Python, provides a starting point for future development. Other modelling software (i.e. Blender (Foundation, 2018), Napari (Chiu et al., 2022)) could also take the registered image data and display them. To then combine this with distortion vectors provides an interactive 3D model for researchers to determine the reliability of their data.

However, this method of distortion visualisation would be difficult to portray on paper. Modern journal articles are taking advantage of data repositories to show additional media as supplementary videos and other similar formats. Thereby, distinct slices of

3D distortion maps could be shown in the immediate literature to illustrate the key regions of alignment, with the full 3D distortion map viewable in accessible modelling or visualisation software.

Labelling density has an impact on the clarity of the 3D distortion maps. As illustrated in figures 5-5 and 5-6 the denser the structure in an area the more difficult for 3D visualisation to show the smaller scale distortions. In the case of the NUP98 dataset, the macroscopic distortions are equally visible in both the 2D and 3D distortion data. As the 3D visualisation is interactive the capacity to explore the structures allows for exploration of the 3D landscape, in contrast to the 2D distortion map slices. This could be effectively communicated through 3D model data as a supplement to 3D ExM data.

Multiplanar view of the data, as in figure 5-6, with smaller structures having less obstruction, is a more likely usage case in the pursuit of ultrastructure investigation. Here the 2D data provides visual access to the centre of the structure that would be obstructed by 3D information. The 3D data in turn shows the clear visual increase in resolution of the structures. In addition, regions that are effectively aligned are clear to identify from the lack of distortion vectors in the vicinity.

Using both 2D and 3D representations of the data to portray examples of well aligned and poorly aligned regions, would further allow for transparency and foster a greater understanding of the uses of ExM.

Error quantification provides the numerical understanding to the data thus obtained. RMSE as a function of length measurement has been used to determine the error across the scale of the image and thereby highlight regions where error is prominent.

As the linear distance between two points is calculated with trigonometry irrespective of plane, when adapting to 3D, we can continue to use trigonometry. This allows us to contextualise the data in 3D space by comparing the 3D RMSE alongside the RMSE of each 2D plane. These split RMSEs then allow equivalent comparison which can further highlight the presence and scale of errors.

5.6.2. Variation in Expansion Factor between Axes

The presence of an anisotropic expansion factor independently in the axial direction is an unexpected finding. Several labs globally have mentioned seeing similar effects, with the cause remaining unknown. Several factors could be the cause for this including: sample drift in z, optical aberration, and genuine gel-based distortion.

Sample drift had been addressed through drift correction algorithms such as “Linear Stack Alignment with SIFT” (Lowe, 2004) and Turboreg (Thevenaz et al., 1998). However, it remains plausible that a persistent drift independent of the sample, but related to the hydrogel stability, is possibly resulting in the elongation in Z.

This could occur due to the top surface of the gel having a greater surface area exposed. The greater surface area would facilitate the evaporation of water near the top of the hydrogel. In turn resulting in a perceived drift as the hydrogel shrinks near

the upper surface and distorts the area below. This would only partially explain the effects seen as it would be expected that the XY expansion factor would decrease further up into the sample.

Optical aberration would conversely be more likely to produce further defocus and perceived expansion further into the sample within the XY plane. Hence this explanation is unlikely.

In regards to gel based distortion, it is known that structures like nuclei do not expand proportional to the expected gel expansion factor (Büttner et al., 2021; Pernal et al., 2020). Typically this results in a reduced expansion of these structures as further investigated in a recent preprint by Norman et al. (2024) (Norman et al., 2024). The preprint shows preliminary evidence that the concentration of Acryloyl-X is responsible for the anisotropy found here. With lower concentrations yielding better expansion of nuclei. This is deemed to be due to excessive linking of chromatin by Acroloyl-X reducing the capacity of the nucleus to expand.

Whilst this would explain a reduction in expansion factor, it is unlikely to explain the increase seen in the axial expansion factor. Further investigation into ExM gel recipes and additional underlying factors is warranted.

5.7. Concluding Remarks

The 3D spatial separation of fluorophores offered by expansion microscopy is an opportunity to further develop and increase the applicability of the technique. As expansion can be combined with super-resolution techniques, the resolution improvements and structural insight provided could open new doors of exploration for researchers.

With the pipeline presented here, the foundation and initial standard for data analysis in this advancement are set to maintain the robust, and integral validation used currently in the ExM community.

In addition to biological application, development of novel gel recipes may play an important role. For example, the knowledge of cellular compartments having different expansion rates is a known caveat of the technique thus far. However, preliminary work broaching 3D ExM has shown that this may be related to acryloyl-X concentration causing excessive crosslinking at dense regions. Reduction of the acryloyl-X or replacement with glutaraldehyde was found to reduce and eliminate distortions caused by this process (Norman et al., 2024). Thus, adjustment to the classical gel recipes can be explored to ensure minimal anisotropy in all 3 axes.

Overall, validation of novel advancements is necessary in cementing a new technique amongst users. Classical ExM allows for high resolution insight within biological research. Advancing the technique to 3D ExM maintains the accessibility, whilst opening the technique to further biological application and research.

Chapter 6. General Discussion

6.1. Application of a Plate-Based Approach to ExM

Expansion microscopy has evolved from its initial inception, with frequent breakthroughs and developments allowing for new insights and applications in scientific research. A core ideology of the technique has been to allow for accessibility and democratization of high-resolution microscopy; a plate-based approach was designed with this philosophy in mind.

The traditional approach to expansion microscopy involves several delicate stages, particularly gel handling and transference, which can introduce errors and reduce reproducibility. Minimizing risks at these stages, especially manual handling, helps clarify the impact of other factors, such as incomplete digestion or mechanical tears, on sample quality (Asano et al., 2018). Reducing manual handling also allows for better optimization of digestion steps within the classical framework. Adopting a more standardised technique could enhance reproducibility in the field of ExM.

The microplate allows for continued use of straightforward protocols, whilst reducing gel handling and variability. Regulating these factors alone results in more consistent gel formation and higher throughput, which are primarily limited by the available imaging time. Whilst currently limited to 4x expansion recipes, this approach has demonstrated compatibility with both cultured cells and tissue samples. By sharing the footprint of a 6-well plate, the microplate remains compatible with other tools useful for scientific investigation.

Comparatively, the recent 96-well plate approach, HiExM, of Day et al. (2024) (Day et al., 2024) shows four-fold expansion of cultured cells, using an automated platform. The current inception of HiExM has a hard limit of four-fold expansion, limited by the well capacity and stability of the small gel sizes. Whilst this technique has a demonstrable increase in throughput, the requirement of a dedicated fluid-handling device to automate the process reduces the accessibility of the technique. Combined with the current limitation of being only compatible with cultured cells, and the additional complexity introduced through multiple nitrogen purgings and UV irradiation, this results in HiExM's current applications being limited.

HiExM as a technique is a clear future development for the ExM field and will likely play a key role as the technique develops. However, ExM requires further development to truly make use of large-scale automation. In particular, building further trust in the technique through robust gel recipes which maximise isotropy and minimise distortions.

In comparison, the microplate approach is a natural next step in the development of ExM. Transforming the slide bound traditional approach to a more standardised system able to be applied in a more simplistic manner. The overall method remains similar; however, the steps of the technique are made more accessible. Thereby, retaining the core philosophy of ExM and allowing for easier access and use of the technique.

Further developments in automation would allow for clinical application using ExPath (Zhao et al., 2017) related recipes for histopathology and biopsy related insight. The use of plate-based approaches would be critical to such developments and present an opportunity of increased application and development of ExM beyond the research field. This remains predicated on validation of ExM methods with common histology samples to assess for distortions.

6.2. The Role of Pre-/Post-ExM Image Analysis

To increase the reliability and robustness of ExM, the integration of pre- and post-ExM image analysis is essential for long-term validation and the complexity of the technique. A persistent challenge in ExM is the presence of distortions, which can complicate consistent identification through pre- and post-ExM imaging. This task remains both time-consuming and technically demanding.

As outlined in Chapter 1.7.4., 41.6% of journal articles between 2015 to 2023 report pre-/post-ExM data, although few continue to calculate the RMSE as a function of length measurement. This is likely due to a growing confidence in ExM and the inherent difficulties in pre-/post-ExM image acquisition. Bridging this gap remains a critical focus for future advancements in the field.

The microplate approach developed in this thesis aims to address the challenges associated with pre-/post-ExM image acquisition. The coordinate mapping method described in Chapter 3 is adaptable to other ExM modalities beyond the microplate format. For instance, in the traditional ExM approach, regions imaged on the coverslip before ExM could be mapped to corresponding location within the

expanded gel by extrapolating relative coordinate positions. This allows approximate location within the expanded gel to be identified prior to cutting the gel for imaging.

The complexity of both qualitative and quantitative image analysis methods in ExM has hindered consistent and reliable reporting. To alleviate this, the code developed here seeks to simplify the process whilst maintaining accessibility. Specifically, RMSE analysis can be computationally taxing for larger datasets due to the requirements of the analysis method. Briefly, RMSE code requires measuring the distance between a coordinate point and all other points in the image for all points. These values are subtracted from the equivalent points in the image pair to calculate the error. Thereby, in avoiding repeating coordinate pairs, the mathematical lower triangle of this coordinate array is requisite to the computation.

Currently available code is designed for smaller datasets of 200-500 pixels per lateral dimension (Chen et al., 2015; Truckenbrodt et al., 2019). However, as the image size increases the amount of data to be processed can easily exceed the capacity of the computer. For example, for a 500x500x20 pixel dataset, the total data to be calculated for the RMSE exceeds 10^13 which is on the Terabyte scale. Due to the structure of Python data, this would require the data being contained in both RAM and hard drive space, easily overwhelming a non-specialist device. Cloud approaches could provide an accessible alternative outside a dedicated computing environment; however, security of data and time constraints remain prevalent.

The change in approach to sequential calculations of RMSE described in Chapter 3, aims to improve accessibility by tackling this problem. In summary, instead of

tackling the entirety of the data simultaneously, the information to be processed is sequentially calculated by each point against all other points. By avoiding repeating point pairs, the list of coordinates to process decreases with each iteration, resulting in all points being processed in a format that is overall smaller to handle comparatively. This reduced load requirement should allow a less powerful system to handle RMSE analysis without dedicating excessive computational power to the process. This remains limited by the size of the dataset however, as larger datasets could quickly scale beyond the capacity of this approach, following a square law.

To facilitate this approach, based on the concept that distortions will be relevant and prominent near fluorescent structures, the code allows for selection of a subset of the data. This subset is based upon a fluorescence threshold calculated by the number of points selected to be processed allowing for more focused analysis whilst eliminating structure free areas. By adjusting the point amount, this approach allows for quick preliminary error analysis as well as the full image RMSE analysis as required. In application, this can allow researchers to get an understanding of the errors present prior to a full analysis which will take a greater amount of time.

6.3. Limitations in ExM

While ExM allows researchers to further investigate structures below the diffraction limit, the current barriers of gel fragility, distortions, and accessibility for new users, continue to hinder its widespread adoption and effectiveness.

ExM gels, despite advancements in formulation, broadly remain fragile. When compounded by the challenges of manual handling, the technique demands a high

level of skill and attention to detail for consistent results. Recent additions, such as TREx (Damstra et al., 2022) and tetra-gel (Gao et al., 2021; Lee et al., 2021), have addressed gel fragility by introducing more robust and deformation-resistant hydrogel recipes. However, the need for careful manual handling remains a limitation.

The microplate approach, which eliminates manual gel handling, largely circumvents the fragility of hydrogels by containing the gel within a closed system. The method is currently effective with four-fold expanding samples. However, the broader use of larger expansion recipes (U-ExM (Alonso, 2022), X10 ExM (Truckenbrodt et al., 2018) and TREx (Damstra et al., 2022)) are an important part of the ExM field. To adapt the microplate approach to these larger expansion protocols, two strategies can be employed: increasing the well size or reducing the gelation chamber's dimensions. Enlarging the well size would reduce the number of wells per microplate and necessitate custom coverslips. However, since the CAD models for the plates are open-source, they could be modified to accommodate protocols requiring ten-fold expansion.

Alternatively, reducing the size of the gelation chamber could allow for smaller, more robust gels suitable for larger expansion factors. This approach is limited by the ability of the silicone frames to produce sufficiently large, distinct gels while maintaining structural integrity. Combining both strategies, reducing the gel size from 5x5mm to 3x3mm and increasing well size from 20x20mm to 30x30mm, could potentially allow for ten-fold expansion by allowing for a ten-fold expandable space and a gel that could still be formed.

An alternative approach involves developing an outer frame structure that could be mounted in a petri dish or a standard 6-well plate. This would enable the larger geometries required for ten-fold expansion, while an inner frame could maintain the geometric approach developed in Chapter 4.

The presence of artefacts as a result of the reliance on digestion and denaturation approaches, and the flexible and heterogeneous nature of hydrogels, has led to the importance of characterisation and documentation of distortions (Truckenbrodt et al., 2019). Detectable artefacts, including shearing and fracturing, are clearly identified in the post-expansion image alone. However, quantitative approaches can reveal artefacts not readily observable by eye, particularly those affecting subcellular regions, where local warping and tilting can distort the spatial size of structures.

Pre-/post-ExM images registration, along with quantification, would allow these distortions to be contextualised relative to the original data, enhancing the reliability of the expansion process. However, performing these steps for every sample is considerably time consuming and labour intensive.

By constraining the approach to a single microplate, this approach can be simplified using the coordinate system to perform simpler pre-/post-ExM imaging. The coordinate and grid concept has been explored in other approaches wherein, using the sample geometry for image alignment (Zhu et al., 2021), and direct imprinting of a grid (Damstra et al., 2023) to the hydrogel, have provided methodologies to collect pre-/post-ExM data.

However, pre-/post-ExM methods of analysis are fundamentally limited by the diffraction limit. Hence, only distortions larger than this scale can be reliably detected. The difficulty of identifying these nanoscale distortions increase when combined with optical aberrations and noise in the data. This limits approaches using sample geometry and grid patterns, especially as these artefacts can increase deeper into the sample.

In context, the microplate approach takes advantage of the intrinsic ultrastructure of pre-ExM imaging to allow for localised distortion analysis relevant to the data. This is irrespective of the limitations of grid size or the dimensions of the sample.

In combination these tools could produce a method to offer greater precision to distortion analysis through both local measurements and standardised grid structures.

The question of image restoration using this data has posed an interesting challenge. These methods remain limited by the resolution of the original image or the fiducial markers. Therefore, such methods should be excluded to constitute best practice till novel, robust methodologies are developed.

6.4. General Limitations

The work outlined in this thesis has aimed to address two key weaknesses in the ExM technique: accessibility and reproducibility. Whilst the plate-based approach now opens a novel avenue to performing ExM, it is currently limited to four-fold approaches.

Methods to proceed towards a ten-fold approach have been discussed earlier but require testing and vigorous assessment of their viability.

The 3D-printed nature of the plates should lend itself to more accessible production, modification and usage. However, the requirements of a resin printer over standard FDM printing result in production limitations and the viability of other materials outside ABS remain unexplored.

Regarding the pre-/post-ExM data acquired and used for this work, the acquisition of the larger 3D datasets has proved a limiting factor for further analysis. This is due to the time required to obtain such data as well as the inherent difficulties in acquiring such information due to photobleaching and the increased spatial separation in fluorophores. In context, the 3D data acquired is generally from multiple gels in singular successful experiments. As the effects reported here are consistent between the gels in the experiment, further repeats could help ascertain whether the cause is limited to the few 3D ExM experiments performed.

6.5. Advancing Expansion Microscopy

Expansion microscopy has proven itself as an effective high-resolution method capable of application in a variety of situations. To move the technique forward, 3D expansion microscopy data acquisition and analysis approaches have been discussed in Chapter 5. In particular, the anisotropic nature of ExM and the effect in the axial direction. The methodology provided, aims to provide a framework to further investigate the discrepancies between the lateral and axial axis in both distortion and image alignment.

The increased spatial resolution ExM provides allows for avenues of exploration unique to ExM amongst the super-resolution techniques. Work to explore 3D ExM by (Norman et al., 2024), has shown that gel anisotropy can be associated with sample heterogeneity, in particular the structure dense regions within the nucleus. By adjusting the amount of Acryloyl-X, they have tentatively been able to produce four and twelvefold approaches with greater isotropy throughout the cell in all dimensions. This work primarily uses the expansion factor as a measure of the gel anisotropy, avoiding discussing RMSE analysis in the 3D setting.

This work aligns with previous data by (Ku et al., 2016), wherein the magnified analysis of the proteome (MAP) approach targeted crosslinking between endogenous proteins to improve gel homogenisation and binding. This work was performed on tissue samples using a four-fold expansion recipe and thoroughly demonstrated the use of denaturation processes to break crosslinks between the endogenous proteins and thereby allow the hydrogel to expand isotropically.

By understanding how RMSE is influenced in each axis, it is possible to isolate the likely cause of the distortion. This could allow for countermeasures through experimental changes. For example, if the expansion factor is greater in one axis and the RMSE shows this at a particular length scale, structures at that scale could be isolated to determine the issue. This could isolate low-scale drift issues or sample heterogeneity allowing a researcher to directly target and mitigate this for future experiments.

The anisotropic expansion seen in the 3D data is influenced by the axial resolution, sample density and inherent heterogeneity of the sample. Further exploration into these factors within other gel types could help isolate ExM methods best suited for 3D ExM and ways to mitigate anisotropy. Therein, allowing better use of the features of expansion microscopy.

Bibliography

Abbe, E, 1873. Beiträge zur Theorie Des Mikroskop. Arch Mikr Anat 9, 413–368.

Aguet, F., 2009. Super-Resolution Fluorescence Microscopy Based on Physical Models. École polytechnique fédérale de Lausanne.

Albrecht, N.E., Jiang, D., Akhanov, V., Hobson, R., Speer, C.M., Robichaux, M.A., Samuel, M.A., 2022. Rapid 3D-STORM imaging of diverse molecular targets in tissue. Cell Rep. Methods 2, 100253. https://doi.org/10.1016/j.crmeth.2022.100253

Alonso, V.L., 2022. Ultrastructure Expansion Microscopy (U-ExM) in Trypanosoma cruzi: localization of tubulin isoforms and isotypes. https://doi.org/10.1101/2022.03.06.483067

Amodeo, S., Kalichava, A., Fradera-Sola, A., Bertiaux-Lequoy, E., Guichard, P., Butter, F., Ochsenreiter, T., 2021. Characterization of the novel mitochondrial genome segregation factor TAP110 in Trypanosoma brucei. J. Cell Sci. 134. https://doi.org/10.1242/jcs.254300

Ankarklev, J., Jerlström-Hultqvist, J., Ringqvist, E., Troell, K., Svärd, S.G., 2010. Behind the smile: cell biology and disease mechanisms of Giardia species. Nat. Rev. Microbiol. 8, 413–422. https://doi.org/10.1038/nrmicro2317

Arganda-Carreras, I., Sorzano, C.O.S., Marabini, R., Carazo, J.M., Ortiz-de-Solorzano, C., Kybic, J., 2006. Consistent and Elastic Registration of Histological Sections Using Vector-Spline Regularization, in: Beichel, R.R., Sonka, M. (Eds.), Computer Vision Approaches to Medical Image Analysis, Lecture Notes in Computer Science. Springer Berlin Heidelberg, Berlin, Heidelberg, pp. 85–95. https://doi.org/10.1007/11889762_8

Asano, S.M., Gao, R., Wassie, A.T., Tillberg, P.W., Chen, F., Boyden, E.S., 2018. Expansion Microscopy: Protocols for Imaging Proteins and RNA in Cells and Tissues. Curr. Protoc. Cell Biol. 80. https://doi.org/10.1002/cpcb.56

Ashburner, J., Friston, K.J., 2005. Unified segmentation. NeuroImage 26, 839–851. https://doi.org/10.1016/j.neuroimage.2005.02.018

Balzarotti, F., Eilers, Y., Gwosch, K.C., Gynnå, A.H., Westphal, V., Stefani, F.D., Elf, J., Hell, S.W., 2017. Nanometer resolution imaging and tracking of fluorescent molecules with minimal photon fluxes. Science 355, 606–612. https://doi.org/10.1126/science.aak9913

Barjatya, A., 2004. Block Matching Algorithms For Motion Estimation. IEEE Trans. Evol. Comput. 8, 225–239.

Bates, M., Blosser, T.R., Zhuang, X., 2005. Short-Range Spectroscopic Ruler Based on a Single-Molecule Optical Switch. Phys. Rev. Lett. 94, 108101. https://doi.org/10.1103/PhysRevLett.94.108101

Bergstrand, J., Xu, L., Miao, X., Li, N., Öktem, O., Franzén, B., Auer, G., Lomnytska, M., Widengren, J., 2019. Super-resolution microscopy can identify specific protein distribution patterns in platelets incubated with cancer cells. Nanoscale 11, 10023–10033. https://doi.org/10.1039/C9NR01967G

Bertiaux, E., Balestra, A.C., Bournonville, L., Louvel, V., Maco, B., Soldati-Favre, D., Brochet, M., Guichard, P., Hamel, V., 2021. Expansion microscopy provides new insights into the cytoskeleton of malaria parasites including the conservation of a conoid. PLOS Biol. 19, e3001020. https://doi.org/10.1371/journal.pbio.3001020

Besl, P.J., McKay, N.D., 1992. A method for registration of 3-D shapes. IEEE Trans. Pattern Anal. Mach. Intell. 14, 239–256. https://doi.org/10.1109/34.121791

Betzig, E., Patterson, G.H., Sougrat, R., Lindwasser, O.W., Olenych, S., Bonifacino, J.S., Davidson, M.W., Lippincott-Schwartz, J., Hess, H.F., 2006. Imaging Intracellular Fluorescent Proteins at Nanometer Resolution. Science 313, 1642–1645. https://doi.org/10.1126/science.1127344

Bürgers, J., Pavlova, I., Rodriguez-Gatica, J.E., Henneberger, C., Oeller, M., Ruland, J.A., Siebrasse, J.P., Kubitscheck, U., Schwarz, M.K., 2019. Light-sheet fluorescence expansion microscopy: fast mapping of neural circuits at super resolution. Neurophotonics 6, 015005. https://doi.org/10.1117/1.NPh.6.1.015005

Büttner, M., Lagerholm, C.B., Waithe, D., Galiani, S., Schliebs, W., Erdmann, R., Eggeling, C., Reglinski, K., 2021. Challenges of Using Expansion Microscopy for Super-resolved Imaging of Cellular Organelles. ChemBioChem 22, 686–693. https://doi.org/10.1002/cbic.202000571

Büttner, M., Lagerholm, C.B., Waithe, D., Galiani, S., Schliebs, W., Erdmann, R., Eggeling, C., Reglinski, K., 2020. Challenges of using Expansion Microscopy for super-resolved imaging of cellular organelles. ChemBioChem n/a. https://doi.org/10.1002/cbic.202000571

Cahoon, C.K., Yu, Z., Wang, Y., Guo, F., Unruh, J.R., Slaughter, B.D., Hawley, R.S., 2017. Superresolution expansion microscopy reveals the three-dimensional organization of the Drosophila synaptonemal complex. Proc. Natl. Acad. Sci. U. S. A. 114, E6857–E6866. https://doi.org/10.1073/pnas.1705623114

Carravilla, P., Chojnacki, J., Rujas, E., Insausti, S., Largo, E., Waithe, D., Apellaniz, B., Sicard, T., Julien, J.-P., Eggeling, C., Nieva, J.L., 2019. Molecular recognition of the native HIV-1 MPER revealed by STED microscopy of single virions. Nat. Commun. 10, 78. https://doi.org/10.1038/s41467-018-07962-9

Chacko, L.A., Mikus, F., Ariotti, N., Dey, G., Ananthanarayanan, V., 2023. Microtubule–mitochondrial attachment facilitates cell division symmetry and mitochondrial partitioning in fission yeast. J. Cell Sci. 136, jcs260705. https://doi.org/10.1242/jcs.260705

Chakraborty, T., Driscoll, M.K., Jeffery, E., Murphy, M.M., Roudot, P., Chang, B.-J., Vora, S., Wong, W.M., Nielson, C.D., Zhang, H., Zhemkov, V., Hiremath, C., Cruz, E.D.D.L., Yi, Y., Bezprozvanny, I., Zhao, H., Tomer, R., Heintzmann, R., Meeks, J.P., Marciano, D.K., Morrison, S.J., Danuser, G., Dean, K.M., Fiolka, R., 2019. Light-sheet microscopy of cleared tissues with isotropic, subcellular resolution. Nat. Methods 16, 1109–1113. https://doi.org/10.1038/s41592-019-0615-4

Chang, J.-B., Chen, F., Yoon, Y.-G., Jung, E.E., Babcock, H., Kang, J.S., Asano, S., Suk, H.-J., Pak, N., Tillberg, P.W., Wassie, A.T., Cai, D., Boyden, E.S., 2017. Iterative expansion microscopy. Nat. Methods 14, 593–599. https://doi.org/10.1038/nmeth.4261

Chen, F., Tillberg, P.W., Boyden, E.S., 2015. Expansion microscopy. Science 347, 543–548. https://doi.org/10.1126/science.1260088

Chen, F., Wassie, A.T., Cote, A.J., Sinha, A., Alon, S., Asano, S., Daugharthy, E.R., Chang, J.-B., Marblestone, A., Church, G.M., Raj, A., Boyden, E.S., 2016. Nanoscale imaging of RNA with expansion microscopy. Nat. Methods 13, 679–684. https://doi.org/10.1038/nmeth.3899

Chen, M., Sun, T., Zhong, Y., Zhou, X., Zhang, J., 2021. A Highly Sensitive Fluorescent Akt Biosensor Reveals Lysosome-Selective Regulation of Lipid

Second Messengers and Kinase Activity. ACS Cent. Sci. https://doi.org/10.1021/acscentsci.1c00919
Chiu, C.-L., Clack, N., the napari community, 2022. napari: a Python Multi-Dimensional Image Viewer Platform for the Research Community. Microsc. Microanal. 28, 1576–1577. https://doi.org/10.1017/S1431927622006328
Chozinski, T.J., Halpern, A.R., Okawa, H., Kim, H.-J., Tremel, G.J., Wong, R.O.L., Vaughan, J.C., 2016. Expansion microscopy with conventional antibodies and fluorescent proteins. Nat. Methods 13, 485–488. https://doi.org/10.1038/nmeth.3833
Damstra, H.G., Mohar, B., Eddison, M., Akhmanova, A., Kapitein, L.C., Tillberg, P.W., 2022. Visualizing cellular and tissue ultrastructure using Ten-fold Robust Expansion Microscopy (TREx). eLife 11, e73775. https://doi.org/10.7554/eLife.73775
Damstra, H.G.J., Passmore, J.B., Serweta, A.K., Koutlas, I., Burute, M., Meye, F.J., Akhmanova, A., Kapitein, L.C., 2023. GelMap: intrinsic calibration and deformation mapping for expansion microscopy. Nat. Methods 20, 1573–1580. https://doi.org/10.1038/s41592-023-02001-y
Day, J.H., Della Santina, C.M., Maretich, P., Auld, A.L., Schnieder, K.K., Shin, T., Boyden, E.S., Boyer, L.A., 2024. HiExM: high-throughput expansion microscopy enables scalable super-resolution imaging. https://doi.org/10.7554/eLife.96025.3
Düring, D.N., Rocha, M.D., Dittrich, F., Gahr, M., Hahnloser, R.H.R., 2019. Expansion light sheet microscopy resolves subcellular structures in large portions of the songbird brain. Front. Neuroanat. 13. https://doi.org/10.3389/fnana.2019.00002
Dyba, M., Hell, S.W., 2002. Focal Spots of Size λ / 23 Open Up Far-Field Florescence Microscopy at 33 nm Axial Resolution. Phys. Rev. Lett. 88, 163901. https://doi.org/10.1103/PhysRevLett.88.163901
Dyba, M., Jakobs, S., Hell, S.W., 2003. Immunofluorescence stimulated emission depletion microscopy. Nat. Biotechnol. 21, 1303–1304. https://doi.org/10.1038/nbt897
Farnebäck, G., 2003. Two-Frame Motion Estimation Based on Polynomial Expansion, in: Bigun, J., Gustavsson, T. (Eds.), Image Analysis, Lecture Notes in Computer Science. Springer Berlin Heidelberg, Berlin, Heidelberg, pp. 363–370. https://doi.org/10.1007/3-540-45103-X_50
Fernandez, R., Moisy, C., 2021. Fijiyama: a registration tool for 3D multimodal time-lapse imaging. Bioinformatics 37, 1482–1484. https://doi.org/10.1093/bioinformatics/btaa846
Fischler, M.A., Bolles, R.C., 1981. Random sample consensus: a paradigm for model fitting with applications to image analysis and automated cartography. Commun. ACM 24, 381–395. https://doi.org/10.1145/358669.358692
Foundation, B., 2018. Blender [WWW Document]. blender.org. URL https://www.blender.org/ (accessed 12.15.24).
Freifeld, L., Odstrcil, I., Förster, D., Ramirez, A., Gagnon, J.A., Randlett, O., Costa, E.K., Asano, S., Celiker, O.T., Gao, R., Martin-Alarcon, D.A., Reginato, P., Dick, C., Chen, L., Schoppik, D., Engert, F., Baier, H., Boyden, E.S., 2017. Expansion microscopy of zebrafish for neuroscience and developmental biology studies. Proc. Natl. Acad. Sci. U. S. A. 114, E10799–E10808. https://doi.org/10.1073/pnas.1706281114

Gambarotto, D., Zwettler, F.U., Le Guennec, M., Schmidt-Cernohorska, M., Fortun, D., Borgers, S., Heine, J., Schloetel, J.-G., Reuss, M., Unser, M., Boyden, E.S., Sauer, M., Hamel, V., Guichard, P., 2019. Imaging cellular ultrastructures using expansion microscopy (U-ExM). Nat. Methods 16, 71–74. https://doi.org/10.1038/s41592-018-0238-1

Gao, M., Maraspini, R., Beutel, O., Zehtabian, A., Eickholt, B., Honigmann, A., Ewers, H., 2018. Expansion Stimulated Emission Depletion Microscopy (ExSTED). ACS Nano 12, 4178–4185. https://doi.org/10.1021/acsnano.8b00776

Gao, R., Yu, C.-C. (Jay), Gao, L., Piatkevich, K.D., Neve, R.L., Munro, J.B., Upadhyayula, S., Boyden, E.S., 2021. A highly homogeneous polymer composed of tetrahedron-like monomers for high-isotropy expansion microscopy. Nat. Nanotechnol. 1–10. https://doi.org/10.1038/s41565-021-00875-7

Gaudin, N., Gil, P.M., Boumendjel, M., Ershov, D., Pioche-Durieu, C., Bouix, M., Delobelle, Q., Maniscalco, L., Phan, T.B.N., Heyer, V., Reina-San-martin, B., Azimzadeh, J., 2022. Evolutionary conservation of centriole rotational asymmetry in the human centrosome. eLife 11. https://doi.org/10.7554/eLife.72382

Gerasimaitė, R., Bucevičius, J., Kiszka, K.A., Schnorrenberg, S., Kostiuk, G., Koenen, T., Lukinavičius, G., 2021. Blinking Fluorescent Probes for Tubulin Nanoscopy in Living and Fixed Cells. ACS Chem. Biol. 16, 2130–2136. https://doi.org/10.1021/acschembio.1c00538

Geumann, U., Schäfer, C., Riedel, D., Jahn, R., Rizzoli, S.O., 2010. Synaptic membrane proteins form stable microdomains in early endosomes. Microsc. Res. Tech. 73, 606–617. https://doi.org/10.1002/jemt.20800

Günay, K.A., Chang, T.-L., Skillin, N.P., Rao, V.V., Macdougall, L.J., Cutler, A.A., Silver, J.S., Brown, T.E., Zhang, C., Yu, C.-C., Olwin, B.B., Boyden, E.S., Anseth, K.S., 2023. Photo-expansion microscopy enables super-resolution imaging of cells embedded in 3D hydrogels. Nat. Mater. 22, 777–785. https://doi.org/10.1038/s41563-023-01558-5

Halpern, A.R., Alas, G.C.M., Chozinski, T.J., Paredez, A.R., Vaughan, J.C., 2017. Hybrid Structured Illumination Expansion Microscopy Reveals Microbial Cytoskeleton Organization. ACS Nano 11, 12677–12686. https://doi.org/10.1021/acsnano.7b07200

Harris, C.R., Millman, K.J., Van Der Walt, S.J., Gommers, R., Virtanen, P., Cournapeau, D., Wieser, E., Taylor, J., Berg, S., Smith, N.J., Kern, R., Picus, M., Hoyer, S., Van Kerkwijk, M.H., Brett, M., Haldane, A., Del Río, J.F., Wiebe, M., Peterson, P., Gérard-Marchant, P., Sheppard, K., Reddy, T., Weckesser, W., Abbasi, H., Gohlke, C., Oliphant, T.E., 2020. Array programming with NumPy. Nature 585, 357–362. https://doi.org/10.1038/s41586-020-2649-2

Hein, B., Willig, K.I., Hell, S.W., 2008. Stimulated emission depletion (STED) nanoscopy of a fluorescent protein-labeled organelle inside a living cell. Proc. Natl. Acad. Sci. 105, 14271–14276. https://doi.org/10.1073/pnas.0807705105

Hein, B., Willig, K.I., Wurm, C.A., Westphal, V., Jakobs, S., Hell, S.W., 2010. Stimulated Emission Depletion Nanoscopy of Living Cells Using SNAP-Tag Fusion Proteins. Biophys. J. 98, 158–163. https://doi.org/10.1016/j.bpj.2009.09.053

Heine, J., Reuss, M., Harke, B., D'Este, E., Sahl, S.J., Hell, S.W., 2017. Adaptive-illumination STED nanoscopy. Proc. Natl. Acad. Sci. 114, 9797–9802. https://doi.org/10.1073/pnas.1708304114

Hell, S.W., 2003. Toward fluorescence nanoscopy. Nat. Biotechnol. 21, 1347–1355. https://doi.org/10.1038/nbt895

Hell, S.W., Wichmann, J., 1994. Breaking the diffraction resolution limit by stimulated emission: stimulated-emission-depletion fluorescence microscopy. Opt. Lett. 19, 780. https://doi.org/10.1364/OL.19.000780

Herrmannsdörfer, F., Flottmann, B., Nanguneri, S., Venkataramani, V., Horstmann, H., Kuner, T., Heilemann, M., 2017. 3D d STORM Imaging of Fixed Brain Tissue, in: Poulopoulos, A. (Ed.), Synapse Development, Methods in Molecular Biology. Springer New York, New York, NY, pp. 169–184. https://doi.org/10.1007/978-1-4939-6688-2_13

Hinterndorfer, K., Laporte, M.H., Mikus, F., Tafur, L., Bourgoint, C., Prouteau, M., Dey, G., Loewith, R., Guichard, P., Hamel, V., 2022. Ultrastructure expansion microscopy reveals the cellular architecture of budding and fission yeast. J. Cell Sci. 135, jcs260240. https://doi.org/10.1242/jcs.260240

Hörl, D., Rojas Rusak, F., Preusser, F., Tillberg, P., Randel, N., Chhetri, R.K., Cardona, A., Keller, P.J., Harz, H., Leonhardt, H., Treier, M., Preibisch, S., 2019. BigStitcher: reconstructing high-resolution image datasets of cleared and expanded samples. Nat. Methods. https://doi.org/10.1038/s41592-019-0501-0

Huang, B., Wang, W., Bates, M., Zhuang, X., 2008. Three-Dimensional Super-Resolution Imaging by Stochastic Optical Reconstruction Microscopy. Science 319, 810–813. https://doi.org/10.1126/science.1153529

Jiang, N., Kim, H.-J., Chozinski, T.J., Azpurua, J.E., Eaton, B.A., Vaughan, J.C., Parrish, J.Z., 2018. Superresolution imaging of Drosophila tissues using expansion microscopy. Mol. Biol. Cell 29, 1413–1421. https://doi.org/10.1091/mbc.E17-10-0583

Jones, S.A., Shim, S.-H., He, J., Zhuang, X., 2011. Fast, three-dimensional super-resolution imaging of live cells. Nat. Methods 8, 499–505. https://doi.org/10.1038/nmeth.1605

Jungmann, R., Avendaño, M.S., Woehrstein, J.B., Dai, M., Shih, W.M., Yin, P., 2014. Multiplexed 3D cellular super-resolution imaging with DNA-PAINT and Exchange-PAINT. Nat. Methods 11, 313–318. https://doi.org/10.1038/nmeth.2835

Karagiannis, E.D., Kang, J.S., Shin, T.W., Emenari, A., Asano, S., Lin, L., Costa, E.K., Consortium, C.I.G.C., Marblestone, A.H., Kasthuri, N., Boyden, E.S., 2019. Expansion Microscopy of Lipid Membranes. bioRxiv 829903. https://doi.org/10.1101/829903

Ke, J., Liu, K., Sun, Y., Xue, Y., Huang, J., Lu, Y., Dai, J., Chen, Y., Han, X., Shen, Y., Shen, D., 2023. Artifact Detection and Restoration in Histology Images With Stain-Style and Structural Preservation. IEEE Trans. Med. Imaging 42, 3487–3500. https://doi.org/10.1109/TMI.2023.3288940

Klar, T.A., Jakobs, S., Dyba, M., Egner, A., Hell, S.W., 2000. Fluorescence microscopy with diffraction resolution barrier broken by stimulated emission. Proc. Natl. Acad. Sci. 97, 8206–8210. https://doi.org/10.1073/pnas.97.15.8206

Klein, S., Staring, M., Murphy, K., Viergever, M.A., Pluim, J., 2010. elastix: A Toolbox for Intensity-Based Medical Image Registration. IEEE Trans. Med. Imaging 29, 196–205. https://doi.org/10.1109/TMI.2009.2035616

Klimas, A., Gallagher, B.R., Wijesekara, P., Fekir, S., DiBernardo, E.F., Cheng, Z., Stolz, D.B., Cambi, F., Watkins, S.C., Brody, S.L., Horani, A., Barth, A.L., Moore, C.I., Ren, X., Zhao, Y., 2023. Magnify is a universal molecular anchoring

strategy for expansion microscopy. Nat. Biotechnol. 1–12. https://doi.org/10.1038/s41587-022-01546-1
Königshausen, E., Schmitz, C.T., Rump, L.C., Sellin, L., 2021. Imaging of podocytic proteins nephrin, actin, and podocin with expansion microscopy. J. Vis. Exp. 2021. https://doi.org/10.3791/62079
Ku, T., Swaney, J., Park, J.-Y., Albanese, A., Murray, E., Cho, J.H., Park, Y.-G., Mangena, V., Chen, J., Chung, K., 2016. Multiplexed and scalable super-resolution imaging of three-dimensional protein localization in size-adjustable tissues. Nat. Biotechnol. 34, 973–981. https://doi.org/10.1038/nbt.3641
Kuang, W., Xin, B., Huang, Z.-L., Shi, B., 2022. A labeling strategy with effective preservation of fluorophores for expansion single-molecule localization microscopy (Ex-SMLM). Analyst 147, 139–146. https://doi.org/10.1039/d1an01680f
Kunz, T.C., Götz, R., Sauer, M., Rudel, T., 2019. Detection of Chlamydia Developmental Forms and Secreted Effectors by Expansion Microscopy. Front. Cell. Infect. Microbiol. 9. https://doi.org/10.3389/fcimb.2019.00276
Laporte, M.H., Klena, N., Hamel, V., Guichard, P., 2022. Visualizing the native cellular organization by coupling cryofixation with expansion microscopy (Cryo-ExM). Nat. Methods 19, 216–222. https://doi.org/10.1038/s41592-021-01356-4
Lee, H., Yu, C.-C., Boyden, E.S., Zhuang, X., Kosuri, P., 2021. Tetra-gel enables superior accuracy in combined super-resolution imaging and expansion microscopy. Sci. Rep. 11, 16944. https://doi.org/10.1038/s41598-021-96258-y
Lee, M.Y., Mao, C., Glaser, A.K., Woodworth, M.A., Halpern, A.R., Ali, A., Liu, J.T.C., Vaughan, J.C., 2022. Fluorescent labeling of abundant reactive entities (FLARE) for cleared-tissue and super-resolution microscopy. Nat. Protoc. 1–28. https://doi.org/10.1038/s41596-021-00667-2
Li, R., Chen, X., Lin, Z., Wang, Y., Sun, Y., 2018. Expansion enhanced nanoscopy. Nanoscale 10, 17552–17556. https://doi.org/10.1039/c8nr04267e
Lim, Y., Shiver, A.L., Khariton, M., Lane, K.M., Ng, K.M., Bray, S.R., Qin, J., Huang, K.C., Wang, B., 2019. Mechanically resolved imaging of bacteria using expansion microscopy. PLOS Biol. 17, e3000268. https://doi.org/10.1371/journal.pbio.3000268
Louvel, V., Haase, R., Mercey, O., Laporte, M.H., Soldati-Favre, D., Hamel, V., Guichard, P., 2022. Nanoscopy of organelles and tissues with iterative ultrastructure expansion microscopy (iU-ExM). https://doi.org/10.1101/2022.11.14.516383
Lowe, D.G., 2004. Distinctive Image Features from Scale-Invariant Keypoints. Int. J. Comput. Vis. 60, 91–110. https://doi.org/10.1023/B:VISI.0000029664.99615.94
Lu, C.-H., Huang, C.-Y., Tian, X., Chen, P., Chen, B.-C., 2023. Large-scale expanded sample imaging with tiling lattice lightsheet microscopy. Int. J. Biochem. Cell Biol. 154. https://doi.org/10.1016/j.biocel.2022.106340
Maes, F., Collignon, A., Vandermeulen, D., Marchal, G., Suetens, P., 1997. Multimodality image registration by maximization of mutual information. IEEE Trans. Med. Imaging 16, 187–198. https://doi.org/10.1109/42.563664
Marongiu, R., Marongiu, R., Gratiet, A.L., Gratiet, A.L., Pesce, L., Pesce, L., Bianchini, P., Diaspro, A., Diaspro, A., 2020. ExCIDS: a combined approach coupling Expansion Microscopy (ExM) and Circular Intensity Differential Scattering (CIDS) for chromatin-DNA imaging. OSA Contin. 3, 1770–1780. https://doi.org/10.1364/OSAC.388868

Martínez, G.F., Gazal, N.G., Quassollo, G., Szalai, A.M., Cid-Pellitero, E.D., Durcan, T.M., Fon, E.A., Bisbal, M., Stefani, F.D., Unsain, N., 2020. Quantitative expansion microscopy for the characterization of the spectrin periodic skeleton of axons using fluorescence microscopy. Sci. Rep. 10, 2917. https://doi.org/10.1038/s41598-020-59856-w

Mascheroni, L., Scherer, K.M., Manton, J.D., Ward, E., Dibben, O., Kaminski, C.F., 2020. Combining sample expansion and light sheet microscopy for the volumetric imaging of virus-infected cells with super-resolution. Biomed. Opt. Express 11, 5032–5044. https://doi.org/10.1364/BOE.399404

M'Saad, O., Bewersdorf, J., 2020. Light microscopy of proteins in their ultrastructural context. Nat. Commun. 11, 3850. https://doi.org/10.1038/s41467-020-17523-8

Nagorni, M., Hell, S.W., 1998. 4Pi-Confocal Microscopy Provides Three-Dimensional Images of the Microtubule Network with 100- to 150-nm Resolution. J. Struct. Biol. 123, 236–247. https://doi.org/10.1006/jsbi.1998.4037

Norman, R.X., Chen, Y.-C., Recchia, E.E., Loi, J., Rosemarie, Q., Lesko, S.L., Patel, S., Sherer, N., Takaku, M., Burkard, M.E., Suzuki, A., 2024. One step 4x and 12x 3D-ExM: robust super-resolution microscopy in cell biology. https://doi.org/10.1101/2024.08.13.607782

Olivier, N., Keller, D., Gönczy, P., Manley, S., 2013. Resolution Doubling in 3D-STORM Imaging through Improved Buffers. PLoS ONE 8, e69004. https://doi.org/10.1371/journal.pone.0069004

Ourselin, S., Roche, A., Prima, S., Ayache, N., 2000. Block Matching: A General Framework to Improve Robustness of Rigid Registration of Medical Images, in: Delp, S.L., DiGoia, A.M., Jaramaz, B. (Eds.), Medical Image Computing and Computer-Assisted Intervention – MICCAI 2000, Lecture Notes in Computer Science. Springer Berlin Heidelberg, Berlin, Heidelberg, pp. 557–566. https://doi.org/10.1007/978-3-540-40899-4_57

Park, H.-E., Choi, D., Park, J.S., Sim, C., Park, S., Kang, S., Yim, H., Lee, M., Kim, J., Pac, J., Rhee, K., Lee, J., Lee, Y., Lee, Y., Kim, S.-Y., 2019. Scalable and Isotropic Expansion of Tissues with Simply Tunable Expansion Ratio. Adv. Sci. 6. https://doi.org/10.1002/advs.201901673

Pellett, P.A., Sun, X., Gould, T.J., Rothman, J.E., Xu, M.-Q., Corrêa, I.R., Bewersdorf, J., 2011. Two-color STED microscopy in living cells. Biomed. Opt. Express 2, 2364. https://doi.org/10.1364/BOE.2.002364

Pernal, S.P., Liyanaarachchi, A., Gatti, D.L., Formosa, B., Pulvender, R., Kuhn, E.R., Ramos, R., Naik, A.R., George, K., Arslanturk, S., Taatjes, D.J., Jena, B.P., 2020. Nanoscale imaging using differential expansion microscopy. Histochem. Cell Biol. https://doi.org/10.1007/s00418-020-01869-7

proExM for tissues: gelation demonstration, 2017.

Ramachandran, P., Varoquaux, G., 2011. Mayavi: 3D Visualization of Scientific Data. Comput. Sci. Eng. 13, 40–51. https://doi.org/10.1109/MCSE.2011.35

Reinhardt, S.C.M., Masullo, L.A., Baudrexel, I., Steen, P.R., Kowalewski, R., Eklund, A.S., Strauss, S., Unterauer, E.M., Schlichthaerle, T., Strauss, M.T., Klein, C., Jungmann, R., 2023. Ångström-resolution fluorescence microscopy. Nature 617, 711–716. https://doi.org/10.1038/s41586-023-05925-9

Reuss, M., Engelhardt, J., Hell, S.W., 2010. Birefringent device converts a standard scanning microscope into a STED microscope that also maps molecular orientation. Opt. Express 18, 1049. https://doi.org/10.1364/OE.18.001049

Rueckert, D., Sonoda, L.I., Hayes, C., Hill, D.L.G., Leach, M.O., Hawkes, D.J., 1999. Nonrigid registration using free-form deformations: application to breast MR

images. IEEE Trans. Med. Imaging 18, 712–721. https://doi.org/10.1109/42.796284
Rust, M., Bates, M., Zhuang, X., 2006. Sub-diffraction-limit imaging by stochastic optical reconstruction microscopy (STORM). Nat Methods 3, 793–796 (2006). Nat. Methods 793–796. https://doi.org/10.1038/nmeth929
Scardigli, M., Pesce, L., Brady, N., Mazzamuto, G., Gavryusev, V., Silvestri, L., Hof, P.R., Destrieux, C., Costantini, I., Pavone, F.S., 2021. Comparison of Different Tissue Clearing Methods for Three-Dimensional Reconstruction of Human Brain Cellular Anatomy Using Advanced Imaging Techniques. Front. Neuroanat. 15. https://doi.org/10.3389/fnana.2021.752234
Schmidt, R., Wurm, C.A., Jakobs, S., Engelhardt, J., Egner, A., Hell, S.W., 2008. Spherical nanosized focal spot unravels the interior of cells. Nat. Methods 5, 539–544. https://doi.org/10.1038/nmeth.1214
Schnitzbauer, J., Strauss, M.T., Schlichthaerle, T., Schueder, F., Jungmann, R., 2017. Super-resolution microscopy with DNA-PAINT. Nat. Protoc. 12, 1198–1228. https://doi.org/10.1038/nprot.2017.024
Seehra, R.S., Warrington, S.J., Allouis, B.H.K., Sheard, T.M.D., Spencer, M.E., Shakespeare, T., Cadby, A., Bose, D., Strutt, D., Jayasinghe, I., 2023. Geometry-preserving expansion microscopy microplates enable high-fidelity nanoscale distortion mapping. Cell Rep. Phys. Sci. 4, 101719. https://doi.org/10.1016/j.xcrp.2023.101719
Shaib, A.H., Chouaib, A.A., Chowdhury, R., Altendorf, J., Mihaylov, D., Zhang, C., Krah, D., Imani, V., Spencer, R.K.W., Georgiev, S.V., Mougios, N., Monga, M., Reshetniak, S., Mimoso, T., Chen, H., Fatehbasharzad, P., Crzan, D., Saal, K.-A., Alawieh, M.M., Alawar, N., Eilts, J., Kang, J., Soleimani, A., Müller, M., Pape, C., Alvarez, L., Trenkwalder, C., Mollenhauer, B., Outeiro, T.F., Köster, S., Preobraschenski, J., Becherer, U., Moser, T., Boyden, E.S., Aricescu, A.R., Sauer, M., Opazo, F., Rizzoli, S.O., 2024. One-step nanoscale expansion microscopy reveals individual protein shapes. Nat. Biotechnol. https://doi.org/10.1038/s41587-024-02431-9
Shaib, A.H., Chouaib, A.A., Imani, V., Chowdhury, R., Georgiev, S.V., Mougios, N., Monga, M., Reshetniak, S., Mihaylov, D., Chen, H., Fatehbasharzad, P., Crzan, D., Saal, K.-A., Trenkwalder, C., Mollenhauer, B., Outeiro, T.F., Preobraschenski, J., Becherer, U., Moser, T., Boyden, E.S., Aricescu, A.R., Sauer, M., Opazo, F., Rizzoli, S.O., 2022. Expansion microscopy at one nanometer resolution. https://doi.org/10.1101/2022.08.03.502284
Sheard, T.M.D., Hurley, M.E., Colyer, J., White, E., Norman, R., Pervolaraki, E., Narayanasamy, K.K., Hou, Y., Kirton, H.M., Yang, Z., Hunter, L., Shim, J.-U., Clowsley, A.H., Smith, A.J., Baddeley, D., Soeller, C., Colman, M.A., Jayasinghe, I., 2019. Three-dimensional and chemical mapping of intracellular signaling nanodomains in health and disease with enhanced expansion microscopy. ACS Nano 13, 2143–2157. https://doi.org/10.1021/acsnano.8b08742
Sheard, T.M.D., Jayasinghe, I., 2020. Enhanced expansion microscopy to measure nanoscale structural and biochemical remodeling in single cells, in: Methods in Cell Biology. Academic Press. https://doi.org/10.1016/bs.mcb.2020.04.019
Sheard, T.M.D., Spencer, M.E., Shakespeare, T., Seehra, R.S., Suen, K.M., Jayasinghe, I., 2023. Diverse labelling of cellular compartments with NHS esters in expansion microscopy. Biophys. J. 122, 275a. https://doi.org/10.1016/j.bpj.2022.11.1570

Shroff, H., Galbraith, C.G., Galbraith, J.A., Betzig, E., 2008. Live-cell photoactivated localization microscopy of nanoscale adhesion dynamics. Nat. Methods 5, 417–423. https://doi.org/10.1038/nmeth.1202

Sim, J., Park, C.E., Cho, I., Min, K., Eom, M., Han, S., Jeon, H., Cho, H.-J., Cho, E.-S., Kumar, A., Chong, Y., Kang, J.S., Piatkevich, K.D., Jung, E.E., Kang, D.-S., Kwon, S.-K., Kim, J., Yoon, K.-J., Lee, J.-S., Boyden, E.S., Yoon, Y.-G., Chang, J.-B., 2022. Nanoscale resolution imaging of the whole mouse embryos and larval zebrafish using expansion microscopy. https://doi.org/10.1101/2021.05.18.443629

Singh, H., Lu, R., Rodríguez, P.F.G., Wu, Y., Bopassa, J.C., Stefani, E., Toro, L., 2012. Visualization and quantification of cardiac mitochondrial protein clusters with STED microscopy. Mitochondrion 12, 230–236. https://doi.org/10.1016/j.mito.2011.09.004

Steib, E., Tetley, R., Laine, R.F., Norris, D.P., Mao, Y., Vermot, J., 2022a. TissUExM enables quantitative ultrastructural analysis in whole vertebrate embryos by expansion microscopy. Cell Rep. Methods 2, 100311. https://doi.org/10.1016/j.crmeth.2022.100311

Steib, E., Tetley, R., Laine, R.F., Norris, D.P., Mao, Y., Vermot, J., 2022b. TissUExM enables quantitative ultrastructural analysis in whole vertebrate embryos by expansion microscopy. Cell Rep. Methods 2. https://doi.org/10.1016/j.crmeth.2022.100311

Sun, D., Fan, X., Shi, Y., Zhang, H., Huang, Z., Cheng, B., Tang, Q., Li, W., Zhu, Y., Bai, J., Liu, W., Li, Y., Wang, X., Lei, X., Chen, X., 2020. Click-ExM enables expansion microscopy for all biomolecules. Nat. Methods 1–7. https://doi.org/10.1038/s41592-020-01005-2

Sun, Y., Zhang, Z., Bing, T., Liu, J., Li, W., Liu, X., Zhang, N., Shu, Y., Wang, J., Shangguan, D., 2022. Aptamer-Based Cell Nucleus Imaging via Expansion Microscopy. Anal. Chem. https://doi.org/10.1021/acs.analchem.2c00773

Thevenaz, P., Ruttimann, U.E., Unser, M., 1998. A pyramid approach to subpixel registration based on intensity. IEEE Trans. Image Process. 7, 27–41. https://doi.org/10.1109/83.650848

Tillberg, P., 2021. Protein-retention expansion microscopy (ExM): scalable and convenient super-resolution microscopy, in: Methods in Molecular Biology. pp. 147–156. https://doi.org/10.1007/978-1-0716-1402-0_7

Tillberg, P.W., Chen, F., Piatkevich, K.D., Zhao, Y., Yu, C.-C., English, B.P., Gao, L., Martorell, A., Suk, H.-J., Yoshida, F., DeGennaro, E.M., Roossien, D.H., Gong, G., Seneviratne, U., Tannenbaum, S.R., Desimone, R., Cai, D., Boyden, E.S., 2016. Protein-retention expansion microscopy of cells and tissues labeled using standard fluorescent proteins and antibodies. Nat. Biotechnol. 34, 987–992. https://doi.org/10.1038/nbt.3625

Török, P., Munro, P.R.T., 2004. The use of Gauss-Laguerre vector beams in STED microscopy. Opt. Express 12, 3605. https://doi.org/10.1364/OPEX.12.003605

Truckenbrodt, S., Maidorn, M., Crzan, D., Wildhagen, H., Kabatas, S., Rizzoli, S.O., 2018. X10 expansion microscopy enables 25-nm resolution on conventional microscopes. EMBO Rep. 19. https://doi.org/10.15252/embr.201845836

Truckenbrodt, S., Sommer, C., Rizzoli, S.O., Danzl, J.G., 2019. A practical guide to optimization in X10 expansion microscopy. Nat. Protoc. https://doi.org/10.1038/s41596-018-0117-3

Wang, Y., Yu, Z., Cahoon, C.K., Parmely, T., Thomas, N., Unruh, J.R., Slaughter, B.D., Hawley, R.S., 2018. Combined expansion microscopy with structured

illumination microscopy for analyzing protein complexes. Nat. Protoc. 13, 1869–1895. https://doi.org/10.1038/s41596-018-0023-8
Wells III, W.M., Viola, P., Atsumi, H., Nakajima, S., Kikinis, R., n.d. Multi-modal volume registration by maximization of mutual information.
Wen, G., Vanheusden, M., Acke, A., Valli, D., Neely, R.K., Leen, V., Hofkens, J., 2020. Evaluation of Direct Grafting Strategies via Trivalent Anchoring for Enabling Lipid Membrane and Cytoskeleton Staining in Expansion Microscopy. ACS Nano. https://doi.org/10.1021/acsnano.9b09259
Wen, G., Vanheusden, M., Leen, V., Rohand, T., Vandereyken, K., Voet, T., Hofkens, J., 2021a. A Universal Labeling Strategy for Nucleic Acids in Expansion Microscopy. J. Am. Chem. Soc. https://doi.org/10.1021/jacs.1c05931
Wen, G., Vanheusden, M., Leen, V., Rohand, T., Vandereyken, K., Voet, T., Hofkens, J., 2021b. A Universal Labeling Strategy for Nucleic Acids in Expansion Microscopy. J. Am. Chem. Soc. https://doi.org/10.1021/jacs.1c05931
Westphal, V., Rizzoli, S.O., Lauterbach, M.A., Kamin, D., Jahn, R., Hell, S.W., 2008. Video-Rate Far-Field Optical Nanoscopy Dissects Synaptic Vesicle Movement. Science 320, 246–249. https://doi.org/10.1126/science.1154228
Xu, J., Tehrani, K.F., Kner, P., 2015. Multicolor 3D Super-resolution Imaging by Quantum Dot Stochastic Optical Reconstruction Microscopy. ACS Nano 9, 2917–2925. https://doi.org/10.1021/nn506952g
Yao, L., Zhang, L., Fei, Y., Chen, L., Mi, L., Ma, J., 2021. Application of SNAP-Tag in Expansion Super-Resolution Microscopy Using DNA Oligostrands. Front. Chem. 9. https://doi.org/10.3389/fchem.2021.640519
Yu, C.-C. (Jay), Barry, N.C., Wassie, A.T., Sinha, A., Bhattacharya, A., Asano, S., Zhang, C., Chen, F., Hobert, O., Goodman, M.B., Haspel, G., Boyden, E.S., 2020. Expansion microscopy of C. elegans. eLife 9, e46249. https://doi.org/10.7554/eLife.46249
Zhao, Y., Bucur, O., Irshad, H., Chen, F., Weins, A., Stancu, A.L., Oh, E.-Y., DiStasio, M., Torous, V., Glass, B., Stillman, I.E., Schnitt, S.J., Beck, A.H., Boyden, E.S., 2017. Nanoscale imaging of clinical specimens using pathology-optimized expansion microscopy. Nat. Biotechnol. 35, 757–764. https://doi.org/10.1038/nbt.3892
Zhu, C., Wang, A., Chen, L., Guo, L., Ye, J., Chen, Q., Wang, Q., Yao, G., Xia, Q., Cai, T., Guo, J., Yang, Z., Sun, Z., Xu, Y., Lu, G., Zhang, Z., Cao, J., Liu, Y., Xu, H., 2021. Measurement of expansion factor and distortion for expansion microscopy using isolated renal glomeruli as landmarks. J. Biophotonics n/a. https://doi.org/10.1002/jbio.202100001
Zwettler, F.U., Reinhard, S., Gambarotto, D., Bell, T.D.M., Hamel, V., Guichard, P., Sauer, M., 2020. Molecular resolution imaging by post-labeling expansion single-molecule localization microscopy (Ex-SMLM). Nat. Commun. 11, 3388. https://doi.org/10.1038/s41467-020-17086-8